Title
Photodissociation Studies of Combustion Relevant Radical Molecules

Author
Shapero, Mark Jeffrey

Publication Date
2017

Peer reviewed|Thesis/dissertation

Photodissociation Studies of Combustion Relevant Radical Molecules

by

Mark Jeffrey Shapero

A dissertation submitted in partial satisfaction of the

requirements for the degree of

Doctor of Philosophy

in

Chemistry

in the

Graduate Division

of the

University of California, Berkeley

Committee in charge:

Professor Daniel M. Neumark, Chair
Professor Richard Saykally
Professor Michael Frenklach

Fall 2017

Photodissociation Studies of Combustion Relevant Radical Molecules

Mark Jeffrey Shapero

Abstract

Photodissociation Studies of Combustion Relevant Radical Molecules

by

Mark Jeffrey Shapero

Doctor of Philosophy in Chemistry

University of California, Berkeley

Professor Daniel M. Neumark, Chair

The photodissociation of several combustion relevant radical molecules has been carried out. These species behave significantly different from closed shell species and the experiments presented here provide fundamental new insights into the chemical dynamics of free radicals.

The experiments were carried out on a molecular beam photofragment translational spectroscopy instrument. Radicals were generated by flash pyrolysis of a suitable precursor and entrained in a pulsed molecular beam. The radicals were then photodissociated and the products were detected with a rotatable mass spectrometer based on electron impact ionization.

The benzyl radical photodissociation and the cyclopentadienyl radical photodissociation were investigated at 248 nm. Two dissociation channels were observed for each radical. The benzyl radical dissociates into H + C_7H_6 and CH_3 + C_6H_4 and the cyclopentadienyl radical dissociates to H + C_5H_4 and C_3H_3 + C_2H_2, where the C_5H_4 fragment was identified as ethynylallene by its ionization energy. The translational energy distribution determined for each channel suggests that every dissociation mechanism occurs via internal conversion to the ground state followed by intramolecular vibrational redistribution and dissociation. The branching ratio between the two competing channels for each radical was measured experimentally and compared to RRKM (Rice-Ramspberger-Kassel-Marcus) calculations. For both radicals, the dominant experimental channel was corroborated by RRKM calculations.

To my family and friends

Contents

List of Figures

List of Tables

Acknowledgments

I could not have completed my PhD without the support of an incredible number of people and I owe a great deal of gratitude to every single one of them! I will cherish my graduate school experience and it is a positive memory because of the involvement of everyone in my life.

Dan Neumark was an excellent advisor! I am thankful for his mentorship and support in both my research pursuits and extracurricular activities.

Neil Cole-Filipiak taught me everything I needed to know to perform my experiments. He is directly responsible for my successful research.

Isaac Ramphal made me redundant in lab almost as soon as he joined. For that, I am extremely grateful.

Holly Williams and Marissa Weichman joined the Neumark lab in the same year as I and we have progressed through graduate school together. I have greatly relied on them during my time here even up to our last days of filing dissertations together.

The members of the Neumark group, with all the different iterations, made coming to lab everyday enjoyable and sometimes unpredictable! I have so many great memories with these amazing people.

The most important things that have kept me sane during grad school are all the friends that I have made outside of my research lab.

My amazing chemistry friends have been there since day one in graduate school. We have spent so much time together over the past 5 and half years and I wouldn't trade any of it. Thanks to Alec White, Jacob Olshansky, Jean Van Buren, Jon Witte, Lisa Alexander, Michelle Leuenberger, Monatrice Lam, Noelle Catarineu, Royce Lam, Samia Hamed, Scott Ellis, and Walter Ralston.

Eric Bolin, Patrick Wilson and Jamie Lincoff are who I turn to for those times when I just want to let go and dance. I am so thankful for all of the nights out we have had together and those late night Uber and Lyft rides home from the city.

I must thank the entire Big Gay Frisbee league. I have made so many great friends on and off the frisbee field through this amazing organization.

Finally, I would like to thank my parents and my sisters. They have always supported me through my 20 some years of schooling. I was always encouraged to ask questions and be curious, which has translated into this dissertation.

Chapter 1

Introduction

1.1 Photochemistry and Photodissociation

There are many different types of chemical reactions that are initiated by light. A critical human physiological example is the cis-trans isomerization of retinal in the eye, which begins with the absorption of a photon.[1] This photoisomerization initiates a complex transduction pathway ultimately leading to vision. These types of reactions make up the field of photochemistry, which includes many subfields including photosynthesis, photocatalysis, and photodissociation. As evidenced by the title of this dissertation, the focus here will be on photodissociation.

Photodissociation is a process whereby fragmentation of a molecule occurs following absorption of light. This process can be formally expressed as

$$\mathrm{ABC} + N_{photons} h\nu \rightarrow (\mathrm{ABC})^* \rightarrow \mathrm{A}(\alpha) + \mathrm{BC}(\beta), \tag{1.1}$$

where ABC represents the initial molecule that absorbs $N_{photons}$ number of photons, each with energy $h\nu$ of frequency ν. $(\mathrm{ABC})^*$ represents the photoexcited ABC molecule before it breaks apart into fragments A and BC and the labels α and β specify the quantum state of each fragment. The fragments in Equation 1.1 are one dissociation channel of the many different possible product channels, which may include AB + C or A + B + C as examples.

The importance of photodissociation in the context of life on Earth is exemplified by the ozone cycle. Ozone absorbs harmful UV light and subsequently breaks apart. It is replenished through the cycle shown below:[2]

$$\begin{aligned} \mathrm{O_3} + h\nu &\rightarrow \mathrm{O_2} + \mathrm{O} \\ \mathrm{O} + \mathrm{O_3} &\rightarrow 2\mathrm{O_2} \\ \mathrm{O} + \mathrm{O_2} + \mathrm{M} &\rightarrow \mathrm{O_3} + \mathrm{M}. \end{aligned} \tag{1.2}$$

In addition to the fundamental interest in photodissociation reactions, photodissociation experiments also provide insight on general reaction dynamics. An example of a general reaction is

$$\mathrm{AB}(\alpha) + \mathrm{C}(\beta) \rightarrow (\mathrm{ABC})^* \rightarrow \mathrm{A}(\gamma) + \mathrm{BC}(\delta). \tag{1.3}$$

Molecule AB reacts with C to produce molecules A and BC through an intermediate $(\mathrm{ABC})^*$, where α, β, γ, and δ specify the quantum state of each species. It is clear that the reactions in Equations 1.1 and 1.3 share many of the same components and thus generating the excited intermediate through photoexcitation provides a technique for studying reaction dynamics.[3,4]

The production of the excited intermediate by photoexcitation provides a huge advantage over other techniques.[3,5] Thermal activation through heating reactants in a bulb or with the use of shock tubes creates broad distributions of internal energy states, which obscure any state specific information.[3] Crossed molecular beam experiments, which may mimic Equation 1.3, are another technique to form an excited intermediate. However this type of experiment produces intermediate states with all possible collision geometries.[6] In addition, the excitation in the intermediate is dependent on the relative translational energy of the colliding molecules, which places an experimental restriction on the excitation energy in the intermediate species. Furthermore, the initiation time for both of these techniques is not precise because it is governed by either the diffusion rate or the collision rate.[3] Photoexcitation with lasers (or in some cases flash lamps) solves these issues. Lasers provide a well defined photon energy for excitation that can be tuned to provide a wide range of energies (with the caveat that the molecule will absorb the specific photon energy). Additionally, the time of photon absorption yields an exact starting time for the reaction. Ultimately, photodissociation provides an avenue for understanding molecular reactivity on a state-to-state level by initiating dynamics with state specificity.[3–5,7]

There are many questions that have guided the research in this field over the past 50 years. The following are just samples of such questions:

- How does the absorption of a photon lead to bond cleavage?
- What is the nature of the excited state?
- What is the lifetime of the intermediate excited complex?
- What are the primary fragments formed and what are their quantum states?
- How is the available energy partitioned among the various degrees of freedom?
- What effect does changing the initial state of the molecule have on the dissociation process?

The answers to these questions lie in the potential energy surfaces (PES) of each molecule.[3–5] The work presented in this dissertation provides answers to some of these questions for the particular molecules studied.

1.2 Neutral Free Radicals

Radicals are an attractive set of molecules to study because they play an important role in many different types of chemical reactions, such as polymerization,[8] atmospheric reactions,[9] and combustion.[10] Although radicals are encountered across a broad range of disciplines within the field of chemistry, there are still unanswered questions regarding their reactivity. Compared to closed shell molecules, radicals are more reactive because of their unpaired electron and this increase in reactivity makes studying them very difficult.

The photochemistry of radical molecules, just like closed shell molecules, depends highly on the potential energy surface of the individual molecules.[3–5] The reactivity differences are manifest in the potential energy surfaces. Generally, a closed shell molecule can dissociate either via heterolytic cleavage into two closed shell molecules, or via homolytic cleavage into two radical molecules. Whereas a radical molecule will dissociate into one radical molecule and either a closed shell molecule or a diradical molecule. This difference plays a significant role in shaping their potential energy surfaces. The presence of an exit barrier in a dissociation reaction indicates that the reverse reaction has an activation barrier.[11] Bimolecular reactions that involve closed shell molecules often have barriers to overcome the inherent stability of the closed shell species, whereas this is not the case for reactions of radicals.

Another difference is present in the manifold of electronic excited states. The unpaired electron produces low lying electronic states as there are electronic transitions to and from a singly occupied molecular orbital (example in Ref 12). Also, there is often some enhanced coupling between these states. The effect of these low lying electronic states on the UV photodissociation dynamics is an open area of study.

1.2.1 Combustion Radicals

Combustion chemistry is a field where radical molecules play a large role. Understanding the reactivity of these radicals is essential for modeling combustion reactions. The goal of modeling combustion is to understand exactly what processes occur during realistic combustion, such is in a car engine or power plant, as well as to determine combustion conditions that are less hazardous to the environment and human health.[13,14] A simple combustion reaction is shown in Equation 1.4.

$$CH_4 + 2O_2 \rightarrow CO_2 + 2H_2O \tag{1.4}$$

Although the combustion of methane gas in the presence of oxygen seems rather straight forward and simple, it still contains at least 8 elementary reaction steps, many containing

radical species, that sum to Equation 1.4.[15] Realistic fuels such as gasoline and diesel make combustion even more complicated since gasoline and diesel are complex mixtures, which contain alkanes, alkenes, ketones, cyclic species etc. with a range of sizes from 4 up to 15 carbon atoms.[16] As these fuels are burned, many different reactions take place including thermal dissociation which can lead to both production and decomposition of radicals. Modeling combustion relies on accurate dissociation pathways for radicals produced during combustion. Additionally, if there are competing pathways, the relative number of reaction trajectories that proceed through each pathway is also important.

The experiments presented in this dissertation showcase a method for producing combustion relevant radicals in a collisionless environment that allows their individual dynamics to be studied. In certain cases, the photo-induced dynamics can be related to thermal dissociation, which will be discussed in Chapters 3 and 4.

1.3 UV Photodissociation

Following photoexcitation, a molecule can undergo numerous different processes. It can relax without dissociating through emission of a photon or through collisional deactivation with a bath gas.[17] Alternatively, it can dissipate energy via dissociation. The experiments presented in this dissertation use UV light for excitation in a collisionless environment so dissociation can occur on an electronic excited state or on the electronic ground state.[17] The following two sections describe the possible dissociation mechanisms in more detail.

1.3.1 Dissociation on an Electronic Excited State

Absorption of a UV photon promotes a molecule to an electronically excited state.[17] The subsequent dissociation is highly dependent on the topography of the potential energy surface of that exact excited state. Two examples are shown in Figure 1.1.

In Figure 1.1 (a), the excited state that is accessed by absorbing a photon is repulsive along a specific bond and leads to the breaking of that bond. This process is generally fast, on the order of a bond vibrational period, and leads to large amounts of energy partitioned into the relative translational energy of the fragments.[5] The photodissociation of H_2O via the first absorption band is an example of this type of mechanism.[18]

An alternative excited state dissociation mechanism is shown in 1.1 (b) where the initial state after photoexcitation is bound. As depicted in the figure, there is not enough energy in the photon to dissociate to A + BC*, where BC* represents an electronic excited state of the BC molecule. In this case, the molecule evolves on the bound excited state until it transitions to another state. If the potential energy surfaces cross, the transition can occur through a conical intersection, and in Figure 1.1 (b) a conical intersection connects the bound excited state to a repulsive state. The role of conical intersections in photo-induced chemical

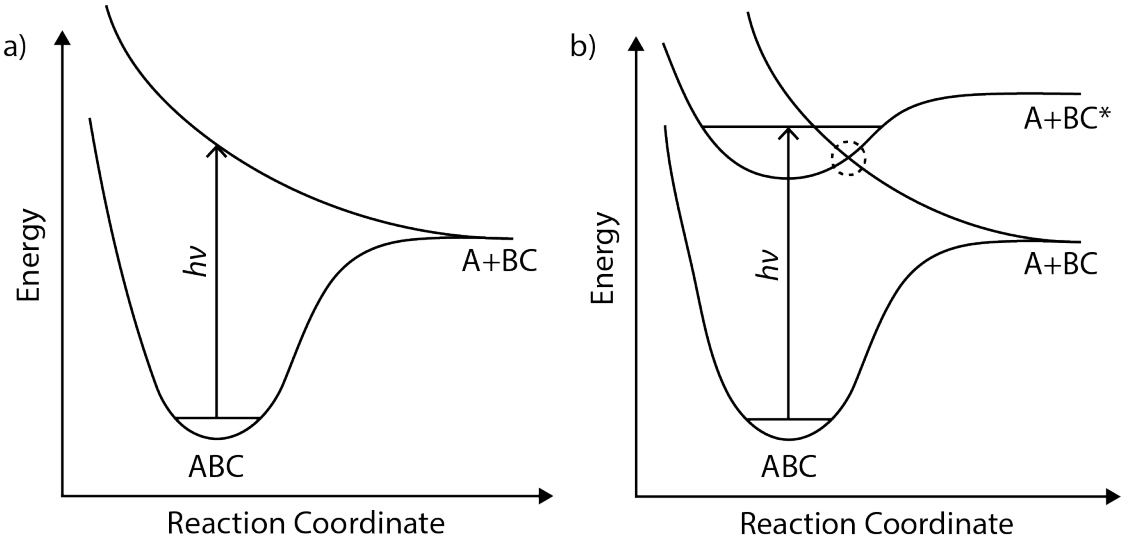

Figure 1.1: Example potential energy diagrams of photoexcitation to an electronic excited state for a hypothetical ABC molecule. (a) The excited state is repulsive along the A – BC coordinate. (b) The initial state accessed by the photon is bound. Dissociation proceeds after transitioning from the bound state to a repulsive state.

reactions is described in great detail by the work of Yarkony.[19] This type of mechanism is called "electronic predissociation"[20] and it is exhibited by the photodissociation of H_2S.[21–23]

There is another possibility for dissociating on an electronic excited state. If the photon energy in Figure 1.1 (b) was above the energy barrier to form A + BC*, then that channel would be a viable dissociation pathway.

1.3.2 Dissociation on the Electronic Ground State

Dissociating on the electronic ground state is the alternative process to dissociating on an electronic excited state. In general, ground state dissociation occurs when a) there are no viable excited state dissociation channels or b) when the excited state lifetime is too short to allow for nuclear motion on the excited state surface. In both cases, the excited state relaxes to the ground state in a process called internal conversion. This internal conversion can occur through one or more conical intersections, where the electronic potential energy surfaces cross. After internal conversion, the electronic excitation energy is converted into vibrational and internal rotational energy. The dissociation occurs once enough energy is localized in the reaction coordinate to overcome the energy barrier.[3] This type of mechanism is exemplified in Figure 1.2, which shows ground state dissociation channels with and without an exit barrier. Examples of this photodissociation mechanism are presented in Chapters 3 and 4.

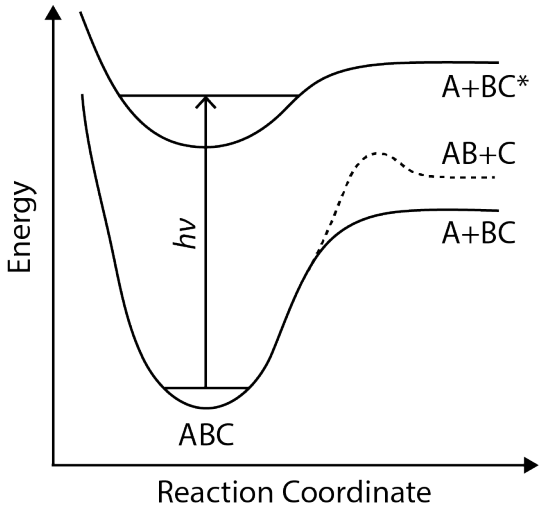

Figure 1.2: An example potential energy diagram with no viable excited electronic state dissociation channels and two ground electronic state dissociation channels. The formation of A + BC proceeds without an exit barrier, whereas the formation of AB + C has an exit barrier.

If intramolecular vibrational energy redistribution occurs on the ground state before dissociation, then this photodissociation mechanism can be related to thermal dissociation mechanisms.[3] This mechanism is called statistical dissociation because the rate of dissociation is determined by the statistical energy partitioning into all vibrational modes of the molecule. In this case, there are multiple theoretical frameworks for calculating reaction rates, such as RRKM theory,[24] which is discussed further in Chapters 3 and 4.

1.4 Photofragment Translational Spectroscopy

In a photodissociation experiment, there are many desirable pieces of information that can be ascertained and similarly many different techniques for acquiring that information, see Ref 4 for a full review. The technique used in the experiments presented here is photofragment translational spectroscopy (PTS), which was initially introduced by Wilson.[25] This technique measures the translational energy of the fragments produced by the photodissociation event. The translational energy can be related to the internal energy of the fragments by conservation of energy, which is expressed as

$$E_{avail} = h\nu + E_0 - D_0 = E_T + E_{int}. \tag{1.5}$$

The available energy to the fragments, E_{avail}, is equal to the photon energy, $h\nu$, plus the initial internal energy of the reactant, E_0, minus the dissociation energy for the specific channel, D_0. After dissociation, the available energy can be partitioned into either translational

energy, E_T, or internal energy of the fragments, E_{int}. Thus by measuring the translational energy distribution, the internal energy distribution can be determined and the type of dissociation mechanism can also be inferred. Additionally, if the internal energy can be experimentally determined, then the dissociation energy can be calculated experimentally.

There are various types of apparatuses for performing PTS and many different detection schemes available for determining the translational energy of the fragments.[7,26] Since it is difficult to detect neutral species, which many fragments are, most detection schemes rely on some form of ionization. The experiments presented here use electron ionization to ionize the fragments. The time-of-flight (TOF) spectra of the ionized fragments are then measured to determine their translational energy distribution. This technique is described in more detail below and in Chapter 2.

1.4.1 Kinematics

This section describes the kinematic constraints on the fragments produced from a photodissociation event. Herschbach introduced the Newton diagram to depict the kinematics and an example is shown in Figure 1.3.[27,28]

In the reactant center-of-mass frame, a molecule ABC absorbs a photon and dissociates. The resulting velocity of each fragment is governed by the conservation of energy in Equation 1.5 and the conservation of linear momentum

$$m_A \overrightarrow{u}_A + m_{BC} \overrightarrow{u}_{BC} = 0, \tag{1.6}$$

where m_i is the mass of fragment i and $\overrightarrow{u}_i$ is the center of mass velocity of fragment i. The resulting translational energy is

$$E_T(A + BC) = \frac{1}{2} m_A ||u_A^2|| + \frac{1}{2} m_{BC} ||u_{BC}^2||. \tag{1.7}$$

In a typical PTS experiment, the reactant is entrained in a molecular beam that is moving at some lab frame velocity $\overrightarrow{V}_{ABC}$. As the reactant dissociates, it scatters away from the molecular beam and this scattering is depicted in the Newton diagram in Figure 1.3. The circles represent the scenario when all of the available energy from Equation 1.5 goes into translational energy. In his case the fragments will scatter to a maximum angle away from the molecular beam, and measuring this angle provides insight on the dissociation mechanism, which is further discussed in Chapters 3 and 4.

1.4.2 Kinetics

From PTS, the translational energy distributions of the fragments are determined. The following discussion explains how the measured TOF spectra of the fragments are the result of

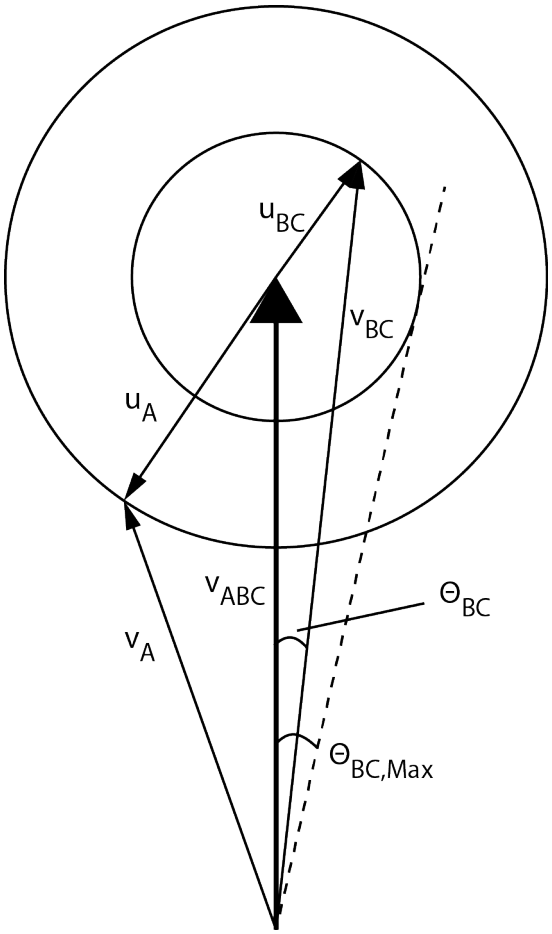

Figure 1.3: An example Newton diagram that represents the dissociation reaction, ABC → A + BC. The A fragment is lighter than the BC fragment.

the center-of-mass translational energy distribution, $P(E_T)$. For a more in depth explanation see the dissertation of X. Zhao.[29]

For a simplified reaction $R(r_i) + h\nu \rightarrow R(r_f) \rightarrow A(a) + B(b)$, the rate of production of photoproducts, A and B, from the reactant excited state, $R(r_f)$, can be described by the set of coupled differential equations in Equations 1.8 – 1.10. These equations include two sequential processes: the initial photoexcitation with rate constant k_{if}, and the unimolecular

dissociation with a state-to-state rate constant $k_d(r_f \rightarrow a, b)$.

$$\begin{aligned}\frac{dN_R(v_R, \omega_R, X, r_f, t)}{dt} =& \sum_i k_{if} N_R(v_R, \omega_R, X, r_i, t) \\ & - \sum_{a,b} k_d(r_f \rightarrow a, b) N_R(v_R, \omega_R, X, r_f, t)\end{aligned} \tag{1.8}$$

$$\frac{dN_A(v_A, \omega_A, X, a, t)}{dt} = \sum_{f,b} \int_{\{v_A, \omega_A\}} k_d(r_f \rightarrow a, b) N_R(v_R, \omega_R, X, r_f, t) \tag{1.9}$$

$$\frac{dN_B(v_B, \omega_B, X, b, t)}{dt} = \sum_{f,a} \int_{\{v_B, \omega_B\}} k_d(r_f \rightarrow a, b) N_R(v_R, \omega_R, X, r_f, t) \tag{1.10}$$

The density of species Y is given as $N_Y(v_Y, \omega_Y, X, y, t)$ with respect to laboratory velocity v_Y and solid angle ω_Y and three dimensional spatial coordinate X, in quantum state y at time t. $\{v_Y, \omega_Y\}$ represents the constrained integration over those variables. These equations rely on the following assumptions:

- There is no momentum change when the reactant absorbs a photon.
- Molecules do not change their positions during the effective reaction time, τ.

The resulting number density of A fragments from the dissociation process is directly related to the measured TOF spectrum because the detector used in the experiments described in this dissertation acts as a number density detector.[30,31] Determining the number density of A fragments requires the integration of Equations 1.8 – 1.10, which is complex and reported in full detail in X. Zhao's dissertation.[29] Briefly, a number of assumptions are made as well as a coordinate transformation to determine the product density. The assumptions are:

- The effective reaction time, τ, can be considered infinitely short with respect to the resolution of the arrival time, T.
- The size of the interaction region can be considered infinitely small compared to the resolution of the arrival time, T.
- The initial density of the reactant, R, in the molecular beam before irradiation, $N_R^0(v_R, \omega_R, X, r_i)$, is constant.
- The internal state distribution of the reactant, R, is independent of v_R and ω_R in the molecular beam.

The coordinate transformation changes the summation over product quantum states to the center-of-mass translational energy, E_T, and solid angle, Ω. The number density resulting from the integration and manipulation is

$$N_A(v_A,\omega_A)dv_A d\omega_A = \int\limits_{\{v_A,\omega_A,dv_A,d\omega_A\}} C^0 P(E_T,\Omega) N_R^0(v_R,\omega_R) dv_R d\omega_R dE_T d\Omega. \tag{1.11}$$

Here, $P(E_T,\Omega)$ is the normalized center-of-mass translational energy and angular distribution for the dissociation event and C^0 and $N_R^0(v_R,\omega_R)$ are constants relating to the molecular beam population.

In a PTS experiment, the product A enters the detector with solid angle ω_D with a laboratory velocity ranging from v_A to $v_A + dv_A$. The fragment is measured as a function of its arrival time, T, and therefore its velocity can be determined with knowledge of the flight length L, where $v_A = \frac{L}{T}$. The density at arrival time T is given by

$$N_A^T(T,\omega_D)dT = \left[\int\limits_{\omega_D} N_A(v_A,\omega_A)|\frac{\partial v_A}{\partial T}|d\omega_A\right]dT, \tag{1.12}$$

where

$$|\frac{\partial v_A}{\partial T}| = \frac{v_A}{T}.$$

The final necessary transformation is from center-of-mass variables E_T and Ω to variables v_A and ω_A in the laboratory frame. This transformation is performed using

$$E_T = \frac{1}{2}\frac{m_R m_A}{m_B}u_A^2 \Rightarrow \frac{\partial E_T}{\partial u_A} = \frac{m_R m_A}{m_B}u_A \tag{1.13}$$

and

$$\frac{\partial \Omega}{\partial \omega_A} = \frac{v_A^2}{u_A^2}. \tag{1.14}$$

These are the Jacobians for the coordinate transformation, where m_i is the mass of species i and u_i is the center-of-mass velocity of species i. The full expression for the time-of-flight spectrum of A is

$$N_A^T(T,\omega_D) = C^0\frac{v_A^3}{T}\frac{m_R m_A}{m_B}\int\limits_{\{T,\omega_D\}}\frac{P(E_T,\Omega)}{u_A}N_R^0(v_R,\omega_R)dv_R d\omega_R d\omega_A. \tag{1.15}$$

As discussed above, the fragments need to be ionized to be detected. For electron ionization, the ionization efficiency depends on the velocity of the fragment by

$$\eta_A(v_A) = \frac{\eta_A^o}{v_A}. \tag{1.16}$$

η_A^o can be approximated as a constant that depends on parameters of the ionizer and properties of species A. With this last consideration, the ion time-of-flight spectrum is

$$N_A^{T+}(T, \omega_D) = \frac{\eta_A^o}{v_A} N_A^T. \tag{1.17}$$

The product center-of-mass translational energy and angular distribution can be further simplified by assuming that the distributions can be decoupled into two independent distributions,

$$P(E_T, \Omega) = P(E_T) \times I(\Omega). \tag{1.18}$$

This $P(E_T)$ distribution is the quantity that is determined from the TOF spectra with PTS and the form of $I(\Omega)$ is known from previous work to be

$$I(\Omega) = \frac{1}{4\pi}\{1 + \beta P_2(cos[\Omega])\}, \tag{1.19}$$

$$P_2(x) = \frac{1}{2}(3x^2 - 1). \tag{1.20}$$

β is the anisotropy parameter that characterizes the type of electronic transition and timescale leading to dissociation; it can range from –1 to 2.[32,33]

1.5 Systems Discussed

The particular systems discussed here are the benzyl radical and the cyclopentadienyl radical. There are many similarities between these two molecules: both are hydrocarbon cyclic alkenyl radicals, both are resonantly stabilized radicals and both are prevalent in hydrocarbon combustion models.

The experiments carried out on these molecules, described in Chapters 3 and 4, are also very similar. The photodissociation of each molecule was carried out at 248 nm. In both cases, there was discussion in the literature suggesting that certain dissociation channels should exist that had never been previously detected and in both cases, these new dissociation channels were detected.

In addition to establishing the identities of the dissociation channel products, the branching ratios between competing channels were calculated. Through analyzing the results, the dissociation mechanisms for all channels were also determined.

Chapter 2

Experiment

2.1 Overview

Photofragment translational spectroscopy, outlined in the previous chapter, is conducted on a modified crossed molecular beam machine. Briefly, the target molecule is entrained in a molecular beam and hit with a laser pulse causing it to dissociate. The fragments are scattered off of the molecular beam axis and are detected as a function of this scattering angle with a rotatable mass spectrometer detector. The time-of-flight (TOF) spectrum of each fragment is measured and used to determine the translational energy distribution for the dissociation event. The following chapter gives more details on the apparatus and its implementation.

2.2 The Crossed Molecular Beam Machine

2.2.1 History of B Machine

Experiments in this dissertation were conducted on Yuan T. Lee's B Machine in its current home of D10 Latimer Hall in the College of Chemistry at the University of California Berkeley. This location was not always its home and it was not always an apparatus for photofragment translational spectroscopy. The initial design for the machine dates back to 1969 and Lee's postdoctoral work with Dudley Herschbach.[34] The B machine's design drawings were done by C. Ng in 1974. Upon Lee's move to UC Berkeley, the machine lived in Giauque Hall. When Lee left UC Berkeley, the B machine was gifted to Daniel Neumark and the new lab space in D10 Latimer was constructed specifically for the B machine. Then graduate student, Jason Robinson coordinated the move of the machine and the construction of the lab space. Details of that can be found in his lab notebooks as well as in his dissertation.[35]

B machine has been continually upgraded with new technology and repurposed for new experiments. Initially, the detector was pumped with ion pumps and the source and main chambers were pumped with diffusion pumps.[34] These pumps have all been upgraded to turbomolecular pumps. The initial experiments conducted on the apparatus were crossed molecular beam experiments; the current experiments are photodissociation experiments. The future possibilities for experiments on this apparatus include colliding a molecular beam with a liquid surface. Current graduate students are working on design modifications for that experiment.

2.2.2 Apparatus

The apparatus of the crossed molecular beam machine has three sections, the source chamber, the scattering or main chamber and the detector. As is evident from their names, the radical molecular beam is produced in the source chamber, photodissociated in the main chamber and detected with the detector. A schematic diagram of the apparatus is shown in Figure 2.1. All chambers are made of non-magnetic stainless steel.

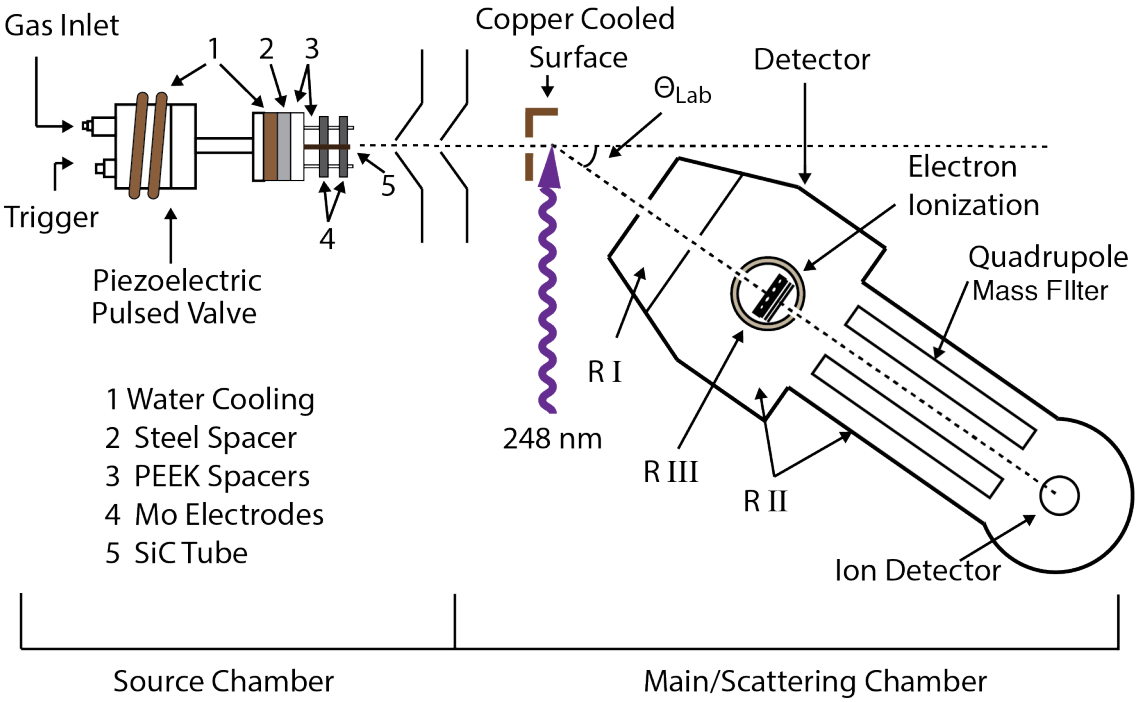

Figure 2.1: Schematic diagram of the crossed molecular beam apparatus

The source chamber is made up of a 10” tee cross that is mounted to the wall of the main chamber with a roughly triangular section cordoned off inside main chamber by

a metal insert. The metal insert has an opening for installing a skimmer that allows the molecular beam to pass through. The pulsed valve that produces the radical molecular beam is mounted inside the source chamber. The operation of the pulsed valve to produce a radical molecular beam is discussed below in section 2.5. Its alignment is discussed in section 2.2.3. There are feedthroughs into the source chamber for the gas to produce the molecular beam, for the electronics to trigger the pulsed valve and generate radicals, and for cooling water to thermally stabilize the pulsed valve. The source chamber is pumped with a 2200 L/s turbomolecular pump, which is backed by a Roots blower and Welch mechanical pump. Operational pressures are generally 6.0×10^{-5} torr for a 400 Hz rep rate molecular beam.

The main chamber is a very large vacuum chamber, which is necessitated by the rotation of the detector in vacuum. Its dimensions are $96 \times 96 \times 76$ cm. It is pumped with a 2200 L/s turbomolecular pump backed with a Welch mechanical pump. In addition, there is a copper surface that is cooled with a helium cryo-compressor to $\sim$10K. Typical operating pressures are 6.0×10^{-7} torr for a 400 Hz rep rate molecular beam. The side flanges of the main chamber have lenses to focus the incoming laser light into the interaction region.

Inside the main chamber is a retractable chopper wheel for characterizing the molecular beam velocity. The motor is a 3-phase synchronous Globe motor (part no. 75A1004-2). The motor is driven by a controller that was built by the now defunct Berkeley electronics shop and no circuit diagram is available. Fundamentally, the controller takes wall power and converts the frequency to 200 Hz and decreases the voltage. Attached to the motor is a chopper plate with four evenly spaced slits so when the motor runs at 200 Hz, the chopper slit passes the molecular beam axis at 800 Hz. The chopper wheel is monitored by a light–photodiode pair that outputs signal when a slit passes through it and that signal is used to trigger the pulsed valve.

The detector is mounted to a 63.5 cm diameter rotatable flange on top of the machine. Vacuum is maintained in the main chamber during rotation by two graphite-embedded Teflon tec rings with a direct-drive mechanical pump evacuating the space between the two rings. The geometry of the detector from a top down view is shown in Figure 2.1. Separating the detector from the main chamber is a slide valve with two different aperture sizes. The small hole is used to characterize the molecule beam on axis, whereas the larger hole is used for photodissociation experiments off axis. The molecular beam or photodissociation products go through three detector regions before reaching the electron ionizer; each region is pumped with its own turbomolecular pump and share a fourth turbomolecular pump with a single Welch mechanical backing pump. These regions are marked on Figure 2.1 as R I, R II, and R III and have typical operational pressures of $< 1 \times 10^{-10}$, $< 1 \times 10^{-12}$ and 5×10^{-11} torr, respectively. This triple differential pumping is necessary to have the lowest possible background in the ionizer, which is in region III. Further pumping is provided by cooling the walls of region III with liquid nitrogen.

Within region III is the electron ionizer and associated ion optics. The ionizer and ion optics are controlled by the Extrel Merlin 5221. This ionizer was installed in 2014 and N. Cole-Filipiak's dissertation goes into great detail on its design and operation.[36] After the molecules are ionized, cations pass back into region II, which contains the quadrupole mass filter and Daly style ion detector.[37] The quadrupole mass filter is a set of 4 cylindrical rods with applied oscillating voltages. The voltage on the quadrupole dictates which mass to charge (m/z) values have stable trajectories through the rods, thus acting as a mass filter.[38] The quadrupole voltages are also controlled by the Extrel Merlin 5221 and the oscillating frequency is either 1.2 MHz or 2.1 MHz. The 1.2 MHz frequency can pass up to $m/z = 300$, whereas the maximum m/z value for 2.1 MHz is 120.

Once the ionized fragment has passed through the quadrupole, it is accelerated towards the "doorknob", which is an aluminum electrode held at –30 kV. When the positively ionized fragment hits the doorknob, secondary electrons are emitted that are then accelerated away from the doorknob. These electrons then hit a scintillation material that emits photons, which are collected by a photomultiplier tube and turned into an electric signal through amplification with a dynode chain.

The raw signal output from the photomultiplier tube passes through a discriminator and then a level adapter, which converts the signal into TTL pulses, before being sent to the multichannel scalar for binning into time bins. The output of the multichannel scalar is a TOF spectrum, which shows the number of detection events as a function of time. The processing of the data is discussed below in section 2.3.

2.2.3 Alignment

Aligning the apparatus can be a multi-day job as it includes aligning the molecular beam and aligning the laser. The molecular beam is aligned so that it propagates through the interaction region and directly into the detector (when it is on axis). The laser is aligned so that it is focused at the interaction region where it intersects with the molecular beam.

Both alignment procedures begin with the same first step. Once the machine is vented to atmosphere and the flanges removed, horizontal and vertical threads are taped to either end of the machine along the axis to be aligned. There are notches on the machine that the threads are placed in, which define the alignment axis. For the molecular beam, the axis is aligned from the source chamber towards the detector, whereas for the laser, the axis is perpendicular to the molecular beam axis. The alignment scope is then positioned so that the crosshairs on the scope line up with both sets of intersecting threads at either end of the machine. This positioning ensures the scope is aligned to the alignment axis at all focal depths through the machine. It is very important to allow the scope to settle so that it does not move during the entire alignment process; settling can take up to 3 hours.

For the molecular beam, the pulsed valve is installed first into the source chamber. There are three set screws to adjust its positioning: up, down and away from the lab door. It is positioned so that the hole at the end of the pulse valve is aligned to the crosshairs on the scope. If the movement from the set screws is insufficient for alignment, the entire mount can be unbolted from the chamber and repositioned for better alignment. The next item to be installed is the first skimmer. It is held in place by two screws and its positioning cannot be adjusted. If it is not aligned to the scope crosshairs then either it is not sitting flush in its hole or the scope has shifted. The final piece to install is the second skimmer. This skimmer is mounted to a plate, which upon installation can be moved down and towards the door. Since the skimmer plate can only move in two direction, it is necessary to initially place the skimmer too high and too far away from the door so that it can be moved into alignment. Since the first skimmer's alignment cannot be adjusted, the second skimmer is aligned to the hole from the first skimmer.

For the laser, once the threads are in place and the scope has settled, the flange that the laser passes through is replaced on the chamber and a heater on the lens mount is turned on. The lens is heated so there is no hot spot in the glass when the laser goes through. Heat sensitive receipt paper is placed at the interaction region. The laser is turned on and for a split second allowed to hit the receipt paper, which turns black where the laser hit. The spot on the receipt paper is compared to the crosshairs from the scope and the mirrors are adjusted to move the spot in alignment with the scope crosshairs. This paper burning technique is repeated until the center of the laser spot is aligned with the scope crosshairs.

2.3 Data Analysis

2.3.1 Molecular Beam Characterization

The ultimate goal of analyzing the TOF spectra is to determine a center-of-mass translational energy distribution for the dissociation event. This analysis requires the conversion of the lab frame measured TOF spectra to the center-of-mass frame, which is done by subtracting the center-of-mass lab frame velocity aka the molecular beam velocity. This velocity is shown in Figure 1.3 as $\overrightarrow{V}_{ABC}$.

To determine the velocity of the molecular beam, a TOF spectrum is acquired on axis ($\Theta_{Lab} = 0°$) with the chopper wheel in the path of the molecular beam. The light–photodiode pair provides the trigger pulse for the pulsed valve. This TOF spectrum is fit to

$$N(v) \propto v^2 e^{-s^2(\frac{v-V_0}{V_0})^2}, \tag{2.1}$$

where V_0 is the velocity of the molecular beam and s is the speed ratio, which is the spread in velocity divided by the velocity.[39] The variable v is converted from the arrival time by

$$v = \frac{L'}{t_{real}} \tag{2.2}$$

where L' is the distance between the chopper wheel and the point of ionization and t_{real} is the neutral flight time of the species from the chopper wheel to the point of ionization.

2.3.2 Machine Parameters

To fit the TOF spectra to Equation 2.1, the measured arrival time, t_{meas}, must be converted to the neutral flight time, t_{real}, and the flight length, L', must be measured. The measured arrival time is augmented from the neutral flight time by several parameters outlined in Equation 2.3.

$$t_{meas} = t_{real} + \alpha_{ion}\sqrt{m} + E_o \pm M_o \tag{2.3}$$

The measured arrival time is the sum of the neutral flight time, plus $\alpha_{ion}\sqrt{m}$, the flight time of the ionized fragment of mass m, plus E_o, the electronic offset, and M_o ,the mechanical offset, which can be either positive or negative.

The measured arrival time can be divided up into the neutral species flight time and the ionized species flight time. The desired flight time is t_{real}, which is the neutral flight time to the ionizer, so the ion flight time must be subtracted. The ion flight time is given by α, the ion flight constant, times the square root of the mass of the fragment. The ion flight constant, α is determined by measuring the arrival times of different mass fragments that originate from the same parent species. In this case, all of their neutral flight times are the same, so the only difference is the ion flight time. The ion flight constant is the slope of the plot of arrival time versus square root mass.[40] The ion flight constant for B machine is ~ 4.7 μs amu$^{\frac{1}{2}}$.

The electronic offset in Equation 2.3 is a property of the light–photodiode pair. The photodiode has a 5 μs rise time after light is detected to transmit an electric signal.[41] The mechanical offset accounts for any misalignment of the chopper wheel and light–photodiode pair. It is determined by measuring the arrival time of a species with the chopper spinning in the clockwise direction and comparing it to the arrival time with the chopper spinning in the counterclockwise direction. The offset is equal to the difference divided by 2. The mechanical offset for B machine has been measured to be ~ 10 μs. The sign of the mechanical offset depends on the direction the chopper is spinning and it is set so that both directions result in the same neutral flight time.

With the above parameters, t_{real} can be calculated from t_{meas}. The flight length is still needed to determine the velocity. It is determined by producing molecular beams of rare gases, where the beam velocity can be calculated by

$$v_\infty = \sqrt{\frac{5k_bT}{m}}. \tag{2.4}$$

v_∞ is the velocity after supersonic expansion, k_b is Boltzmann's constant, T is the temperature of the nozzle, and m is the mass of the molecule.[39] Combining Equations 2.2, 2.3 and

2.4 gives

$$t_{meas} = \left(\frac{L'}{\sqrt{5k_bT}} + \alpha_{ion} \right) \sqrt{m} + (E_o \pm M_o), \tag{2.5}$$

where t_{meas} can be plotted as a function of $\sqrt{m}$ to determined L'. For B machine, that distance is measured to be 22.8 cm.

For photodissociation time-of-flight spectra, the starting point is the laser interaction region and not the chopper wheel. The neutral flight length needs to be adjusted, which is done by measuring the distance between the chopper wheel and the laser interaction region with a ruler. That distance is 1.7 cm, so the neutral flight length for a photodissociation experiment is 21.1 cm.

2.3.3 Determining Translational Energy Distributions

The TOF spectra are analyzed using PHOTRAN.[42] Simulated TOF spectra are produced by convoluting experimental parameters, such as beam velocity and flight length, with a given center-of-mass angular and translational energy distribution. An initial guess of the translational energy distribution, $P(E_T)$, is point-wise iteratively adjusted until good agreement is reached between the data and the simulation. All data are analyzed together to ensure everything is self-consistent.

2.4 Lasers

The molecular beam produced in the source chamber is crossed with a laser pulse in the main chamber. As discussed in the introduction, lasers provide a well defined amount of energy to initiate the dissociation event and the use of pulsed lasers with the pulsed molecular beam provides a well defined start time for the dissociation event. Excimer lasers are used for these experiments because they produce intense pulses of UV light. The absorption of a single photon of UV light can supply enough energy to overcome dissociation barriers in many molecules. Additionally, a high intensity photon flux is needed so that enough molecules in the molecular beam absorb and dissociate to overcome detector background.

There are two excimer lasers in the lab, a GAM EX100/500 and an LPX 220i. The GAM laser has a lower maximum power output and smaller spot sized compared to the LPX laser. The GAM laser was used for the experiment presented in Chapter 3. That experiment required low laser power to ensure only a single photon was being absorbed. The LPX laser was used for the experiment presented in Chapter 4 where a higher laser power was still able to maintain the single photon absorption regime.

2.4.0.1 Excimer Laser Use Guidelines

The lasing medium for an excimer laser is a gas mixture of a halogen gas, rare gas, and buffer gas. The GAM laser only has a single injection port and therefore a premixed gas cylinder must be used. The LPX has individual ports for each gas. It is recommended that halogen gas cylinders be replaced regularly to avoid the possibility of corrosion. A new gas fill for each laser is necessary when the output power drops below the usable threshold for the experiment. Generally a gas fill will last around 3 weeks but that is dependent on how much the laser is used. On the LPX, an injection of halogen gas has proven to extend the lifetime of a gas fill.

Compared to many other laser systems in the Neumark Group, the use of excimer lasers is fairly simple. Nevertheless, they still require alignment of the cavity. The lasing cavity is made up of a large gas cylinder with a mirror on one end and a window on the other end. Each laser has its own procedure for swapping out the optics, which can be found in their respective manuals. Once the optics are replaced, they need to be aligned parallel to each other and exactly perpendicular to the direction of laser propagation. This alignment procedure is done by directing a laser pointer down the cavity and looking at the subsequent reflections. It is important to verify that the laser pointer is directed straight down the cavity, which can be done by sweeping the direction of the laser pointer and confirming that the reflection moves in the logical direction.

The lasers are triggered through an external trigger, which is based on the timing of the pulse valve.

2.4.0.2 Excimer Maintenance

Over the past five and half years, a considerable amount of maintenance has been done on both lasers. This section will briefly describe the changes that were made to each laser. Additional information regarding symptoms and diagnostic testing is in the laser log section of the XBEAM lab notebooks.

The GAM laser was converted from a water cooled version to an air cooled version because the water cooling lines corroded and were constantly leaking. This change has no effect on running the laser. Additionally, the thyratron, rheostat and multiple capacitors have been replaced.

The LPX laser underwent a major refurbishment by OniCorp at the end of 2013. The largest operational change was the installation of new optic mounts that allow for easier replacement of the optics. In the years since the refurbishment, the varistors and the trigger card have been replaced.

2.5 Radical Source

The production of radicals is essential for the experiments presented here. This task has been accomplished with the use of a pyrolysis nozzle attached to the pulsed valve.[43,44] A schematic of the source design is shown on the left side of Figure 2.1 and a picture of the source is shown in Figure 2.2

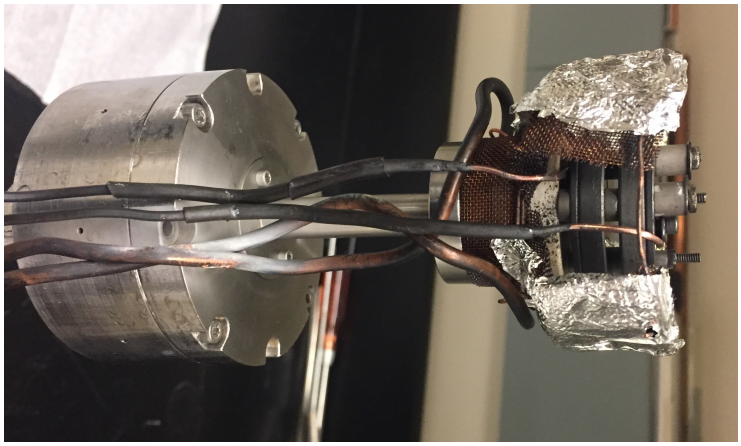

Figure 2.2: Picture of the pulsed valve with the pyrolysis source attached. The two molybdenum electrodes are visible towards the left. The aluminum foil forms the heat shield.

The first part of the source is the piezoelectric pulsed valve, which creates a short gas pulse that propagates through the pyrolysis nozzle. A piezoelectric crystal (Physik Instrumente part no. P-286.20) is housed in a home built metal casing and driven by a pulsed voltage. Attached to the crystal is an aluminum poppet that moves with the vibration of the crystal. At the end of the poppet is an o-ring that creates a seal over a hole in a metal surface. As the crystal and poppet vibrate, the seal is broken and gas escapes through the hole in the metal surface to form the gas pulse.[45]

The gas that is released from the pulsed valve enters the pyrolysis nozzle. The nozzle is attached to the base plate of the pulsed valve and contains many components,[46] which will be described in order starting from the pulsed valve. The first component is a water cooled copper block, which helps protect the pulsed valve from high temperatures. The next component is a steel spacer followed by a PEEK spacer. The molybdenum electrodes are separated from the PEEK spacer and from each other with smaller PEEK spacers. Molybdenum is used for the electrodes because it exhibits similar thermal expansion properties to SiC. The final component to the pyrolysis nozzle is the SiC tube (manufactured by GoodFellow), which has an inner diameter of 1 mm. It is installed between the two Mo electrodes and secured by set screws that tighten down on graphite half moon clamps to ensure electrical contact. Encompassing the entire assembly is a heat shield made of aluminum foil, which helps with temperature equilibration.

To operate the pyrolysis nozzle, the power supplied to the electrodes is gradually turned up in half amp increments until the final power is reached. During this period, the contents in the molecular beam are monitored via mass spectrometry. Once the final power is reached, the source is left for at least an hour to equilibrate. This waiting period is essential to ensure that the molecular beam is stable throughout the entire day.

This pyrolysis source was used to generate both the benzyl radical as well as the cyclopentadienyl radical for experiments presented in Chapters 3 and 4.

2.6 Laboratory Upgrades

Many laboratory upgrades were undertaken over the course of the 5 and a half years in which this research was completed. The upgrades include both changes to hardware as well as software to run the experiment. The hardware that was updated includes the multichannel scalar, the electron ionizer and the quadrupole controller. The latter two are described in detail in N. Cole-Filipiak's dissertation.[36] New laboratory software was written in LabView to communicate with and control equipment. These programs have greatly increased the productivity in the lab. The basic purpose of the software will be described here and the code with more detail can be found in Appendix A.

A new data acquisition program was written for two reasons, to migrate away from a WindowsNT computer and to upgrade the multichannel scalar from an Ortec Turbo-MCS to an Ortec MCS PCI card (A73-B32). The LabView program communicates with the MCS to initiate it and then to start, stop, clear and save any data collected on the MCS. The data acquisition program can also perform the beam velocity calculation by fitting the data to the beam profile in Equation 2.1.

Another LabView program was written to turn on the Leybold Coolpak 6200 helium cryo-compressor. This program monitors all of the machine pressures and only turns the compressor on if they are low enough. Before this program was written, the compressor was turned on every morning by hand, which then required a waiting time of 3 hours for the copper block in the main chamber to reach $\sim$10K. With this program, the compressor automatically turns on very early in the morning, so that the copper cooling block is cold by the time a researcher arrives. Additionally, the program can adjust the pressure in the source chamber and ensure it is constant by communicating with an Arduino Uno that controls a servo motor to turn the pressure knob. This pressure monitoring and adjustment has automated a process that would otherwise require the full attention of a researcher.

Chapter 3

Benzyl Radical Photodissociation Dynamics at 248 nm

The photodissociation of jet cooled benzyl radicals, C_7H_7, at 248 nm has been studied using photofragment translational spectroscopy. Two dissociation channels were observed, H + C_7H_6 and CH_3 + C_6H_4. The translational energy distribution determined for each channel suggests that both dissociation mechanisms occur via internal conversion to the ground state followed by intramolecular vibrational redistribution and dissociation. The branching ratio between these two channels has been measured to be CH_3 + C_6H_4 : H + C_7H_6 = 0.011 ± 0.004. The dominance of the H + C_7H_6 channel is corroborated by the branching ratio calculated using Rice-Ramsperger-Kassel-Marcus theory.

3.1 Introduction

The benzyl radical (C_7H_7) is ubiquitous in combustion schemes for aromatic hydrocarbons. It has been suggested as an intermediate in diesel and gasoline combustion[47] as well as a precursor to polycyclic aromatic hydrocarbons (PAHs) and soot,[13] which have negative environmental and health effects.[14] The benzyl radical is frequently encountered when modeling the combustion of toluene, for which it is the predominant decomposition product.[48–50] In addition to its bimolecular chemistry, the unimolecular decay of the benzyl radical is of interest in aromatic combustion,[51,52] and is not very well understood despite the importance and small size of this species. This work aims to probe this aspect of benzyl by focusing on

its photodissociation after excitation at 248 nm.

The benzyl radical was first hypothesized to exist after common spectral features were measured from related aromatic compounds in a glow discharge.[53] Since then, it has been investigated spectroscopically with numerous techniques. Its UV absorption spectrum has been measured[54] and the electronic transition at 248 nm, first reported in 1966,[55] was assigned to the $\tilde{D}^2B_2 \leftarrow \tilde{X}^2B_2$ transition.[56] A major topic in the literature is the coupling of the first two excited electronic states of benzyl, which has been studied by fluorescence spectroscopy,[57–60] photoionization spectroscopy,[12] cavity ring down spectroscopy[61] and theoretically.[62–65] Experimental[66,67] and theoretical[47,68–72] studies of the reactions between the benzyl radical and other molecules have also been carried out.

Thermal decomposition of the benzyl radical has been extensively studied. Initial fragmentation detected with mass spectrometry following toluene pyrolysis suggested that the benzyl radical breaks apart primarily to form C_5H_5 and C_2H_2 fragments with a second dissociation channel into C_4H_4 and C_3H_3 fragments.[73] Following this initial experiment, many shock tube studies measured the decay of the benzyl radical via UV absorption and the production of H atoms by atomic resonance absorption spectroscopy (HARAS).[74] A recent review of the shock tube studies recommends a total benzyl dissociation rate constant of (3.4 $\times$ 10^{15})exp(-42900/T) s^{-1} for the range of 1200 - 1750K.[74] The recommended dissociation mechanism includes the initial suggestion of two carbon-containing fragments along with the addition of two H loss channels.[75] Subsequent shock tube studies performed with HARAS determined that H loss is the dominant dissociation channel with 0.8 H atoms produced per benzyl radical dissociated.[76,77] Deuterated shock tube studies suggested three possible benzyl decay mechanisms: H loss from the ring, H loss from the side chain, and a non-atom loss channel, required to account for the rest of the signal decay.[77]

A new technique for investigating the thermal decomposition of radicals was recently presented by Lemieux[78] and Buckingham et al.[79] A benzyl radical precursor is passed through a heated micro-reactor resulting in radical formation followed by dissociation. The resulting fragments are then supersonically expanded into vacuum and detected with either photoionization mass spectrometry or matrix isolation IR spectroscopy. From these studies, many products were identified including fulvenallene (c-C_5H_4=C=CH_2), potentially the C_7H_6 fragment resulting from H loss; benzyne (c-C_6H_4), potentially from CH_3 loss; and the cyclopentadienyl radical, c-C_5H_5. However, this method cannot distinguish between primary benzyl decomposition products, secondary decomposition products, or non-unimolecular reaction products.

Limited work has been done on the photo-induced fragmentation of the benzyl radical. The fragmentation and collisional deactivation rates of vibrationally excited benzyl radicals have been measured after absorption at 308 nm.[80,81] Two-photon photodissociation of toluene and cycloheptatriene was studied using photofragment translation spectroscopy;[82]

only an H loss channel was detected. Direct photodissociation of the benzyl radical is limited to the work by Song et al.,[83] where H atom time of flight spectra were measured following excitation between 228 - 270 nm. The translational energy distribution for H loss was consistent with the production of fulvenallene as the C_7H_6 product. Deuteration studies also suggested scrambling of the ring and side chain H atoms. No comment was made on any other dissociation channel as only H atoms were measured.

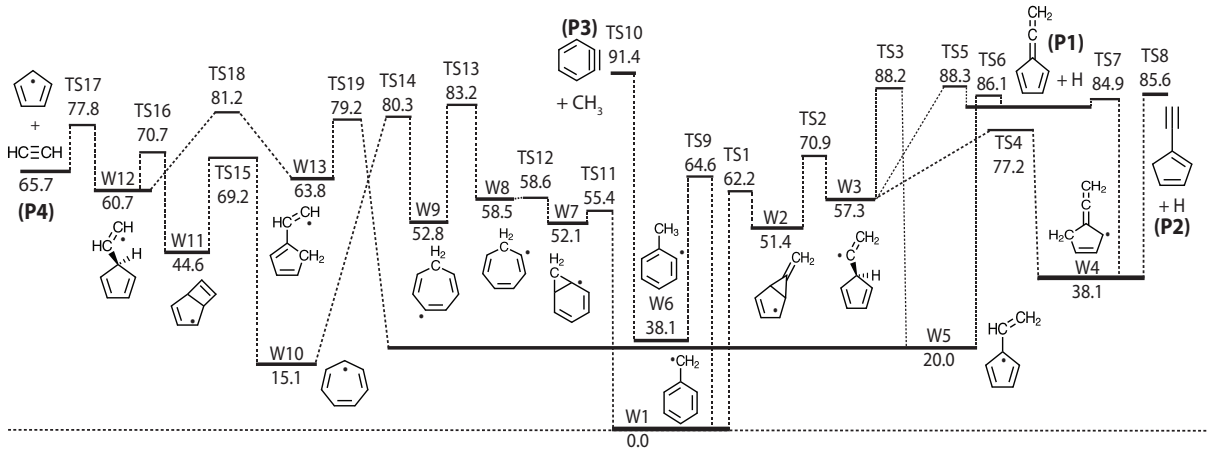

Figure 3.1: A simplified C_7H_7 potential energy diagram showing the production of acetylene + cyclopentadienyl, benzyne + CH_3, fulvenallene + H, and 2-ethynyl cyclopentadiene + H. The energetics and pathways are compiled from refs. 51, 52, 84, and 85. TS7 is shown as a well-defined transition state.[86] All energies are in kcal/mol.

Theoretical studies have proposed various benzyl dissociation mechanisms in an attempt to explain the experimental results presented above. Early theoretical mechanism predictions focused on fragmentation to two carbon-containing species,[75] but more recent studies agree that the most likely benzyl dissociation mechanism is H loss from benzyl to form fulvenallene (P1 in Figure 3.1).[51,52,84–86] The pathway to fulvenallene can be seen in Figure 3.1, which is a collection of potential energy diagrams from refs. 51, 52, 84, and 85. It is initiated by benzyl cyclization to a bicyclic intermediate, W2, followed by ring opening to form a vinyl radical species, W3. From W3, there are three possible hydrogen loss pathways: (i) direct H atom dissociation from the tertiary carbon via TS5; (ii) a hydrogen transfer from the tertiary carbon to the vicinal ring carbon, W4, followed by direct H atom dissociation via TS6; and (iii) hydrogen transfer from the tertiary carbon to the CCH_2 group, W5, also followed by direct H atom dissociation via TS7. The lowest energy path, which goes through W4, is reported by Cavallotti et al.[86] to have a well-defined transition state, whereas da Silva et al.[84] employed variational transition state theory to determine the transition state.

Another C_7H_6 isomer, 2-ethynyl cyclopentadiene (P2 in Figure 3.1), has been proposed as an alternative to the production of fulvenallene, and a recent calculation shows that it

can account for as much as 20% of the C_7H_6 product.[52] Its formation proceeds as a direct H loss from the terminal carbon in W4.

To account for the deuterated experimental results,[77,83] which suggest that H loss can occur from a ring or sidechain H atom, Derudi et al.[51] examined new possible decomposition mechanisms. A competitive CH_3 loss channel was found that allows for H atom scrambling between the ring and the sidechain of benzyl, which was not possible in the proposed fulvenallene pathways. This CH_3 loss pathway, as shown in Figure 3.1, begins with a hydrogen transfer from the benzyl ring to the side chain, W6, followed by a direct dissociation of the methyl group to form benzyne (P3 in Figure 3.1).

The competing formation of *c*-C_5H_5 and C_2H_2 was also considered through a series of isomerization steps from benzyl and from a subsequent recombination of H and fulvenallene.[85,86] The mechanism for acetylene and cyclopentadienyl production from benzyl can occur through two different pathways as shown in Figure 3.1. In the first mechanism, the benzyl radical can isomerize to the tropyl radical, c-C_7H_7 (W1→ W7→ W8→ W9→ W10), followed by the formation of a bicyclic intermediate, W11. This intermediate can undergo ring opening to W12 and a subsequent loss of C_2H_2 to form the products, P4. The other mechanism proceeds from W5 with two consecutive hydrogen transfer reactions to W13 then W12 followed by the formation of products, P4.[85]

Higher energy pathways to other products exist, although they are not expected to play an important role in thermal benzyl decomposition.[86] From a survey of the recent theoretical work[51,52,84–86] and experimental observations,[73,77,79,83] the benzyl radical dissociation channels of interest in this work are:

$$\text{benzyl} \rightarrow \text{fulvenallene} + \text{H} \qquad \Delta H_{0K} = 80.4 \text{ kcal/mol},^{86} \tag{3.1}$$

$$\rightarrow \text{2-ethynyl cyclopentadiene} + \text{H} \qquad \Delta H_{0K} = 85.6 \text{ kcal/mol},^{52} \tag{3.2}$$

$$\rightarrow \text{benzyne} + \text{methyl} \qquad \Delta H_{0K} = 91.4 \text{ kcal/mol},^{51} \tag{3.3}$$

$$\rightarrow \text{cyclopentadienyl} + \text{acetylene} \qquad \Delta H_{0K} = 65.7 \text{ kcal/mol}.^{85} \tag{3.4}$$

In order to gain additional insights into the unimolecular decay of the benzyl radical, we have carried out a study of its collisionless ultraviolet photodissociation dynamics at 248 nm using molecular beam photofragment translational spectroscopy.[4] This experiment can in principle detect channels (3.1) – (3.4) and thus determine if processes other than H atom loss occur. We do in fact observe a small amount of CH_3 loss producing the benzyne fragment, channel (3.3), in addition to H loss, which is most likely from channel (3.1). Translational energy distributions for both channels are consistent with internal conversion to the ground electronic state followed by statistical decay. The experimental branching ratio compares well to Rice-Ramsperger-Kassel-Marcus (RRKM) calculations.

3.2 Experimental

Benzyl radical photodissociation was studied on a modified crossed molecular beam apparatus with a fixed source and rotatable detector as described previously.[34,87,88] A pulsed benzyl radical beam was produced by flash pyrolysis of 2-phenylethyl nitrite as it passed through a resistively heated SiC tube attached to the nozzle of a piezoelectric pulsed valve.[43,89] The resulting net reaction is shown in Figure 3.2.

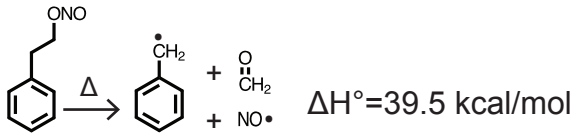

Figure 3.2: Schematic for the pyrolytic generation of benzyl radicals from the precursor 2-phenylethyl nitrite.[89]

The radical precursor, 2-phenylethyl nitrite, was synthesized from 2-phenylethanol[90] and verified to be $> 90\%$ pure via ^{1}H NMR (the other $< 10\%$ being unreacted 2-phenylethanol). A gas mixture of 1.2 atm of $\sim 10\%$ N_2 in He bubbled through an ice water cooled sample of 2-phenylethyl nitrite was used to back the pulsed valve; in previous work,[91] this gas mixture was found to give better vibrational cooling of pyrolytically generated radicals than pure He.

The molecular beam was collimated with two skimmers that separate the source chamber from the main scattering chamber. The collimated beam was crossed at 90° with a focused, unpolarized laser pulse with a fluence of 50 mJ/cm^2 at 248 nm from a GAM EX100/500 excimer laser. The pulsed valve and laser were operated at 200 Hz and 100 Hz respectively, which allowed for background subtraction from the radical beam. The scattered photofragments were detected as a function of laboratory angle, Θ_{Lab} in the plane defined by the laser and the molecular beam. After passing into a triply differentially pumped detector, the photofragments were ionized via electron impact ionization with 70 eV electrons. The resulting ions were mass-selected with a quadrupole mass filter and detected with a Daly style ion detector.[37] The ion signal as a function of time relative to the laser pulse was acquired with a multichannel scalar interfaced with a computer for $10^5 - 10^6$ laser shots. These time of flight (TOF) spectra were simulated using a forward convolution method to iteratively determine the center-of-mass translational energy distributions for each product channel.

Mass spectra of the molecular beam were used to verify 2-phenylethyl nitrite depletion ($m/z = 151$) and benzyl radical formation ($m/z = 91$); examples are shown in Figure 3.3. The gray trace is the precursor mass spectrum taken with pyrolysis off; the parent peak is visible at $m/z = 151$. With pyrolysis on, the parent peak disappears and the resulting mass spectrum (black line, Figure 3.3) matches the literature benzyl radical mass spectrum.[92] Due

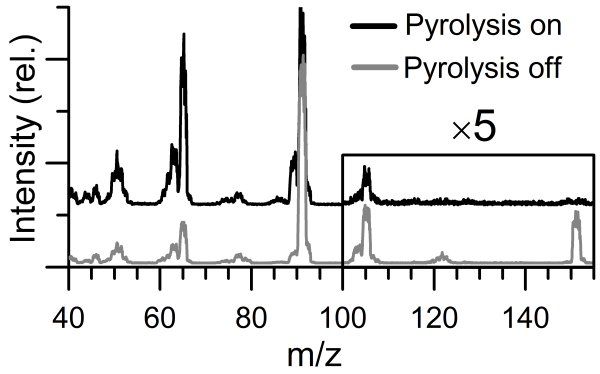

Figure 3.3: Mass spectrum of the molecular beam normalized to the $m/z = 91$ signal intensity with pyrolysis off (gray) and pyrolysis on (black). Upon heating the SiC tube, the peak at $m/z = 151$ disappears, and peaks at $m/z = 89$, 65 and 39 increase in relative intensity.

to dissociative ionization, there is a daughter peak at $m/z = 91$ from the precursor molecule in the gray trace of Figure 3.3. However, once the $m/z = 151$ peak is depleted, as in the black trace of Figure 3.3, it is expected that the $m/z = 91$ peak comes solely from the benzyl radical.

Further confirmation of precursor depletion and benzyl formation was made possible by the installation of a new Extrel axial beam ionizer with the capability of low electron energy ionization. Ionization efficiency curves for $m/z = 91$ are shown in Figure 3.4 with pyrolysis off and on while keeping the emission current constant at 0.5 mA and normalized for signal intensity. The electron energy scale was calibrated by ionization of the noble gases He, Ne, Ar, and Kr. The appearance energy is the extrapolated intercept from the linear region of the curve. The appearance energy of $m/z = 91$ with pyrolysis off was determined to be 10.2 eV, which indicates it is due to dissociative ionization, while with pyrolysis on the appearance energy of 7.0 eV matches the expected ionization energy of 7.2 eV of the benzyl radical.[93]

The benzyl radical beam velocity was characterized with a spinning slotted chopper wheel. Typical beam velocities were around 1800 m/s with speed ratios, defined as the beam flow velocity divided by the velocity spread, in the range of 4-5.

3.2.1 Electronic structure and RRKM calculations

RRKM calculations have been performed as a comparison to the experimental analysis. The stationary points of interest are depicted on the potential energy diagram in Figure 3.1 and are collected from refs. 51, 52, 84, and 85. TS8 and TS10 were determined using variational transition state theory with a 0.2 Å step size. Geometries, vibrational frequencies and the zero point energy at each step were calculated at the B3LYP/6-31+G(d,p) level using

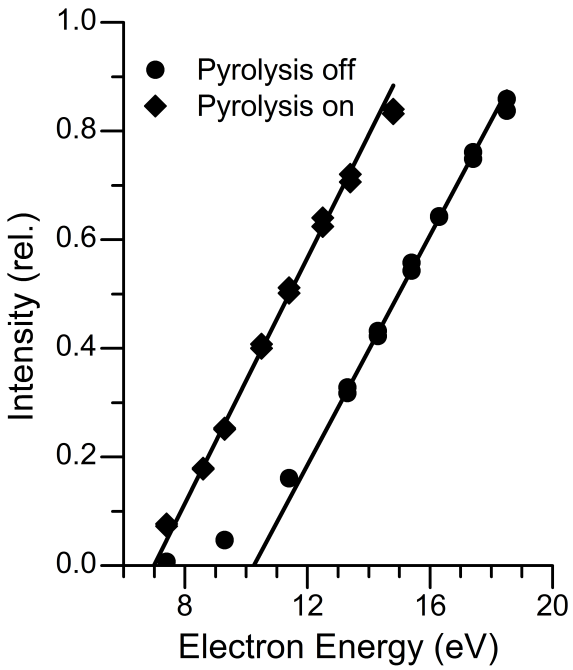

Figure 3.4: Ionization efficiency curves of $m/z = 91$ with pyrolysis off and on. The appearance potential for this signal with pyrolysis off is 10.2 eV whereas with pyrolysis on, it is 7.0 eV.

Gaussian 09[94] and the energies were reevaluated using MOLPRO[95] at the CCSD(T)/CBS level from the cc-pVDZ and cc-pVTZ basis sets using the scaling suggested by Martin.[96] The energies of the stationary points that were not previously reported at this level of theory were reevaluated using the above method from their reported geometries. The transitional modes were all treated in the harmonic oscillator approximation. The lowest vibrational frequency for W3, W6, W12 TS9, TS10, and TS17 was below 100 cm-1 and was thus treated as a free internal rotor with each internal rotational constant calculated from the reported or calculated (TS 10) geometry. The densities and sums of states for each local minimum and transition state were calculated using the Beyer-Swinehart algorithm[97] with the reported energies and vibrational frequencies treated as harmonic oscillator frequencies. Individual rate constants were calculated using the micro-canonical RRKM equation. The maximum energy was given by the photon energy. No tunneling effects were considered. All reaction pathways shown in Figure 3.1 were considered, using the steady state approximation on intermediate local minima to solve for the rate of H atom loss compared to benzyne + CH_3.

3.3 Results

TOF spectra at $m/z = 90$, $C_7H_6^+$, were measured at laboratory scattering angles $\Theta_{Lab} =$ 4°, 5° and 6° with respect to the molecular beam axis and are shown as open circles in Figure 3.5. TOF spectra at $m/z = 76$, $C_6H_4^+$, were detected at laboratory angles ranging from Θ_{Lab} = 4° up to 18°. Representative spectra are shown in Figure 3.6 (open circles). Additional TOF spectra were taken at the dissociative ionization masses of the above parent fragments at $m/z = 74$ and $m/z = 50$, shown in Figure 3.7; these spectra are used to determine product branching ratios as discussed in Section 3.4. Signal at $m/z = 26$ and $m/z = 65$, the masses of the acetylene and cyclopentadienyl photoproduct parent ions, were extensively searched for but not observed.

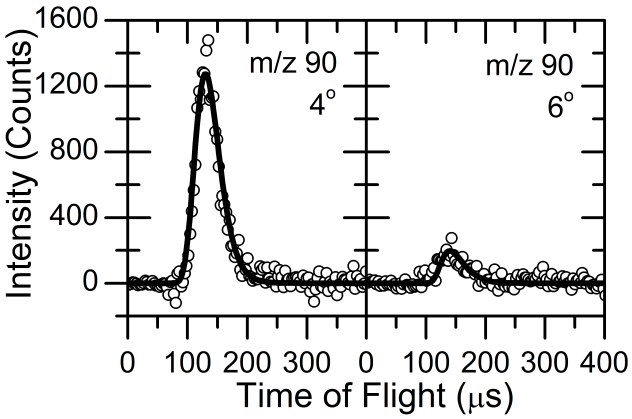

Figure 3.5: Representative TOF spectra of $m/z = 90$ at 4° and 6°. The open circles are data points and the solid line is a simulation based on the $P(E_T)$ distribution in Figure 8.

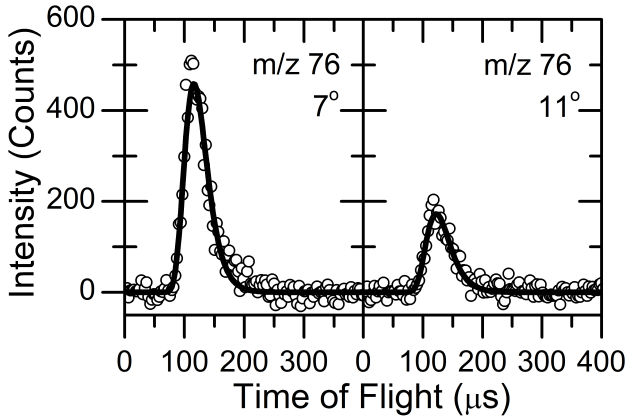

Figure 3.6: Representative TOF spectra of $m/z = 76$ at 7° and 11°. The open circles are data points and the solid line is a simulation based on the $P(E_T)$ distribution in Figure 9.

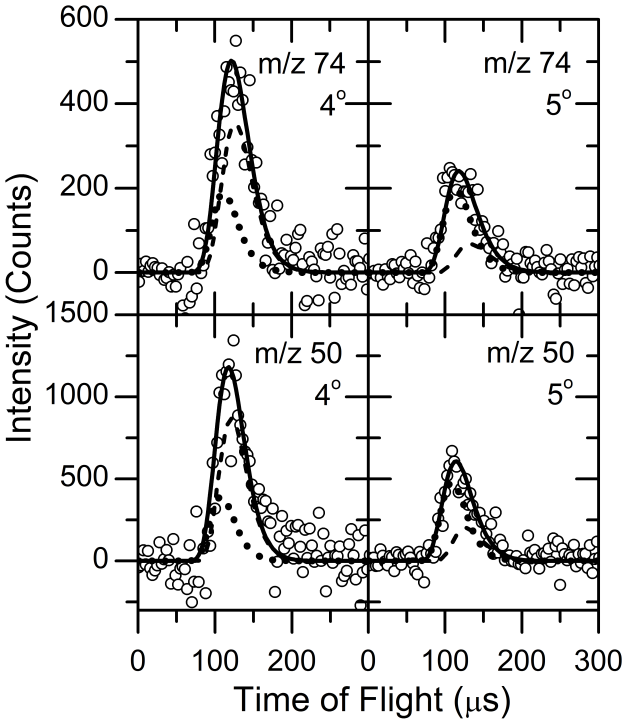

Figure 3.7: TOF spectra of $m/z = 74$ and 50 collected at 4° and 5°. The data are shown as open circles. The simulation has two components: the dashed line comes from the H loss $P(E_T)$ of Figure 8 and the dotted line comes from the CH_3 loss $P(E_T)$ of Figure 9. The solid line is the summed simulation.

Other sources of signal besides the benzyl radical photodissociation were assessed. We looked at the photodissociation of the precursor, 2-phenylethyl nitrite, with the pyrolysis source off, and found one primary pathway which mimicked the pyrolysis reaction in Figure 3.2 forming benzyl ($m/z = 91$), NO ($m/z = 30$) and formaldehyde ($m/z = 30$). With pyrolysis on, there was no longer any measured photodissociation signal at $m/z = 91$ or $m/z = 30$ off the beam axis, suggesting that precursor photodissociation is no longer present. The precursor reagent, 2-phenylethanol, also photodissociates to $m/z = 91$, so the lack of signal at $m/z = 91$ also eliminates it as a TOF contaminant. Bibenzyl may be formed in the SiC micro-reactor and may also photodissociate to form the stable benzyl radical, however it too is eliminated by absence of $m/z = 91$ signal away from the molecular beam. A contaminant at $m/z = 105$ ($C_8H_9^+$) is present in the molecular beam with the pyrolysis source on and the precursor parent m/z peak absent, as seen from the black trace in Figure 3.3. This feature may stem from C_8H_9 radicals formed in the SiC tube from the loss of ONO from the precursor molecule. Considering this formation scenario, the structure of this radical is likely either $C_6H_5CH_2C\bullet H_2$, 2-phenyleth-1-yl, or the more stable isomer, $C_6H_5C\bullet HCH_3$, 1-phenyleth-1-yl.[98] If such a radical was produced and photodissociated, we would expect

to see an H atom loss channel forming the stable styrene molecule ($m/z = 104$),[98] but no photodissociation signal at any $m/z > 90$ is observed. It thus appears all signals in Figs. 3.5–3.7 originate from benzyl radical photodissociation.

Possible contributions from two photon processes were assessed by conducting a laser power dependence study. TOF spectra taken at $m/z = 90$ and 85 mJ/cm^2 had a fast edge that did not depend linearly on laser power. At 50 mJ/cm^2 and below, the fast edge was reduced and the signal intensity had a linear dependence on laser power, in agreement with the laser power study done by Song et al.[83]

3.4 Analysis

Conservation of energy in this experiment is expressed by:

$$E_{avail} = h\nu + E_0 - D_0 = E_{int} + E_T \tag{3.5}$$

The available energy (E_{avail}) to the photoproducts is the photon energy ($h\nu$) and any initial internal energy (E_0) minus the dissociation energy (D_0) for the specific channel. This available energy can either go into the internal energy of the products (E_{int}) or into their relative translational energy (E_T). The initial internal energy of the benzyl radical following supersonic jet expansion is unknown but is approximated as zero for purposes of analysis, supported by our previous work on phenyl radical expansions seeded in He with ~10% N_2.[91]

When all of the available energy is partitioned into translational energy, the maximum laboratory scattering angle can be calculated with knowledge of the benzyl beam velocity. Based on the most energetically favorable pathway for H loss in which fulvenallene is formed, channel (3.1), the $m/z = 90$ fragment should only be present up to a laboratory scattering angle of $\Theta_{Lab} = 6°$. This restriction is depicted in the Newton diagram of Figure 3.8 and reflects the large mass ratio in the recoiling fragments, 90:1. The dashed circle represents the fastest possible center-of-mass velocities for the fulvenallene fragment. As no signal at $m/z = 90$ was observed beyond $\Theta_{Lab} = 6°$, the Newton diagram supports the assignment of the $m/z = 90$ signal to the H loss channel from benzyl.

Signal at $m/z = 76$ was present at laboratory angles well beyond where $m/z = 90$ was detected and therefore cannot be due to dissociative ionization of C_7H_6. The solid circle in Figure 3.8 represents the maximum center-of-mass velocities for the benzyne fragment and indicates that the $m/z = 76$ fragment should scatter up to a laboratory scattering angle of $\Theta_{Lab} = 21°$. The angular distribution of the $m/z = 76$ fragment supports the assignment of this signal to CH_3 loss from benzyl, channel (3.3), as it was measured out to 18°. The $m/z = 1$ and $m/z = 15$ counter-fragments for the two channels are kinematically allowed at

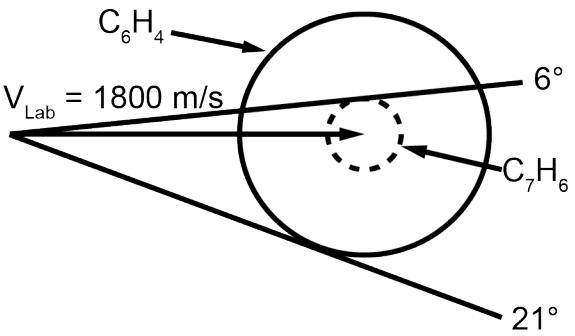

Figure 3.8: Newton diagram for the benzyl photodissociation at 248 nm. Each circle represents the maximum center-of-mass velocities of the photofragment; the dashed circle denotes the C_7H_6 fragment and the solid circle denotes the C_6H_4 fragment. The maximum scattering angles are shown.

all laboratory angles, which, combined with high detector background at these m/z values, prohibited their detection.

The photofragment TOF spectra are governed by the center-of-mass angular and translational energy distribution, $P(E_T, \theta)$. The total distribution can be uncoupled to yield

$$P(E_T, \theta) = P(E_T) \times I(\theta, E_T) \tag{3.6}$$

where $P(E_T)$ is the center-of-mass translational energy distribution and $I(\theta, E_T)$ is the center-of-mass angular distribution. The TOF spectra are analyzed using PHOTRAN,[42] a forward convolution program that simulates the TOF spectra given the center-of-mass angular and translational energy distributions. An initial guess of the $P(E_T)$ distribution is iteratively adjusted until good agreement is reached between the data and the simulation. The analysis assumes that the benzyl radical photodissociation is isotropic, which results in an adequate simulation of the present data. This assumption has been verified by Song et al.[83] for the H loss channel.

Characteristics of the $P(E_T)$ distributions are collected in Table 3.1. Figure 3.9 shows the $P(E_T)$ distribution for H loss; the resulting TOF simulations are shown as solid lines in Figure 3.5. The peak energy is 4 kcal/mol with an average translational energy, $\langle E_T \rangle$, of 7.1 kcal/mol and a maximum translational energy, E_{Tmax}, of 30 kcal/mol. The average fraction of energy that goes into translation, $\langle f_T \rangle$, is 0.2. The peak is very close to 0 kcal/mol and the average translational energy is much lower than the available energy, indicating that the photofragments have a large amount of internal excitation. The $P(E_T)$ extends up to 30 kcal/mol, which is close to the available energy of 35 kcal/mol if fulvenallene is the C_7H_6 fragment. The $P(E_T)$ distribution for H loss from benzyl photodissociation at 254 nm by Song et al.[83] has an average translational energy of 9.2 kcal/mol and is in excellent

Table 3.1: Characteristics of the $P(E_T)$ distributions in Figure 3.9, 3.10 and from Song et al. at 254 nm[83]

channel	peak (kcal/mol)	$\langle E_T \rangle$ (kcal/mol)	E_{Tmax} (kcal/mol)	E_{avail} (kcal/mol)	$\langle f_T \rangle$
H loss	4	7.1	30	35	0.2
H loss from Song et al[83]	5.5	9.2	32.2	35	0.29
CH_3 loss	1	2.9	23	24	0.12

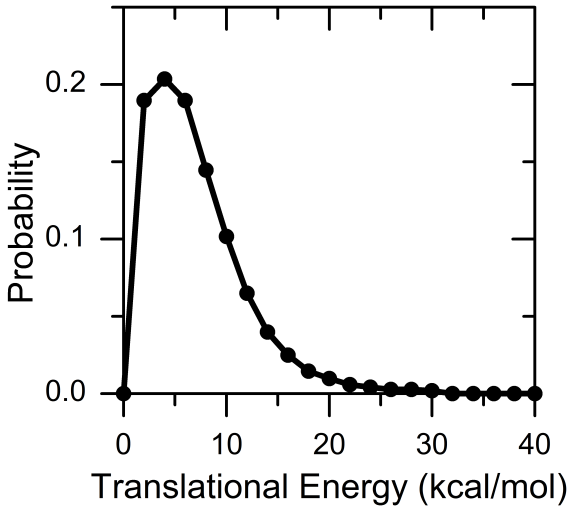

Figure 3.9: Center-of-mass $P(E_T)$ distribution for the benzyl photodissociation to C_7H_6 + H. Details of the $P(E_T)$ distribution can be found in Table 3.1.

agreement with the distribution in Figure 3.9. Its characteristics are also shown in Table 3.1 for comparison.

The $P(E_T)$ distribution for CH_3 loss is shown in Figure 3.10 with the resulting simulations of the $m/z = 76$ TOF spectra shown as solid lines in Figure 3.6. It is peaked at 1 kcal/mol with an average translational energy of 2.9 kcal/mol, an $\langle f_T \rangle$ of 0.12 and extends to a maximum energy of 23 kcal/mol, in agreement with the 24 kcal/mol available energy. The very weak high translational energy component of this distribution, shown in the inset of Figure 3.10, is necessary for agreement between the simulations and all TOF data. Since this $P(E_T)$ distribution was determined from TOF spectra obtained for $\Theta_{Lab} \geq 7°$, points in the $P(E_T)$ distribution below 2 kcal/mol are uncertain. This channel from benzyl photodissociation has not been reported before and there is no $P(E_T)$ with which to compare.

Because of extensive dissociative ionization that occurs from electron impact ionization

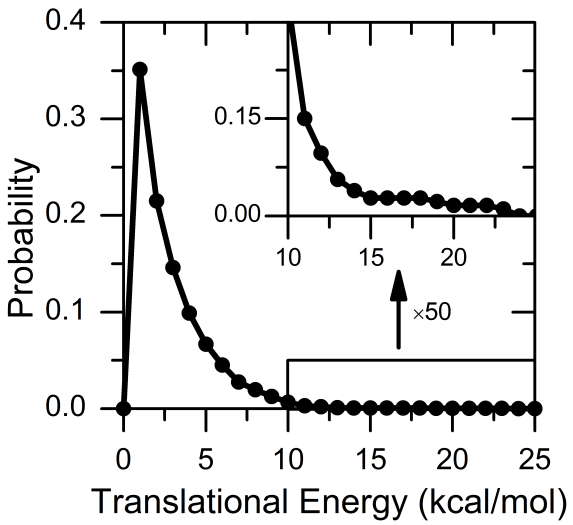

Figure 3.10: Center-of-mass $P(E_T)$ distribution for the benzyl photodissociation to C_6H_4 + CH_3. Details of the $P(E_T)$ distribution can be found in Table 3.1.

at 70 eV, there are m/z values that have components from both H loss and CH_3 loss products, and TOF spectra at these values are useful for estimating branching ratios for the two channels. Within the Newton circle for H loss, the photodissociation signal at $m/z = 74$ and $m/z = 50$ cannot be well simulated by either $P(E_T)$ alone; components from both channels are required for the spectra to be well-simulated. Figure 3.7 shows spectra at $m/z = 74$ and $m/z = 50$ with the total simulation in the solid line and components from each dissociation pathway as dashed and dotted lines.

The branching ratio (BR) between the two channels can be calculated using Equation 3.7.

$$\text{BR } (CH_3 \text{ loss / H loss}) = \frac{W_{CH_3}}{W_H} \times \frac{\sigma_H}{\sigma_{CH_3}} \times \frac{f_H}{f_{CH_3}} \tag{3.7}$$

The weighting of each $P(E_T)$, W_i, in the TOF simulation was determined by matching the total simulation to the data with consistent weighting at all angles. This weighting was then normalized by the ionization cross section, σ_i, of the parent fragment, estimated by the scheme of Fitch and Sauter,[99] and by f_i , the probability that each parent fragment will dissociatively ionize to $m/z = 74$ or $m/z = 50$. This probability was determined by collecting signal at $\Theta_{Lab} = 4°$ for all m/z values with measurable signal intensity (90, 89, 88, 87, 86, 85, 84, 76, 75, 74, 73, 64, 63, 62, 61, 60, 51, 50, 49, 39, 38) and then determining the fraction that appears at the specific m/z value of interest. All of the m/z values mentioned have a component from H loss, but the CH_3 + benzyne channel is only observed at m/z = 76 (40%), 74 (20%), 73 (6%), and 50 (34%) in qualitative agreement with the dominant m/z

values observed with benzyne formed from phenyl photodissociation.[91] Taking all of these factors into account, the experimental branching ratio of CH_3 : H loss is 0.011 ± 0.004. The uncertainty comes from the variation in branching ratio calculated from different angles (4° and 5°) and different masses ($m/z = 74$ and $m/z = 50$). This ratio indicates that H loss is the dominant pathway with only minor contributions from CH_3 loss.

3.5 Discussion

The goal of this study was to assess how the benzyl radical photodissociates after excitation at 248 nm in a collisionless environment with interest in identifying the photofragments and the dissociation mechanism. The results of this study suggest that there are two competing pathways, an H loss pathway and a methyl loss pathway.

The existence of an H loss channel from benzyl has been ascertained by shock tube studies, photodissociation studies and thermolysis studies.[78,79,82,83,100,101] Although the other fragment measured in this experiment at $m/z = 90$ has not been unambiguously identified, theoretical work has suggested that it is most likely the fulvenallene molecule.[51,52,84,86] The identification of an H loss channel is corroborated here by the agreement between the Newton diagram in Figure 3.8 with the angular distribution of signal, and by the excellent agreement between the $P(E_T)$ distribution from Song et al., based on measuring the H atom fragment, with our $P(E_T)$ in Figure 3.9, determined from TOF spectra for the C_7H_6 counter-fragment. We cannot differentiate between the production of fulvenallene and 2-ethynyl cyclopentadiene or distinguish which pathway in Figure 3.1 produces fulvenallene because all of these pathways are energetically very similar.

The methyl loss channel is relatively new to the benzyl dissociation landscape with little mention in the literature. The theoretically reported[51] energetics agree with the extent of the $P(E_T)$ distribution in Figure 3.10. In addition, the assignment of the $m/z = 76$ fragment as benzyne is corroborated by the qualitative agreement with the dissociative ionization pattern measured for this product from phenyl photodissociation.[91] Unfortunately, the corresponding methyl fragment was not detected and thus using conservation of momentum to match the partner fragments was not possible.

The shape of the $P(E_T)$ distributions in Figures 3.9 and 3.10 suggest that the dissociation mechanisms for both H loss and CH_3 loss involve internal conversion to the ground electronic state followed by energy randomization and dissociation. The maximum energy in both distributions agrees with the available energy calculated with ground state products. Time resolved photoionization studies determined an excited state lifetime of 150 fs for the $\tilde{D}^2B_2$ state following excitation at 255 nm and suggested a stepwise internal conversion to the $\tilde{A}/\tilde{B}$ states whose estimated lifetime of less than 2 ps returns the benzyl radical to the ground state.[89,102] Therefore, dissociation on an electronically excited state is unlikely. Both

$P(E_T)$ distributions peak close to zero, which indicates a high degree of internal excitation consistent with energy randomization and dissociation from a bound potential.

If internal conversion to the ground state is followed by rapid intramolecular vibrational redistribution, then RRKM calculations would be a reasonable theoretical framework for experimental comparison. Considering all possible pathways from benzyl as depicted in Figure 3.1, the calculated branching ratio for CH_3 : H loss (combined fulvenallene and 2-ethynyl cyclopentadiene) is 0.027. Omitting any effects of tunneling reduces the rate of any reaction involving H motion; as these transitions are present for both the H loss pathways and the CH_3 loss pathway the effect of including tunneling is unclear. Within the limitations of this analysis, the reported RRKM branching ratio indicates that H loss is the dominant dissociation channel, in good agreement with the experimental branching ratio of 0.011 $\pm$ 0.004. In addition, RRKM calculations showed that fulvenallene is the dominant H loss product over 2-ethynyl cyclopentadiene with a branching ratio of 77:1. Furthermore, RRKM calculations for the formation of acetylene + cyclopentadienyl indicate that it is 46 times less likely to occur than the formation of methyl and benzyne and 1700 times less likely than H loss from benzyl. A more complete RRKM study of the benzyl radical ground state dissociation would be of great interest.

Although the acetylene + cyclopentadienyl channel (3.4) has a lower asymptotic energy than either H atom or and methyl loss, the pathway to its formation has more steps with higher and tighter barriers compared to the other channels.[85] Buckingham et al.[79] claimed to observe both of these species, although they may not be from collisionless primary benzyl dissociation. It is possible that a photon energy higher than 248 nm is necessary for this pathway to occur.

3.6 Conclusion

The photodissociation of the benzyl radical was studied with excitation at 248 nm. There is evidence that supports two dissociation channels: H + C_7H_6, with the C_7H_6 fragment likely to be fulvenallene, and CH_3 + benzyne. Both of these channels have been predicted theoretically and all of the experimental analysis supports the identifications made above. Both dissociation channels occur by internal conversion to the ground state followed by intramolecular vibration energy redistribution and then dissociation. This mechanism is supported by the shape of each $P(E_T)$ distribution and by the agreement between the experimental branching ratio of 0.011 $\pm$ 0.004 in favor of H atom loss with RRKM calculations.

3.7 Acknowledgements

The authors would like to thank Prof. Carlo Cavallotti and Prof. Piergiorgio Casavecchia for helpful discussions. This work was supported by the Director, Office of Basic Energy

Sciences, Chemical Sciences, Geosciences, and Biosciences division of the U.S. Department of Energy under Contract No. DE-AC02-05CH11231.

Chapter 4

Photodissociation of the Cyclopentadienyl Radical at 248 nm

The photodissociation of jet cooled cyclopentadienyl radicals, c-C_5H_5, at 248 nm has been studied using photofragment translational spectroscopy. Two dissociation channels were observed, H + C_5H_4 and C_3H_3 + C_2H_2. The C_5H_4 fragment was identified as ethynylallene by its ionization energy. The translational energy distribution determined for each channel suggests that both dissociation mechanisms occur via internal conversion to the ground electronic state followed by intramolecular vibrational redistribution and dissociation. The experimental branching ratio as well as the RRKM (Rice-Ramsperger-Kassel-Marcus) calculation favors the formation of C_3H_3 + C_2H_2 over the H-atom loss channel. The RRKM calculations also support the observation of ethynylallene as the dominant C_5H_4 product isomer.

4.1 Introduction

The cyclopentadienyl radical (CP), c-C_5H_5, is ubiquitous in hydrocarbon combustion schemes. The importance of CP is rooted in its stability, which allows it to accumulate in combustion environments.[103] The bimolecular reactions of CP in such environments have been studied in order to understand its role in polycyclic aromatic hydrocarbon (PAH) and soot formation.[104–108] Of particular interest are the reactions of CP with acetylene,[85,109,110] CP with itself,[111–115] and CP with H atoms.[116–118] In addition to these bimolecular reactions, unimolecular decay of CP is of interest in combustion and has only been minimally investigated despite the prevalence of this species. This work aims to probe the decomposition of CP by studying its photodissociation after excitation at 248 nm.

Spectroscopic studies of CP have focused on elucidating the nature of its Jahn–Teller distorted ground state and associated vibronic coupling.[119] Initial condensed phase electron paramagnetic resonance (EPR) spectroscopy suggested a permanent structural distor-

tion.[120–122] Miller and co-workers have reported Jahn–Teller coupling constants from their extensive work studying the laser induced fluorescence from the electronically excited $\tilde{A}^2A_2''$ state.[123–127] Further spectroscopic investigations of CP have been carried out using ultrafast electron diffraction,[128] anion photoelectron spectroscopy,[129] and IR spectroscopy in a cryogenic matrix[130] and in He droplets.[131]

The thermal decomposition of CP has only been studied as a secondary reaction from the shock tube pyrolysis of cyclopentadiene.[132–134] Burcat and Dvinyaninov[132] measured the pyrolysis products using a gas chromatograph and flame ionization detector, Kern et al.[133] detected products by time-of-flight mass spectrometry, and Roy et al.[134] used absorption spectroscopy to measure both H-atom and acetylene time profiles. All three investigations proposed that CP decomposed solely to the propargyl radical, C_3H_3, and acetylene, C_2H_2, in a three-step process beginning with a 1,2-hydrogen shift followed by ring opening and ending with dissociation. These previous techniques cannot distinguish between primary CP decomposition products, secondary decomposition products or nonunimolecular reaction products. Other experiments have explored the role of C_5H_5 in bimolecular reactions of C_2H+CH_3CCH, C_2H+H_2CCCH_2, C_2H_2+C_3H_3.[135–137] There have been neither photo-induced fragmentation experiments of CP nor any absorption spectroscopy near 248 nm.

In depth theoretical calculations of CP decomposition were first reported by Moskaleva and Lin,[138] who only considered the pathway to the propargyl radical and acetylene. A more complete potential energy diagram was reported recently by Jamal and Mebel[139] that includes additional decomposition products. A simplified potential energy diagram is shown in Figure 4.1. All pathways begin with a 1,2-hydrogen shift forming the 1,3-cyclopentadien-4-yl radical. This intermediate then ring opens and, depending on which bond breaks, can form either the 1,3,4-pentatrienyl radical or the 1-pentene-4-ynyl radical. From these ring-opened species there are many reaction possibilities, including direct dissociation pathways to form the propargyl radical and acetylene as well as hydrogen atom loss to form ethynylallene or pentadiyne. Additional isomerization and dissociation channels exist, with products including H, CH_3, C_2H, C_3H_4, C_4H_2, and C_5H_4; see Ref 139 for more details. Direct H-atom loss from CP is possible without intervening isomerization, but it has a large energy barrier and thus is not expected to play an important role in thermal decomposition.[139] The channels of interest in this work are:[139]

$$\text{Cyclopentadienyl} \rightarrow \text{propargyl + acetylene} \qquad \Delta H_{0K} = 74.1 \text{ kcal/mol} \tag{4.1}$$

$$\rightarrow \text{ethynylallene + H} \qquad \Delta H_{0K} = 91.0 \text{ kcal/mol} \tag{4.2}$$

$$\rightarrow \text{pentadiyne + H} \qquad \Delta H_{0K} = 95.5 \text{ kcal/mol} \tag{4.3}$$

$$\rightarrow \text{methyl + diacetylene} \qquad \Delta H_{0K} = 78.7 \text{ kcal/mol.} \tag{4.4}$$

In order to gain additional insights into the unimolecular decay of the cyclopentadienyl radical, we have carried out a study of its collisionless ultraviolet photodissociation dynamics

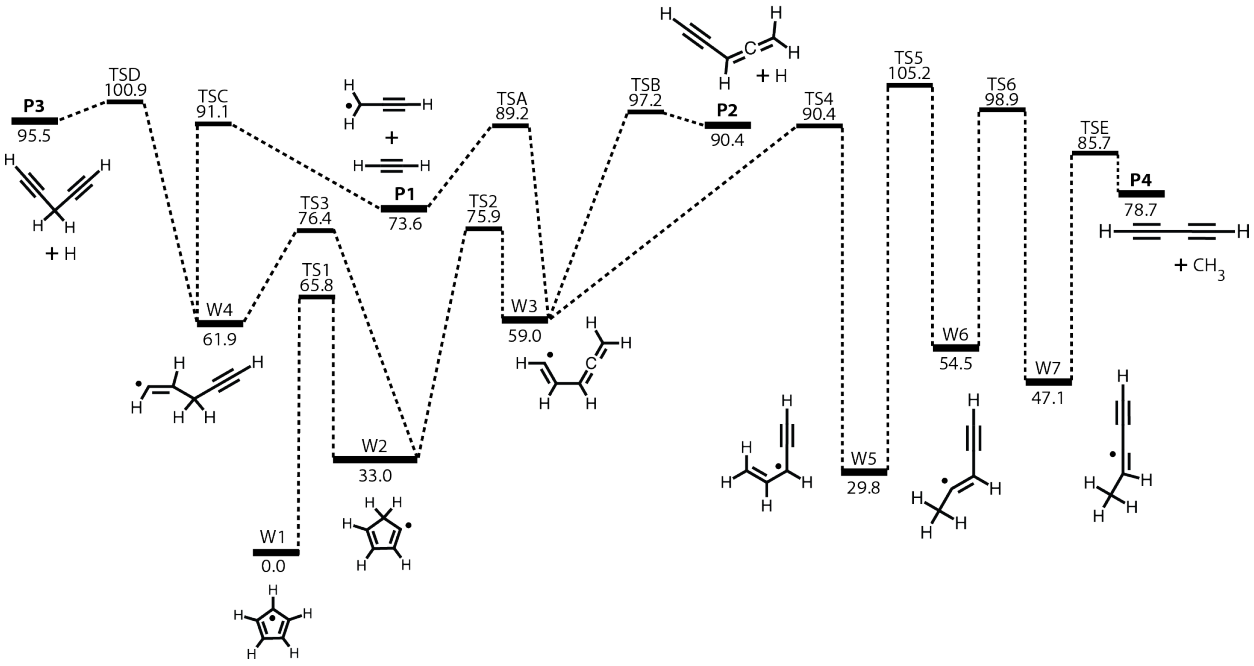

Figure 4.1: A simplified C_5H_5 potential energy diagram showing the production of propargyl + acetylene, ethynylallene + H, pentadiyne + H and diacetylene + methyl. The energetics and pathways are compiled from Refs 138 and 139. All energies are in kcal/mol.

at 248 nm using molecular beam photofragment translational spectroscopy. This experiment can in principle detect all channels and thus determine which processes are occurring. Both Channel 4.1 and Channel 4.2 are observed. The translational energy distributions determined for both channels suggest internal conversion to the ground electronic state followed by statistical decay. The branching ratio between the observed channels is determined and compared to theoretical RRKM calculations.

4.2 Experimental

Cyclopentadienyl radical photodissociation was studied on a modified crossed molecular beam apparatus with a fixed source and rotatable detector as described previously.[34,87,88] A pulsed CP beam was produced by flash pyrolysis of anisole as it passed through a resistively heated SiC tube attached to the nozzle of a piezoelectric pulsed valve.[140,141] Anisole decomposes via a two-step mechanism, first losing a methyl group and then undergoing ring contraction with the loss of CO, to form CP.[142,143]

The pulsed valve was backed with a gas mixture of 1.2 atm of 10% N_2 in He bubbled through an ice-water cooled sample of anisole (Fluka, >99%). The molecular beam was collimated with two skimmers that separate the source chamber from the main scattering chamber. The collimated beam was crossed at 90° by a focused, unpolarized laser pulse with a fluence of 400 mJ/cm^2 at 248 nm from an LPX 220i excimer laser. The pulsed valve and laser were operated at 400 and 200 Hz, respectively, which allowed for background subtraction from the radical beam. The scattered photofragments were detected as a function of laboratory angle, Θ_{Lab}, in the plane defined by the laser and the molecular beam. After passing into a triply differentially pumped detector, the photofragments were ionized via electron impact ionization with 80 eV electrons. The resulting ions were mass-selected with a quadrupole mass filter and detected with a Daly style ion detector.[37] The ion signal as a function of time relative to the laser pulse was acquired with a multichannel scalar interfaced with a computer for $10^5 - 2\times10^6$ laser shots. The time-of-flight (TOF) spectra were simulated using a forward convolution method to iteratively determine the center-of-mass translational energy distributions for each product channel.

Mass spectra of the molecular beam were used to verify anisole depletion (m/z = 108) and CP formation (m/z = 65); examples are shown in Figure 4.2. The upper trace is the precursor mass spectrum taken with pyrolysis off; the parent peak is visible at m/z = 108. With pyrolysis on, the parent peak disappears and the resulting mass spectrum (lower trace) is dominated by the CP parent mass. Because of dissociative ionization, there is a daughter peak at m/z = 65 from the precursor molecule in the upper trace of Figure 4.2. However,

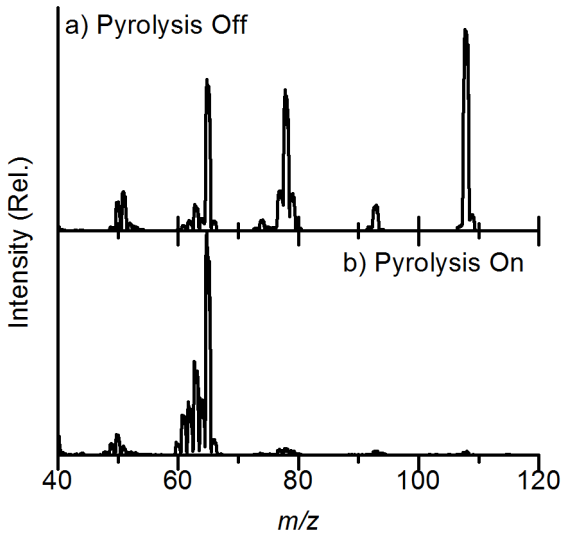

Figure 4.2: Mass spectra of the molecular beam normalized to the signal intensity at m/z = 65; a) pyrolysis off, b) pyrolysis on. The peak at m/z = 108 disappears with pyrolysis on indicating depletion of the precursor.

once the $m/z = 108$ peak is depleted, it is expected that the $m/z = 65$ peak comes solely from CP.

Further confirmation of CP formation is shown by the ionization efficiency curves for $m/z = 65$ in Figure 4.3. The signal intensity at $m/z = 65$ was measured as the electron ionization energy was varied from 5 eV up to 20 eV while keeping the emission current constant. The energy scale was calibrated by the ionization of N_2 in the molecular beam. The appearance energy is the extrapolated intercept from the linear region of the curve. The appearance energy for signal at $m/z = 65$ with pyrolysis off is 14.6 eV, which indicates it is due to dissociative ionization, while with pyrolysis on the appearance energy of 8.7 eV matches the known ionization energy of 8.6 eV for CP.[144]

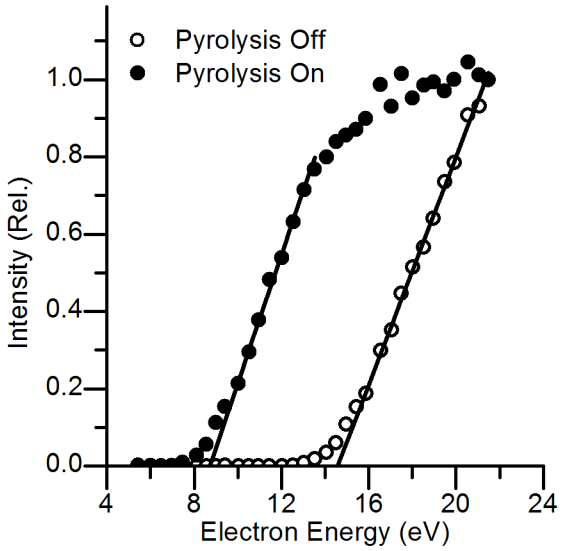

Figure 4.3: Ionization efficiency curves of $m/z = 65$ with pyrolysis off and on. The appearance potential for this signal with pyrolysis off is 14.6 eV, whereas with pyrolysis on, it is 8.7 eV.

The CP beam velocity was characterized with a spinning slotted chopper wheel. Typical beam velocities were around 2000 m/s with speed ratios, defined as the beam flow velocity divided by the velocity spread, in the range of 3–5.

4.3 RRKM Calculations

Rice-Ramsperger-Kassel-Marcus (RRKM) calculations have been performed as a comparison to the experimental observations. The stationary points of interest are depicted on the potential energy diagram in Figure 4.1 and are collected from Refs 138 and 139. The densities and sums of states for each local minimum and transition state were calculated using the Beyer-Swinehart algorithm[97] with the reported energies and vibrational frequencies

treated as harmonic oscillator frequencies. Internal rotations in W3, W4, W6, W7, TS10, TSA, TSC, and TSE were treated as free rotors in calculating the densities and sums of states.[145] Individual rate constants were calculated using the micro-canonical RRKM equation. The maximum energy was given by the photon energy (115 kcal/mol). No tunneling effects were considered. All reaction pathways shown in Figure 4.1 were considered, with the steady-state approximation on the intermediate local minima, to solve for the relative rates of each channel.

4.4 Results

Based on our expectation that Channels 4.1–4.4 are the main dissociation channels, time-of-flight (TOF) spectra were taken at parent m/z values for these channels (m/z = 64, 50, 39, 26, and 15) and for several other m/z values that could result from dissociative ionization (DI) of these parent species.

TOF spectra were measured at $m/z = 64$, $C_5H_4^+$, at laboratory angles $\Theta_{Lab} = 3°$, 4°, 5°, 6°, 7°, 8°,and 10° with respect to the molecular beam axis. Selected small angle TOF spectra are shown as open circles in Figure 4.4. The $m/z = 64$ species was further characterized by measurement of its ionization efficiency curve at $\Theta_{Lab} = 4°$ shown in Figure 4.5. The on-axis $m/z = 64$ signal with an appearance energy of 13.6 eV is due to the dissociative ionization of CP. The off-axis $m/z = 64$ signal comes from the ionized parent fragment of the photodissociation of CP and the appearance energy of 9.4 eV matches the ionization energy of 9.2 eV for ethynylallene, the heavier fragment from Channel 4.2.[146] The other potential fragment with parent ion signal at $m/z = 64$, pentadiyne, has an ionization energy of 10.3 eV;[146] a contribution from this channel to the $m/z = 64$ signal cannot be ruled out based on Figure 4.5 alone.

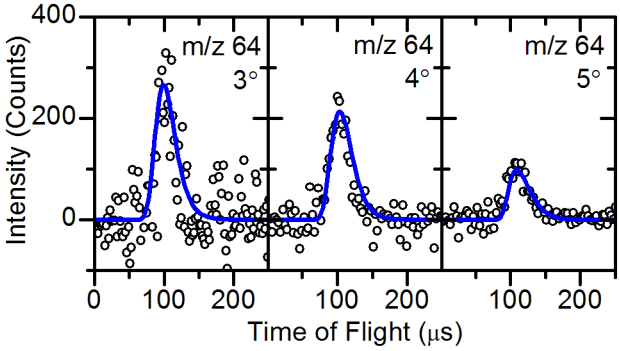

Figure 4.4: Representative TOF spectra of $m/z = 64$ at 3°, 4°, and 5°. The open circles are data points and the blue line is a simulation based on the $P(E_T)$ distribution in Figure 4.8. Counts are normalized to 10^5 laser shots.

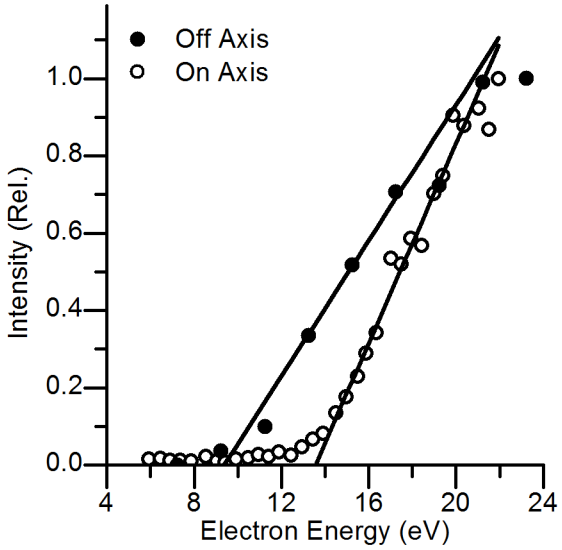

Figure 4.5: Ionization efficiency curves of $m/z = 64$ on and off of the molecular beam axis. The off-axis signal was measured at $\Theta_{Lab} = 4°$. The appearance potential for the signal on axis is 13.6 eV, whereas off axis it is 9.4 eV.

TOF spectra at $m/z = 39$, $C_3H_3^+$, and $m/z = 26$, $C_2H_2^+$, were detected at laboratory angles ranging from $\Theta_{Lab} = 4°$ up to 30°. Representative spectra are shown in Figure 4.6. If these signals indeed correspond to Channel 4.1, it should be possible to simulate them with the same photofragment translational energy distribution, i.e., they are "momentum-matched", as discussed in more detail in Section 4.5.

Investigation of Channel 4.4 was conducted at $m/z = 50$ and 15. TOF spectra at $m/z = 50$ were essentially identical to the $m/z = 64$ spectra, indicating that the signal at $m/z = 50$ was from dissociative ionization of C_5H_4. Attempts to detect signal at $m/z = 15$ were unsuccessful.

Figure 4.7 shows TOF spectra taken for ion signals with $m/z = 24$ and 25. These signals can result from DI of the products from Channels 4.1–4.3. As such, they are used to determine the product branching ratio as discussed in Section 4.5.

Other sources of signal besides CP photodissociation were assessed. It is conceivable that there is a small contribution to our TOF spectra from the photodissociation of the radical precursor, anisole, since it is not completely depleted in the molecular beam. From photodissociation studies of anisole with the pyrolysis source off, the dominant signal appears at $m/z = 65$. With pyrolysis on, the dominant signal occurs at $m/z = 64$ and there is very little signal at $m/z = 65$ off of the beam axis.

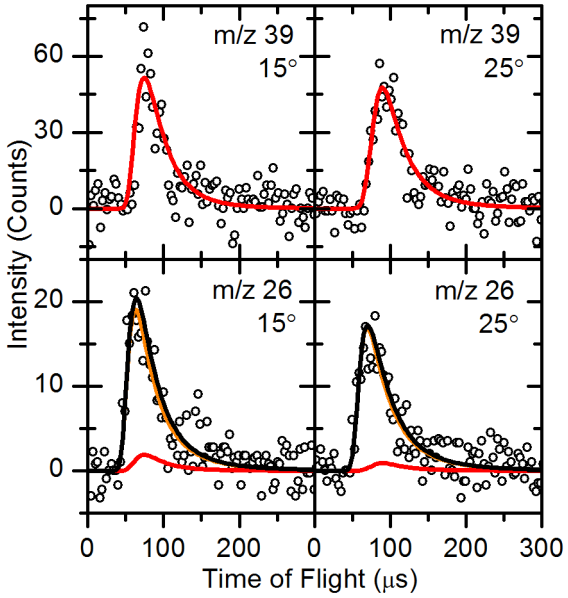

Figure 4.6: Representative TOF spectra of $m/z = 39$ and 26. The data are shown as open circles. The solid lines are simulations based on the $P(E_T)$ distribution in Figure 4.9; the red line is from C_3H_3 and the orange line is from C_2H_2. Both fragments contribute to the $m/z = 26$; the total simulated signal is indicated by the black line. Counts are normalized to 10^5 laser shots.

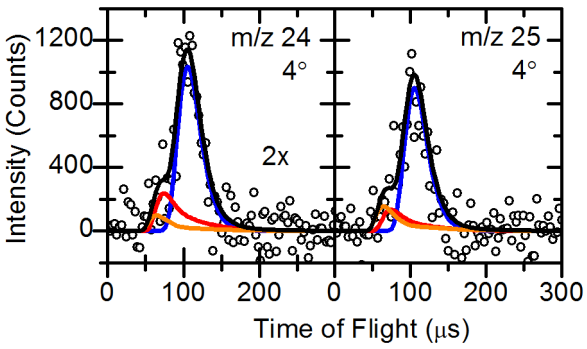

Figure 4.7: TOF spectra of $m/z = 24$ and 25 collected at $\Theta_{Lab} = 4°$. The data are shown as open circles. The black line is the summed simulation, which has three components: the orange and red lines are from the C_2H_2 and C_3H_3 components, respectively, of the $P(E_T)$ distribution in Figure 4.9, and the blue line comes from the C_5H_4 component of the $P(E_T)$ distribution in Figure 4.8. Both spectra were taken for 2×10^6 laser shots.

Possible contributions from two photon processes were assessed by conducting a laser power dependence study. TOF spectra taken over the range of 33 mJ/cm^2 to 667 mJ/cm^2 showed a linear signal intensity dependence on laser power and no qualitative differences in the shape of the TOF spectra.

4.5 Analysis

The TOF spectra and off-axis ionization data in the previous section suggest that CP photodissociation results in Channels 4.1 and 4.2, and possibly Channel 4.3. In this section, we use kinematic analysis to confirm that these channels are present, and characterize them through their center-of-mass (CM) translational energy distributions.

Conservation of energy in this experiment is expressed by

$$E_{avail} = h\nu + E_0 - D_0 = E_{int} + E_T \tag{4.5}$$

The available energy to the photoproducts, E_{avail}, is the sum of photon energy, $h\nu$, and any initial internal energy, E_0, minus the dissociation energy, D_0, for the specific channel. This available energy can be partitioned into either the internal energy, E_{int}, or the relative translational energy, E_T, of the fragments. The initial internal energy of CP following supersonic jet expansion is unknown but is approximated as zero for the purposes of analysis, which is supported by our previous work on phenyl radical expansions seeded in He with 10% N_2.[91]

When all of the available energy is partitioned into translational energy, the maximum laboratory scattering angle for each photofragment can be calculated with knowledge of the CP beam velocity. Kinematic analysis shows that for Channel 4.2, the $m/z = 64$ ethynylallene fragment cannot scatter beyond $\Theta_{Lab} = 6°$, based on the radius of the Newton Circle for this channel.[28] The TOF spectra at $m/z = 64$ below $\Theta_{Lab} = 6°$ comprise only a single dominant feature as shown in Figure 4.4, which supports the assignment of this $m/z = 64$ feature to H-atom loss from CP. Beyond $\Theta_{Lab} = 6°$ this dominant feature disappears and there is a faster, less intense feature that extends past where H-atom loss can occur. It is possible that this feature contributes to the $m/z = 64$ signal within the Newton circle for H-atom loss, but we have assumed that its contribution is minimal in our analysis. For more discussion on this feature see Section 4.9. The $m/z = 1$ counter fragment for Channels 4.2 and 4.3 is kinematically allowed at all laboratory angles, which combined with high detector background at m/z =1, short residence time in the ionization region, and small ionization cross-section prohibited its detection.

Signals at $m/z = 26$ and 39 are present beyond where $m/z = 64$ was detected and therefore cannot be due to the dissociative ionization of C_5H_4. Further, the parent ions at $m/z = 26$ and 39 from Channel 4.1 are kinematically allowed at all measurable laboratory angles and these fragments were detected at all laboratory angles out to $\Theta_{Lab} = 30°$.

The photofragment TOF spectra are governed by the center-of-mass angular and translational energy distribution, $P(E_T, \theta)$. The total distribution can be uncoupled to yield

$$P(E_T, \theta) = P(E_T) \times I(\theta, E_T) \tag{4.6}$$

where $P(E_T)$ is the center-of-mass translational energy distribution and $I(\theta, E_T)$ is the center-of-mass angular distribution. The TOF spectra are analyzed using PHOTRAN,[42] a forward convolution program that simulates the TOF spectra given the center-of-mass angular and translational energy distributions. An initial guess of the $P(E_T)$ distribution is iteratively adjusted until good agreement is reached between the data and the simulation. The analysis assumes that CP photodissociation is isotropic, which results in an adequate simulation of the present data.

Figure 4.8 shows the $P(E_T)$ distribution for H-atom loss; the resulting TOF simulations are shown as blue lines in Figure 4.4. The peak energy is 5 kcal/mol with an average translational energy, $\langle E_T \rangle$, of 8 kcal/mol. The maximum translational energy, $E_{T,max}$, was set to 24 kcal/mol to agree with available energy for Channel 4.2. The average fraction of energy that goes into translation, $\langle f_T \rangle$ is 0.33. The average translational energy is much lower than the available energy, which indicates that the photofragments have a high degree of internal excitation.

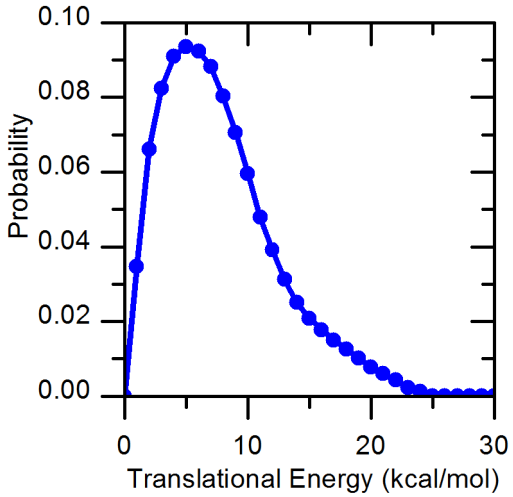

Figure 4.8: Center-of-mass $P(E_T)$ distribution for cyclopentadienyl photodissociation to C_5H_4 + H.

The $P(E_T)$ distribution for Channel 4.1 is shown in Figure 4.9 with the resulting simulations of both m/z = 39 and 26 shown as solid lines in Figure 4.6. It is peaked at 8 kcal/mol with $\langle E_T \rangle$ = 10 kcal/mol and $\langle f_T \rangle$ = 0.24. The $P(E_T)$ distribution extends to a maximum translational energy of 33 kcal/mol, which is within the available energy of 40.9

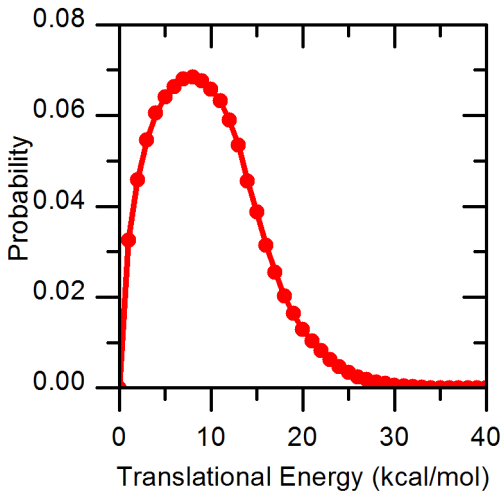

Figure 4.9: Center-of-mass $P(E_T)$ distribution for cyclopentadienyl photodissociation to C_3H_3 + C_2H_2.

kcal/mol for this channel. We find that the TOF spectra for both fragments can be simulated by the same $P(E_T)$ distribution. This is a signature of "momentum-matching", i.e., the two fragments are formed with equal and opposite momenta as required if they originate from the same dissociation event. This observation thus supports the assignment of these features to Channel 4.1. The weighting of each fragment in the simulation of the $m/z = 26$ TOF spectra in Figure 4.6 is set so the branching ratio between C_3H_3 and C_2H_2 is unity as calculated from rearranging Equation 4.7 (below) and solving for the weightings.

Because of extensive dissociative ionization that occurs from electron impact ionization at 80 eV, there is signal from m/z values that have components from both H-atom loss and C_3H_3 + C_2H_2. TOF spectra at these m/z values are useful for estimating the branching ratio between these channels. Within $\Theta_{Lab} = 6°$, where signal from Channels 4.1 and 4.2 can occur, the photodissociation signal at $m/z = 24$ and 25 cannot be well simulated by either $P(E_T)$ alone; components from both channels are required for the spectra to be well-simulated. Figure 4.7 shows spectra at $m/z = 24$ and 25 with the total simulation in the black line and components from each dissociation pathway as blue, red and orange lines.

The branching ratio (BR) between the two pathways can be calculated using equation 4.7.

$$\mathrm{BR}\left(\frac{C_3H_3 + C_2H_2}{C_5H_4 + H}\right) = \frac{W_{C_3H_3 \text{ or } C_2H_2}}{W_{C_5H_4}} \times \frac{\sigma_{C_5H_4}}{\sigma_{C_3H_3 \text{ or } C_2H_2}} \times \frac{f_{C_5H_4}}{f_{C_3H_3 \text{ or } C_2H_2}} \qquad (4.7)$$

The weighting of each $P(E_T)$, W_i, in the TOF simulation was determined by matching the total simulation to the data. This weighting was then normalized by the ionization cross

section, σ_i, of the parent fragment estimated by the scheme of Fitch and Sauter,[99] and by f_i, the probability that each parent fragment will dissociatively ionize to $m/z = 24$ or 25. For the C_5H_4 fragment, this probability was determined by collecting signal at $\Theta_{Lab} = 6°$ for all m/z values with measurable signal intensity (64, 63, 62, 61, 60, 52, 51, 50, 49, 48, 39, 38, 37, 36, 26, 25, 24). The integrated signal that was simulated by the $P(E_T)$ distribution from Figure 4.8 was used to determine the dissociative ionization pattern of the C_5H_4 fragment which is reported in Section 4.9. The acetylene fragmentation pattern was taken from NIST[147] and the propargyl fragmentation pattern was calculated in a previous study on this apparatus.[148,149] Taking all of these factors into account, the experimental branching ratio of Channel 4.1 : Channel 4.2+4.3 is 64% : 36% . The uncertainty in this calculation will be discussed in Section 4.6.

The branching ratio calculated using Equation 4.7 can be compared with the results given by the RRKM calculation that represents the statistical ground state dissociation mechanism. All calculated rate constants are below 10^{11} s^{-1}, which should allow enough time for vibrational energy redistribution. The RRKM analysis predicts the branching ratio of Channel 4.1 : Channel 4.2+4.3 is 97% : 3%. The statistical branching ratios between the other channels were also calculated. For the two H-atom loss pathways, the ratio was calculated to be 99% Channel 4.2 : 1% Channel 4.3, and the Channel 4.1 : Channel 4.4 ratio is 99.9996 % : 0.0004%. Hence, both experiment and theory predict Channel 4.1 to be the dominant pathway, followed by Channel 4.2. The numerical disagreement between experiment and theory for the Channel 4.1 : Channel 4.2 ratio is considered in Section 4.6

4.6 Discussion

The goal of this study was to assess how the cyclopentadienyl radical, CP, photodissociates after excitation at 248 nm in a collisionless environment with interest in identifying the photofragments and the dissociation mechanism. The results of this study suggest that there are two competing pathways, an H-atom loss pathway and an acetylene and propargyl pathway.

The existence of an H-atom loss channel from CP was previously inferred from bimolecular reactions on the C_5H_5 potential energy surface but was never measured directly from CP.[136] The fragment measured in this experiment at $m/z = 64$ was identified as ethynylallene by the agreement with its ionization energy. This identification is further supported by RRKM calculations that predict ethynylallene as the dominant C_5H_4 product from CP dissociation. The production of ethynylallene is assigned to Channel 4.2, H-atom loss from CP, which is corroborated by the agreement of the angular distribution of the $m/z = 64$ signal with the maximum expected scattering angle.

Although the acetylene and propargyl channel dominates the literature for CP decomposition, only the acetylene fragment has been previously detected from the secondary

decomposition of cyclopentadiene. In this experiment, both $m/z = 39$ and $m/z = 26$ were measured and since the TOF spectra at both m/z values were simulated by the respective fragments of the $P(E_T)$ distribution in Figure 4.9, they come from the same dissociation event of CP. Furthermore, the maximum translational energy in the $P(E_T)$ distribution of Figure 4.9 agrees with the energetic constraints for Channel 4.1.

Channel 4.4, methyl + diacetylene, has a lower asymptotic energy than both H-atom loss pathways,[139] but the pathway to its formation has more steps with higher and more constrained barriers compared to the other channels. The lack of signal from this channel is supported by the RRKM calculation, which suggests that this channel should account for much less than 1% of the total dissociation.

The shape of the $P(E_T)$ distributions in Figures 4.8 and 4.9 suggest that the dissociation mechanisms for both pathways involve internal conversion to the ground electronic state followed by energy randomization and dissociation over a barrier. The peak positions in Figures 4.8 and 4.9 are shifted away from 0 kcal/mol, which is indicative of exit barriers on the potential energy surface. From Figure 4.1, there are exit barriers of 15.6 kcal/mol and 6.8 kcal/mol for Channels 4.1 and 4.2 respectively, which are reflected in the $P(E_T)$ distributions where the larger exit barrier corresponds to a peak at higher translational energy; the peak positions are 8 kcal/mol and 5 kcal/mol in the $P(E_T)$ distributions corresponding to Channels 4.1 and 4.2 respectively.

The $P(E_T)$ distribution of Figure 4.8 was constructed to simulate the TOF spectra in Figure 4.4. However, in addition to an H-atom loss feature, these spectra may include a component from the same process that produces the high angle $m/z = 64$ feature. Nevertheless, the TOF spectra require an H-atom loss component because they cannot be simulated by a $P(E_T)$ with a mass ratio smaller than 64:1 (see Section 4.9). The exact weighting of each of these components in the TOF spectra cannot be determined, which leads to uncertainty in the $P(E_T)$ distribution of Figure 4.8.

If internal conversion to the ground state is followed by rapid intramolecular vibrational redistribution, then the experimental branching ratios should be similar to those calculated by RRKM theory. While both the experimental and calculated branching ratios favor Channel 4.1 and find Channel 4.2 to be the only other significant reaction, the experimentally determined amount of Channel 4.2 is considerably higher than the calculated value. We do not think this discrepancy implies non-statistical dissociation dynamics, given the overall form of the $P(E_T)$ distributions. However, there are two possible sources of error in the experimental branching ratio that may be significant. First, the experimental branching ratio is very sensitive to the extent of ethynylallene dissociative ionization to $m/z = 24$ and 25. As shown in Figure 4.13, these m/z values each constitute only 2% of the total DI signal and therefore small changes in the fragmentation pattern used in Equation 4.7 can lead to large changes in the branching ratio. Similarly, the fragmentation pattern of propargyl, which is

used to set the acetylene–propargyl branching ratio to unity, can be a source of error since $m/z = 24$ and 25 constitute just 2% and 3% of the total propargyl DI signal. In TOF spectra at other m/z values (26, 37-39) where there is more DI, background levels are significantly higher and lead to poorer signal-to-noise. Secondly, the "high angle" signal at $m/z = 64$ may contribute to the TOF spectra within the Newton circle for Channel 4.2, thus increasing the apparent contribution of this channel to the overall dissociation yield. As discussed in Section 4.9, this signal can be simulated with a $P(E_T)$ distribution for C_5H_4 + H fragments that extends beyond the maximum value allowed for Channel 4.2, but the origin of this signal is unclear. This dissociation channel could be studied further on an apparatus that can detect H-atoms.[150,151] Given these considerations, the experimental branching ratio is likely to have more systematic error than the RRKM calculation and should be taken as an upper bound for the contribution of Channel 4.2 to the overall photodissociation yield.

4.7 Conclusion

Photodissociation of the cyclopentadienyl radical was studied upon excitation at 248 nm. There is evidence that supports two dissociation channels: H + C_5H_4, with the C_5H_4 fragment being ethynylallene, and C_3H_3 + C_2H_2. Both dissociation channels are attributed to internal conversion to the ground state followed by intramolecular vibrational energy redistribution and dissociation. This mechanism is supported by the shape of each $P(E_T)$ distribution. The experimental branching ratio as well as RRKM calculations favor the formation of C_3H_3 + C_2H_2 over the H-atom loss channel.

4.8 Acknowledgements

This work was supported by the Director, Office of Basic Energy Sciences, Chemical Sciences, Geosciences, and Biosciences division of the U.S. Department of Energy under contract DE-AC02-05CH11231.

4.9 Supplemental Information

4.9.1 High Angle $m/z = 64$

From Figure 4.10, it is clear that there is another component that is contributing to the $m/z = 64$ TOF spectra. It is not possible that this signal is due to H-atom loss from CP because energetically $m/z = 64$ cannot extend beyond $\Theta_{Lab} = 6°$. We were able to simulate this feature with $P(E_T)$ distributions with fragments of $m/z = 93 + 15$ (as if from the anisole precursor), $m/z = 65 + 28$ (as if from phenoxyl), and $m/z = 102 + 26$ (as if from naphthalene). We do not believe that this signal is coming from any of those possibilities. Precursor photodissociation exhibits a dominant feature at $m/z = 65$, however with the

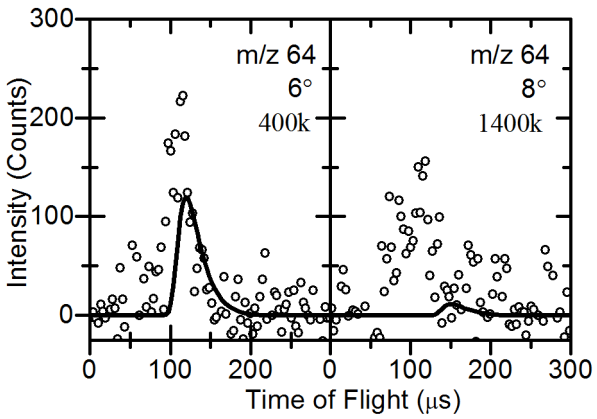

Figure 4.10: TOF spectra of $m/z = 64$ at $\Theta_{Lab} = 6°$ and 8°. The data are shown as open circles and the solid line is the simulation from the $P(E_T)$ in Figure 4.8 for H-atom loss from CP. The $\Theta_{Lab} = 6°$ spectrum was taken for 4×10^5 laser shots while the $\Theta_{Lab} = 8°$ spectrum was taken for 1.4×10^6 laser shots.

pyrolysis on, $m/z = 65$ signal is considerably weaker than that of $m/z = 64$; this discrepancy rules out precursor. If this signal was coming from the phenoxyl radical photodissociation, we would expect to see $m/z = 65$ because the CP parent mass is the dominant fragment after ionization. Since there is more $m/z = 64$ than $m/z = 65$, the additional signal cannot stem from CP as a photofragment. Although naphthalene has been discussed as a product of CP self-reactions, it is not present in our beam (i.e., there is no signal observed at $m/z = 128$). An additional option is to simulate this feature with fragments of $m/z = 64 + 1$, but with energies above the theoretical limit. The simulations from this scenario are shown in Figure 4.11 with the distribution in Figure 4.12

Even with all of these options for simulating the high angle ($\Theta_{Lab} > 6°$) $m/z = 64$ TOF spectra, none of these possibilities can simulate the slow edge of the $\Theta_{Lab} = 6°$ spectra. In order to simulate this slow edge, the mass ratio in the $P(E_T)$ needs to be large. Therefore, there is still a need for the existence of the H-atom loss $P(E_T)$ to simulate the slow edge at $\Theta_{Lab} = 6°$.

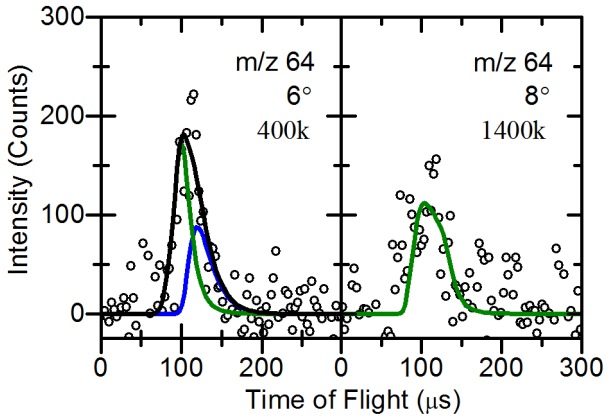

Figure 4.11: TOF spectra of $m/z = 64$ at $\Theta_{Lab} = 6°$ and $8°$. The data are shown as open circles and the green line is the simulation from the $P(E_T)$ distribution in Figure 4.12, the blue line is the simulation from the $P(E_T)$ in Figure 4.8 and the black line is the total simulation. The number of laser shots per spectrum is indicated on the plot.

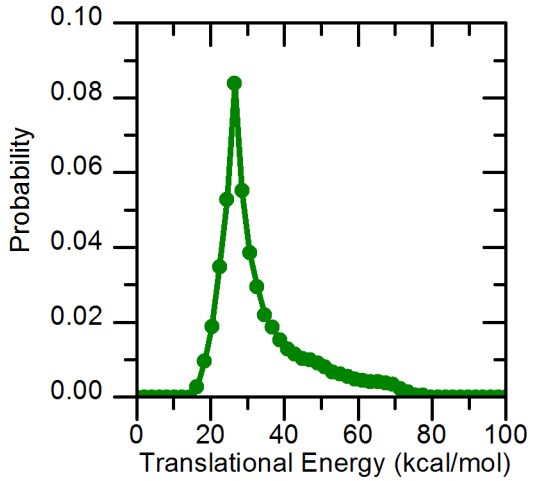

Figure 4.12: Center-of-mass $P(E_T)$ distribution that produces simulations in Figure 4.11 with fragments of mass 64 and 1.

4.9.2 Ethynylallene Fragmentation Pattern

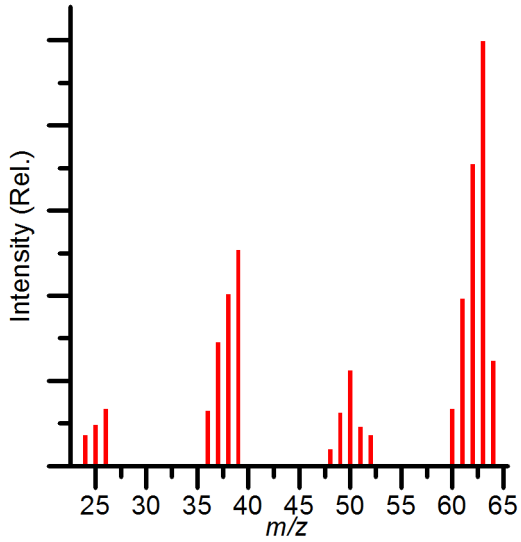

Figure 4.13: Recorded fragmentation pattern of ethynylallene. This pattern was determined by collecting signal at $\Theta_{Lab} = 6°$ for all m/z values with measurable signal intensity (64, 63, 62, 61, 60, 52, 51, 50, 49, 48, 39, 38, 37, 36, 26, 25, 24). The integrated signal that was simulated by the $P(E_T)$ distribution from Figure 4.8 was used to determine this dissociative ionization pattern.

Chapter 5

Conclusions

In addition to the benzyl and cyclopentadienyl radicals, the photodissociation of the phenyl radical, c-C_6H_5,[91] and the fulvenallenyl radical, C_7H_5,[149] has been studied. This entire collection of molecules forms the basis for the following concluding remarks.

5.1 Molecules Studied

The radicals that comprise the collection of molecules studied have many similarities. They are all cyclic alkenyl hydrocarbons, containing 5 or 6 member carbon rings and they are all resonantly stabilized with 3 or more resonance structures for each radical. These classifications will be used to draw conclusions in section 5.4.

In addition to these similarities, these radicals are all involved in the toluene decomposition mechanism. As discussed in the introduction, modeling combustion of realistic fuels is incredibly challenging. One simplifying technique for modeling combustion is to start with a single fuel molecule. Toluene is often chosen as a model fuel because it is a simple branched aromatic hydrocarbon. Its thermal decomposition and reactions in a flame have been extensively studied and modeled.[48–50]

The decomposition pathway of toluene is shown in Figure 5.1. The reactions included are collected from both theoretical calculations and experimental observations described in Refs 91, 149, 152, 153 and Chapter 4. The first tier of the mechanism begins with toluene, which can dissociate to either the phenyl radical and a methyl radical or to the benzyl radical and an H-atom. The second tier of the mechanism includes the dissociation of both phenyl and benzyl. The phenyl radical can break up into either benzyne and an H-atom or acetylene and a C_4H_3 radical, most likely 1-buten-3-ynyl. The benzyl radical has three proposed dissociation channels: 1) fulvenallene and an H-atom, 2) benzyne and a methyl radical, and 3) the cyclopentadienyl radical and acetylene. The third tier of the toluene decomposition mechanism includes the further dissociation of cyclopentadienyl and

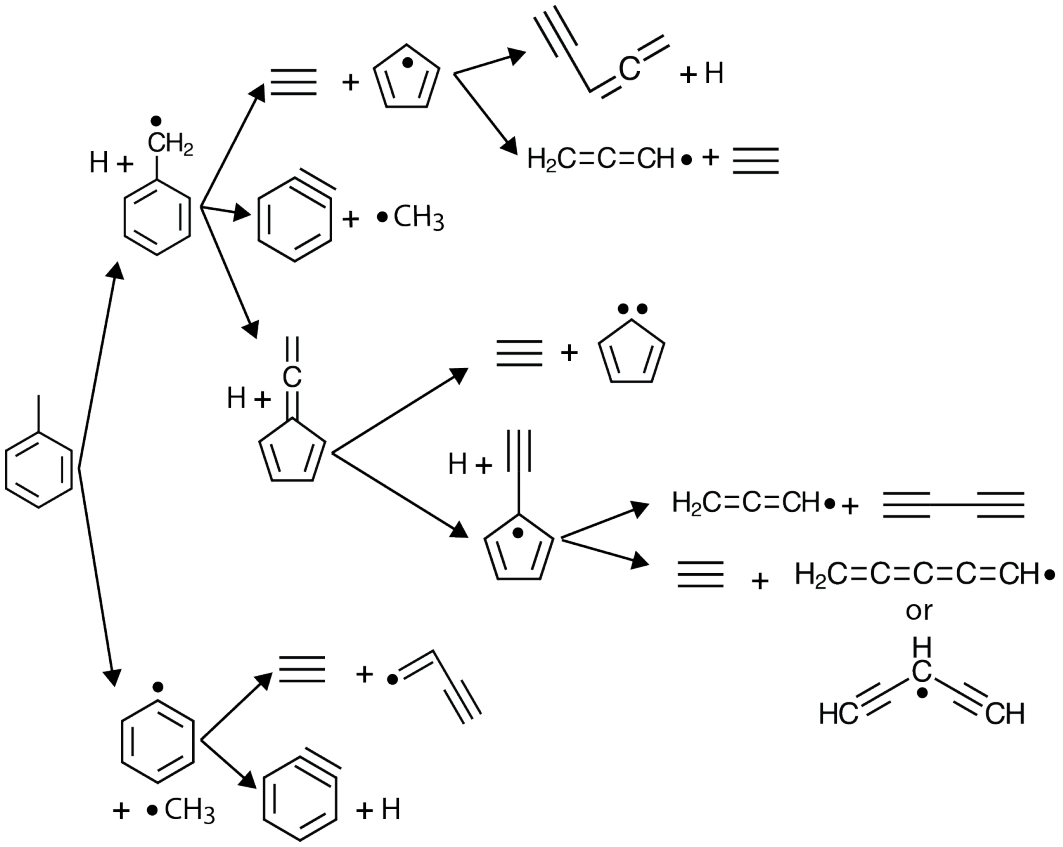

Figure 5.1: The decomposition pathways of toluene collected from Refs 91, 149, 152, 153 and Chapter 4.

fulvenallene. The cyclopentadienyl radical can dissociate to either ethynylallene and an H-atom or the propargyl radical and acetylene. Fulvenallene can fragment either to the fulvenallenyl radical and an H-atom or to cyclopentadienylidene and acetylene. The final tier in Figure 5.1 is the dissociation of the fulvenallenyl radical, which can break apart into propargyl and diacetylene or acetylene and a C_5H_3 radical.

The radicals, benzyl, fulvenallenyl, phenyl, and cyclopentadienyl, and their dissociation reactions are integral components in the toluene decomposition mechanism.

5.2 Radical Production

This work demonstrates the utility of the flash pyrolysis source initially described by Kohn.[43] It was implemented in the B Machine by B. Negru to study the phenyl radical photodissociation.[87] Since then, it has been used to produce many other radical species including benzyl, cyclopentadienyl, cyclohexyl, CH_3S, and CH_3SS.

As a general observation, this technique for generating radicals works best with stabilized radicals, which is evident by the ease of production of both benzyl and cyclopentadienyl. The stabilization results in decomposition pathways that are prohibitively high in energy for the pyrolysis source and therefore further dissociation of the radicals does not occur.

The fulvenallenyl radical is an outlier in this collection because it was produced by the photodissociation of fulvenallene.

5.3 Photodissociation Results

The photodissociation of benzyl, fulvenallenyl, phenyl and cyclopentadienyl were carried out at 248 nm. The $P(E_T)$ distribution for each dissociation channel was determined and the peak of that distribution as well as the average translational energy of the distribution are reported in Table 5.1. Also reported for comparison is the exit barrier for each dissociation channel. The value reported is based on ab initio calculations and represents the most likely (or two most likely) pathway(s) determined by RRKM calculations.

Table 5.1: Photodissociation results of benzyl, fulvenallenyl, phenyl and cyclopentadienyl at 248 nm.

Channel	Peak in $P(E_T)$ (kcal/mol)	Exit Barrier (kcal/mol)	$\langle E_T \rangle$ (kcal/mol)	$\langle f_T \rangle$
$C_7H_7 \rightarrow C_7H_6 + H$ [a]	4	4.5	7.1	0.2
$C_7H_7 \rightarrow C_6H_4 + CH_3$ [a]	1	0	6	0.17
$C_7H_5 \rightarrow C_5H_3 + C_2H_2$ [b]	7	~ 16	12.1	0.16
$C_7H_5 \rightarrow C_4H_2 + C_3H_3$ [b]	6	8.4 or 10.7	9.1	0.13
$C_6H_5 \rightarrow C_6H_4 + H$ [c]	2	0	6	0.17
$C_5H_5 \rightarrow C_5H_4 + H$ [d]	5	6.8	8	0.33
$C_5H_5 \rightarrow C_3H_3 + C_2H_2$ [d]	8	15.6	10	0.24

[a] Ref. 153; [b] Ref. 149; [c] Ref.91; [d] This work

All of the dissociation mechanisms for the channels listed in Table 5.1 are the same. The radical internally converts to the ground state and then dissociation occurs. Quantitatively, the fraction of available energy that goes into translational energy, $\langle f_T \rangle$, is small, ranging from 0.33–0.16. For comparison, the photodissociation of CH_3SS results in S–S cleavage with an $\langle f_T \rangle$ of 0.78,[154] which is attributed to dissociation on an excited repulsive state. Additionally, all of the peak positions of the $P(E_T)$ distributions listed in Table 5.1 are close to 0 kcal/mol. In contrast, the peak position from the $P(E_T)$ distribution for $CH_3SS \rightarrow CH_3S + S$ is 28 kcal/mol.

The assignment of ground state statistical dissociation is also corroborated by the agreement of the experimental and theoretical RRKM branching ratios for the competing pathways of benzyl, fulvenallenyl and cyclopentadienyl.

The comparison of the C5 through C7 hydrocarbons with CH_3SS highlights the collective similarities amongst these hydrocarbons.

Furthermore, as shown in Figure 5.2, there is a direct correlation between the size of the exit barrier and the shape of the $P(E_T)$ distribution, measured by the peak and $\langle E_T \rangle$. As the exit barrier increases, the peak position shifts further away from 0 kcal/mol and the average translational energy increases. This correlation again supports the assignment of these mechanisms to ground state dissociation since the exit barriers are calculated on the ground state. In addition, this correlation supports the general understanding of reaction dynamics where the exit barrier promotes energy partitioning into relative translational energy.

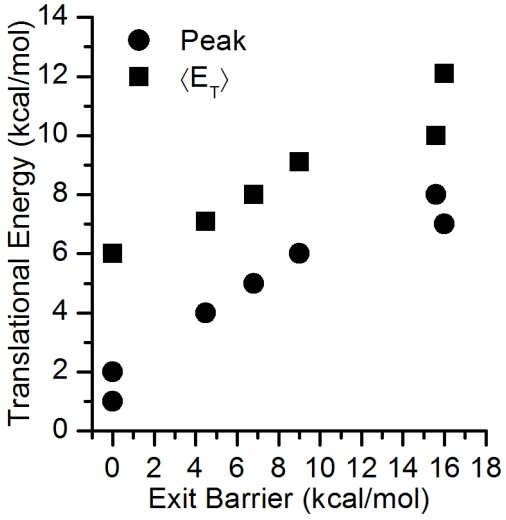

Figure 5.2: Comparison of the exit barrier for each dissociation channel with the peak position and $\langle E_T \rangle$ of the $P(E_T)$ distribution.

5.4 Conclusion

Photodissociation of the benzyl, fulvenallenyl, phenyl and cyclopentadienyl radicals has been studied at 248 nm. Based on each individual experiment, all dissociation channels are attributed to internal conversion to the ground state followed by intramolecular vibrational redistribution and dissociation. In each case, this mechanism is supported by the shape of the $P(E_T)$ distribution as well as the branching ratio comparisons with RRKM theory for

benzyl, fulvenallenyl and cyclopentadienyl radicals. Furthermore, the shape of the $P(E_T)$ distribution is largely effected by the exit barrier on the ground state potential energy surface.

To generalize the work here, photodissociation of cyclic alkenyl hydrocarbons with 5–7 carbon atoms results in ground state statistical dissociation.

5.5 Future Directions

The question on the mechanism of cyclic alkenyl hydrocarbon photodissociation has been answered. With the specialized apparatus for photofragment translational spectroscopy, the next step is to explore different classes of molecules where the mechanism of their photodissociation is still in question. Two possible classes of molecules to examine include heterocyclic radicals, such as pyridyl radical, or peroxyl radical species, such as peroxyl acetyl radical. I leave this endeavor in the capable hands of the next generation of graduate students.

Bibliography

[1] G. Wald, "The molecular basis of visual excitation," *Nature*, vol. 219, pp. 800–807, 1968.

[2] S. Chapman, "The photochemistry of atmospheric oxygen," *Rep. Prog. Phys.*, vol. 9, no. 1, p. 92, 1942.

[3] T. Baer and W. L. Hase, *Unimolecular Reaction Dynamics*. Oxford University Press, 1996.

[4] L. J. Butler and D. M. Neumark, "Photodissociation dynamics," *J. Phys. Chem.*, vol. 100, no. 31, pp. 12801–12816, 1996.

[5] R. Schinke, *Photodissociation Dynamics*. Cambridge University Press, 1993.

[6] C. B. Moore and I. W. M. Smith, "State-resolved studies of reactions in the gas phase," *J. Phys. Chem.*, vol. 100, no. 31, pp. 12848–12865, 1996.

[7] J. P. Simons, "Photodissociation: a critical survey," *J. Phys. Chem.*, vol. 88, no. 7, pp. 1287–1293, 1984.

[8] G. Odian, *Principles of Polymerization*. John Wiley & Sons, 2004.

[9] P. Lightfoot, R. Cox, J. Crowley, M. Destriau, G. Hayman, M. Jenkin, G. Moortgat, and F. Zabel, "Organic peroxy radicals: Kinetics, spectroscopy and tropospheric chemistry," *Atmos. Environ. Part A.*, vol. 26, no. 10, pp. 1805 – 1961, 1992.

[10] F. Battin-Leclerc, "Detailed chemical kinetic models for the low-temperature combustion of hydrocarbons with application to gasoline and diesel fuel surrogates," *Prog. Energy Combust. Sci.*, vol. 34, no. 4, pp. 440 – 498, 2008.

[11] R. D. Levine, *Molecular Reaction Dynamics*. Cambridge University Press, 2005.

[12] G. C. Eiden and J. C. Weisshaar, "Vibronic coupling mechanism in the $\tilde{A}^2A_2 - \tilde{B}^2B_2$ excited states of benzyl radical," *J. Chem. Phys.*, vol. 104, no. 22, pp. 8896–8912, 1996.

[13] R. Sivaramakrishnan, R. S. Tranter, and K. Brezinsky, "High pressure pyrolysis of toluene. 2. modeling benzyl decomposition and formation of soot precursors," *J. Phys. Chem. A*, vol. 110, no. 30, pp. 9400–9404, 2006.

[14] T. R. Barfknecht, "Toxicology of soot," *Prog. Energy Combust. Sci.*, vol. 9, no. 3, pp. 199–237, 1983.

[15] A. Msaad, A. Belcadi, M. Mahdaoui, E. Aaffas, and M. Mouqalid, "Reduced detailed mechanism for methane combustion," *Energy Power Eng.*, vol. 4, no. 1, pp. 28–33, 2012.

[16] W. Dabelstein, A. Reglitzky, A. Schütze, and K. Reders, "Automotive fuels," in *Ullmann's Encyclopedia of Industrial Chemistry*, Wiley-VCH Verlag GmbH & Co. KGaA, 2000.

[17] P. Atkins and J. de Paula, *Atkins' Physical Chemistry*. Oxford University Press, 2006.

[18] V. Engel, V. Staemmler, R. L. Vander Wal, F. F. Crim, R. J. Sension, B. Hudson, P. Andresen, S. Hennig, K. Weide, and R. Schinke, "Photodissociation of water in the first absorption band: a prototype for dissociation on a repulsive potential energy surface," *J. Phys. Chem.*, vol. 96, no. 8, pp. 3201–3213, 1992.

[19] W. Domcke and D. R. Yarkony, "Role of conical intersections in molecular spectroscopy and photoinduced chemical dynamics," *Annu. Rev. Phys. Chem.*, vol. 63, no. 1, pp. 325–352, 2012.

[20] G. Herzberg, *Molecular Spectra and Molecular Structure; Volume III. Electronic Spectra and Electronic Structure of Polyatomic Molceulares*. D. Van Nostrand Company Inc., 1966.

[21] G. van Veen, K. Mohamed, T. Baller, and A. de Vries, "Photofragmentation of H_2S in the first continuum," *Chem. Phys.*, vol. 74, no. 2, pp. 261 – 271, 1983.

[22] K. Weide, V. Staemmler, and R. Schinke, "Nonadiabatic effects in the photodissociation of H_2S," *J. Chem. Phys.*, vol. 93, no. 1, pp. 861–862, 1990.

[23] R. Continetti, B. Balko, and Y. Lee, "Photodissociation of H_2S and the HS radical at 193.3 nm," *Chem. Phys. Lett.*, vol. 182, no. 5, pp. 400 – 405, 1991.

[24] R. A. Marcus and O. K. Rice, "The kinetics of the recombination of methyl radicals and iodine atoms.," *J. Phys. Chem.*, vol. 55, no. 6, pp. 894–908, 1951.

[25] G. E. Busch, J. F. Cornelius, R. T. Mahoney, R. I. Morse, D. W. Schlosser, and K. R. Wilson, "Photofragment spectrometer," *Rev. Sci. Instrum.*, vol. 41, no. 7, pp. 1066–1073, 1970.

[26] M. N. R. Ashfold, I. R. Lambert, D. H. Mordaunt, G. P. Morley, and C. M. Western, "Photofragment translational spectroscopy," *J. Phys. Chem.*, vol. 96, no. 7, pp. 2938–2949, 1992.

[27] D. R. Herschbach, "Reactive collisions in crossed molecular beams," *Discuss. Faraday Soc.*, vol. 33, pp. 149–161, 1962.

[28] D. R. Herschbach, "Reactive scattering in molecular beams," in *Advances in Chemical Physics*, pp. 319–393, John Wiley & Sons, Inc., 1966.

[29] X. Zhao, *Photodissociation of Cyclic Compounds in a Molecular Beam.* Ph.d. dissertation, University of California, Berkeley, 1989.

[30] R. Weiss, "Molecular beam electron bombardment detector," *Rev. Sci. Instrum.*, vol. 32, no. 4, pp. 397–401, 1961.

[31] K. Kuhnke, K. Kern, R. David, and G. Comsa, "High efficiency molecular-beam ionization detector with short ionization region," *Rev. Sci. Instrum.*, vol. 65, no. 11, pp. 3458–3465, 1994.

[32] R. N. Zare and D. R. Herschbach, "Doppler line shape of atomic fluorescence excited by molecular photodissociation," *Proc. IEEE*, vol. 51, pp. 173–182, Jan 1963.

[33] R. N. Zare, "Photoejection dynamics," *Mol. Photochem.*, vol. 4, no. 1, pp. 1–37, 1972.

[34] Y. T. Lee, J. D. McDonald, P. R. LeBreton, and D. R. Herschbach, "Molecular beam reactive scattering apparatus with electron bombardment detector," *Rev. Sci. Instrum.*, vol. 40, no. 11, pp. 1402–1408, 1969.

[35] J. C. Robinson, *Photofragment Translational Spectroscopy Studies of Unsaturated Hydrocarbons.* Ph.d. dissertation, University of California, Berkeley, 2002.

[36] N. C. Cole-Filipiak, *Production and Photodissociation of Neutral Free Radicals.* Ph.d. dissertation, University of California, Berkeley, 2015.

[37] N. R. Daly, "Scintillation type mass spectrometer ion detector," *Rev. Sci. Instrum.*, vol. 31, no. 3, pp. 264–267, 1960.

[38] R. Ekman, J. Silberring, A. M. Westman-Brinkmalm, and A. Kraj, eds., *Mass Spectrometry: Instrumentation, Interpretation, and Applications.* John Wiley & Sons, 2008.

[39] G. Scholes, ed., *Atomic and Molecular Beam Methods, Volume I.* Oxford University Press, 1988.

[40] D. Krajnovich, *Molecular Beam Studies of Photodissociation Reactions.* Ph.d. dissertation, University of California, Berkeley, 1983.

[41] OPTEK, Carrollton, Texas, *Photologic Slotted Optical Switch: OPB920, OPB970, OPB980, OPB990 Series*, 2008.

[42] S. A. Harich, *PHOTRAN, a program for forward convolution analysis of photodissociation.* 2003.

[43] D. W. Kohn, H. Clauberg, and P. Chen, "Flash pyrolysis nozzle for generation of radicals in a supersonic jet expansion," *Rev. Sci. Instrum.*, vol. 63, no. 8, pp. 4003–4005, 1992.

[44] Q. Guan, K. N. Urness, T. K. Ormond, D. E. David, G. B. Ellison, and J. W. Daily, "The properties of a micro-reactor for the study of the unimolecular decomposition of large molecules," *Int. Rev. Phys. Chem.*, vol. 33, no. 4, pp. 447–487, 2014.

[45] D. Proch and T. Trickl, "A high-intensity multi-purpose piezoelectric pulsed molecular beam source," *Rev. Sci. Instrum.*, vol. 60, no. 4, pp. 713–716, 1989.

[46] B. Negru, *Photodissociation Dynamics of Neutral Free Radicals.* Ph.d. dissertation, University of California, Berkeley, 2012.

[47] W. M. Davis, S. M. Heck, and H. O. Pritchard, "Theoretical study of benzyl radical reactivity in combustion systems," *J. Chem. Soc. Faraday Trans.*, vol. 94, no. 18, pp. 2725–2728, 1998.

[48] M. B. Colket and D. J. Seery, "Reaction mechanisms for toluene pyrolysis," *Symp. (Int.) Combust. [Proc.]*, vol. 25, no. 1, pp. 883–891, 1994.

[49] V. Detilleux and J. Vandooren, "Experimental and kinetic modeling evidences of a C_7H_6 pathway in a rich toluene flame," *J. Phys. Chem. A*, vol. 113, no. 41, pp. 10913–10922, 2009.

[50] Z. Tian, W. J. Pitz, R. Fournet, P.-A. Glaude, and F. Battin-Leclerc, "A detailed kinetic modeling study of toluene oxidation in a premixed laminar flame," *Proc. Combust. Inst.*, vol. 33, no. 1, pp. 233–241, 2011.

[51] M. Derudi, D. Polino, and C. Cavallotti, "Toluene and benzyl decomposition mechanisms: elementary reactions and kinetic simulations," *Phys. Chem. Chem. Phys.*, vol. 13, no. 48, pp. 21308–21318, 2011.

[52] D. Polino and M. Parrinello, "Combustion chemistry via metadynamics: benzyl decomposition revisited," *J. Phys. Chem. A*, vol. 119, no. 6, pp. 978–989, 2015.

[53] H. Schler, L. Reinebeck, and R. Koberle, "Über das auftreten von gemeinsamen bruchstücken (mehratomige radikale?) bei benzolderivaten in der glimmentladung," *Z. Naturforsch. A: Phys. Sci.*, vol. 7, no. 6, pp. 421–427, 1952.

[54] F. Bayrakceken and J. E. Nicholas, "A flash photolytic study of the benzyl and alpha-chlorobenzyl radicals," *J. Chem. Soc. (B)*, no. 0, pp. 691–694, 1970.

[55] G. Porter and M. I. Savadatti, "The electronic spectra of benzyl - a new transition," *Spectrochim. Acta, Part A*, vol. 22, no. 5, pp. 803–806, 1966.

[56] M. E. Jacox, "Vibrational and electronic energy levels of polyatomic transient molecules," in *NIST Chemistry WebBook, NIST Standard Reference Database Number 69* (P. Linstom and W. Mallard, eds.), Gaithersburg MD, 20899: National Institute of Standards and Technology.

[57] T. Okamura, T. R. Charlton, and B. A. Thrush, "Laser-induced fluorescence of benzyl radicals in the gas phase," *Chem. Phys. Lett.*, vol. 88, no. 4, pp. 369–371, 1982.

[58] J. I. Selco and P. G. Carrick, "Jet cooled emission spectra of toluene and the benzyl radical," *J. Mol. Spectrosc.*, vol. 137, no. 1, pp. 13–23, 1989.

[59] M. Fukushima and K. Obi, "Jet spectroscopy of benzyl and benzyl-α-d_2," *J. Chem. Phys.*, vol. 96, no. 6, pp. 4224–4232, 1992.

[60] T.-Y. D. Lin, X.-Q. Tan, T. M. Cerny, J. M. Williamson, D. W. Cullin, and T. A. Miller, "High-resolution fluorescence excitation spectra of jet-cooled benzyl and p-methylbenzyl radicals," *Chem. Phys.*, vol. 167, no. 1-2, pp. 203–214, 1992.

[61] K. Tonokura and M. Koshi, "Cavity ring-down spectroscopy of the benzyl radical," *J. Phys. Chem. A*, vol. 107, no. 22, pp. 4457–4461, 2003.

[62] C. Cossart-Magos and S. Leach, "Determination of the symmetry of the first excited electronic state of benzyl by rotational contour analysis of vibronic bands of the emission spectra of $C_6H_5CH_2$, $C_6H_5CD_2$, and $C_6D_5CD_2$," *J. Chem. Phys.*, vol. 56, no. 4, pp. 1534–1545, 1972.

[63] C. Cossart-Magos and S. Leach, "Two-mode vibronic interaction between neighboring 1^2A_2 and 2^2B_2 excited electronic states of the benzyl radical," *J. Chem. Phys.*, vol. 64, no. 10, pp. 4006–4019, 1976.

[64] G. Orlandi, G. Poggi, and F. Zerbetto, "Vibronic coupling in the benzyl radical," *Chem. Phys. Lett.*, vol. 115, no. 3, pp. 253–258, 1985.

[65] F. Negri, G. Orlandi, F. Zerbetto, and M. Z. Zgierski, "Quantum chemical and vibronic analysis of the 1^2B_2-1^2A_2, 2^2B_2 transition in benzyl-h_7 and benzyl-d_7 radicals," *J. Chem. Phys.*, vol. 93, no. 1, pp. 600–608, 1990.

[66] A. A. Boyd, B. Noziere, and R. Lesclaux, "Kinetics and thermochemistry of the reversible combination reactions of the allyl and benzyl radicals with NO," *J. Phys. Chem.*, vol. 99, no. 27, pp. 10815–10823, 1995.

[67] A. Matsugi and A. Miyoshi, "Kinetics of the self-reactions of benzyl and o-xylyl radicals studied by cavity ring-down spectroscopy," *Chem. Phys. Lett.*, vol. 521, no. 0, pp. 26–30, 2012.

[68] G. da Silva and J. W. Bozzelli, "Kinetic modeling of the benzyl + HO_2 reaction," *Proc. Combust. Inst.*, vol. 32, no. 1, pp. 287–294, 2009.

[69] G. da Silva, M. R. Hamdan, and J. W. Bozzelli, "Oxidation of the benzyl radical: mechanism, thermochemistry, and kinetics for the reactions of benzyl hydroperoxide," *J. Chem. Theory Comput.*, vol. 5, no. 12, pp. 3185–3194, 2009.

[70] A. Matsugi and A. Miyoshi, "Computational study on the recombination reaction between benzyl and propargyl radicals," *Int. J. Chem. Kinet.*, vol. 44, no. 3, pp. 206–218, 2012.

[71] A. Matsugi and A. Miyoshi, "Reactions of o-benzyne with propargyl and benzyl radicals: potential sources of polycyclic aromatic hydrocarbons in combustion," *Phys. Chem. Chem. Phys.*, vol. 14, no. 27, pp. 9722–9728, 2012.

[72] G. da Silva and J. W. Bozzelli, "Kinetics of the benzyl + $O(^3P)$ reaction: a quantum chemical/statistical reaction rate theory study," *Phys.Chem. Chem. Phys.*, vol. 14, no. 46, pp. 16143–16154, 2012.

[73] R. D. Smith, "A direct mass spectrometric study of the mechanism of toluene pyrolysis at high temperatures," *J. Phys. Chem.*, vol. 83, no. 12, pp. 1553–1563, 1979.

[74] D. L. Baulch, C. T. Bowman, C. J. Cobos, R. A. Cox, T. Just, J. A. Kerr, M. J. Pilling, D. Stocker, J. Troe, W. Tsang, R. W. Walker, and J. Warnatz, "Evaluated kinetic data for combustion modeling: Supplement II," *J.of Phys. Chem. Ref. Data*, vol. 34, no. 3, pp. 757–1397, 2005.

[75] J. Jones, G. B. Bacskay, and J. C. Mackie, "Decomposition of the benzyl radical: quantum chemical and experimental (shock tube) investigations of reaction pathways," *J. Phys. Chem. A*, vol. 101, no. 38, pp. 7105–7113, 1997.

[76] M. A. Oehlschlaeger, D. F. Davidson, and R. K. Hanson, "High-temperature thermal decomposition of benzyl radicals," *J. Phys. Chem. A*, vol. 110, no. 21, pp. 6649–6653, 2006.

[77] R. Sivaramakrishnan, M. C. Su, and J. V. Michael, "H- and D-atom formation from the pyrolysis of $C_6H_5CH_2Br$ and $C_6H_5CD_2Br$: Implications for high-temperature benzyl decomposition," *Proc. Combust. Inst.*, vol. 33, no. 1, pp. 243–250, 2011.

[78] J. M. Lemieux, *Thermal decomposition of molecules relevant to combustion and chemical vapor deposition by flash pyrolysis time of flight mass spectrometry.* Ph.d. dissertation, University of California, Riverside, 2013.

[79] G. T. Buckingham, T. K. Ormond, J. P. Porterfield, P. Hemberger, O. Kostko, M. Ahmed, D. J. Robichaud, M. R. Nimlos, J. W. Daily, and G. B. Ellison, "The thermal decomposition of the benzyl radical in a heated micro-reactor. I. Experimental findings," *J. Chem. Phys.*, vol. 142, no. 4, p. 044307, 2015.

[80] M. Damm, F. Deckert, and H. Hippler, "Collisional deactivation of vibrationally highly excited benzyl radicals," *Ber. Bunsen-Ges. Phys. Chem.*, vol. 101, no. 12, pp. 1901–1908, 1997.

[81] M. Damm, F. Deckert, H. Hippler, and G. Rink, "Specific rate constants for the fragmentation of vibrationally excited benzyl radicals," *Phys. Chem. Chem. Phys.*, vol. 1, no. 1, pp. 81–90, 1999.

[82] R. Fröchtenicht, H. Hippler, J. Troe, and J. P. Toennies, "Photon-induced unimolecular decay of the benzyl radical: first direct identification of the reaction pathway to C_7H_6," *J. Photochem. Photobiol.*, vol. 80, no. 1-3, pp. 33–37, 1994.

[83] Y. Song, X. Zheng, M. Lucas, and J. Zhang, "Ultraviolet photodissociation dynamics of the benzyl radical," *Phys. Chem. Chem. Phys.*, vol. 13, no. 18, pp. 8296–8305, 2011.

[84] G. da Silva, J. A. Cole, and J. W. Bozzelli, "Thermal decomposition of the benzyl radical to fulvenallene (C_7H_6) + H," *J. Phys. Chem. A*, vol. 113, no. 21, pp. 6111–6120, 2009.

[85] G. da Silva, J. A. Cole, and J. W. Bozzelli, "Kinetics of the cyclopentadienyl + acetylene, fulvenallene + H, and 1-ethynylcyclopentadiene + H reactions," *J. Phys. Chem. A*, vol. 114, no. 6, pp. 2275–2283, 2010.

[86] C. Cavallotti, M. Derudi, and R. Rota, "On the mechanism of decomposition of the benzyl radical," *Proc. Combust. Inst.*, vol. 32, no. 1, pp. 115–121, 2009.

[87] B. Negru, S. J. Goncher, A. L. Brunsvold, G. M. P. Just, D. Park, and D. M. Neumark, "Photodissociation dynamics of the phenyl radical via photofragment translational spectroscopy," *J. Chem. Phys.*, vol. 133, no. 7, p. 074302, 2010.

[88] B. Negru, G. M. P. Just, D. Park, and D. M. Neumark, "Photodissociation dynamics of the tert-butyl radical via photofragment translational spectroscopy at 248 nm," *Phys. Chem. Chem. Phys.*, vol. 13, no. 18, pp. 8180–8185, 2011.

[89] M. Margraf, B. Noller, C. Schrter, T. Schultz, and I. Fischer, "Time- and frequency-resolved photoionization of the C^2A_2 state of the benzyl radical, C_7H_7," *J. Chem. Phys.*, vol. 133, no. 7, p. 074304, 2010.

[90] W. A. Noyes, *Organic Syntheses*, vol. II. Wiley & Sons, 1943.

[91] N. C. Cole-Filipiak, M. Shapero, B. Negru, and D. M. Neumark, "Revisiting the photodissociation dynamics of the phenyl radical," *J. Chem. Phys.*, vol. 141, no. 10, p. 104307, 2014.

[92] R. F. Pottie and F. P. Lossing, "Free radicals by mass spectrometry. xxiii. mass spectra of benzyl and α-d_2-benzyl free radicals," *J. Amer. Chem. Soc.*, vol. 83, no. 12, pp. 2634–2636, 1961.

[93] G. C. Eiden and J. C. Weisshaar, "Adiabatic ionization potential of benzyl radical by two-color resonant two-photon ionization," *J. Phys. Chem.*, vol. 95, no. 16, pp. 6194–6197, 1991.

[94] M. J. Frisch, G. W. Trucks, H. B. Schlegel, G. E. Scuseria, M. A. Robb, J. R. Cheeseman, G. Scalmani, V. Barone, B. Mennucci, G. A. Petersson, H. Nakatsuji, M. Caricato, X. Li, H. P. Hratchian, A. F. Izmaylov, J. Bloino, G. Zheng, J. L. Sonnenberg, M. Hada, M. Ehara, K. Toyota, R. Fukuda, J. Hasegawa, M. Ishida, T. Nakajima, Y. Honda, O. Kitao, H. Nakai, T. Vreven, J. A. Montgomery Jr., J. E. Peralta, F. Ogliaro, M. J. Bearpark, J. Heyd, E. N. Brothers, K. N. Kudin, V. N. Staroverov, R. Kobayashi, J. Normand, K. Raghavachari, A. P. Rendell, J. C. Burant, S. S. Iyengar, J. Tomasi, M. Cossi, N. Rega, N. J. Millam, M. Klene, J. E. Knox, J. B. Cross, V. Bakken, C. Adamo, J. Jaramillo, R. Gomperts, R. E. Stratmann, O. Yazyev, A. J. Austin, R. Cammi, C. Pomelli, J. W. Ochterski, R. L. Martin, K. Morokuma, V. G. Zakrzewski, G. A. Voth, P. Salvador, J. J. Dannenberg, S. Dapprich, A. D. Daniels, . Farkas, J. B. Foresman, J. V. Ortiz, J. Cioslowski, and D. J. Fox, *Gaussian 09*. Wallingford, CT, USA: Gaussian, Inc., 2009.

[95] H. J. Werner, P. J. Knowles, G. Knizia, F. R. Manby, M. Schtz, P. Celani, T. Korona, R. Lindh, A. Mitrushenkov, G. Rauhut, K. R. Shamasundar, T. B. Adler, R. D. Amos, A. Bernhardsson, A. Berning, D. L. Cooper, M. J. O. Deegan, A. J. Dobbyn, F. Eckert, E. Goll, C. Hampel, A. Hesselmann, G. Hetzer, T. Hrenar, G. Jansen, C. Kppl, Y. Liu, A. W. Lloyd, R. A. Mata, A. J. May, S. J. McNicholas, W. Meyer, M. E. Mura, A. Nickla, D. P. O'Neill, P. Palmieri, D. Peng, K. Pflger, R. Pitzer, M. Reiher, T. Shiozaki, H. Stoll, A. J. Stone, R. Tarroni, T. Thorsteinsson, and M. Wang, *MOLPRO version 2008.1, a package of ab initio program.*

[96] J. M. L. Martin, "Ab initio total atomization energies of small molecules — towards the basis set limit," *Chem. Phys. Lett.*, vol. 259, no. 5–6, pp. 669–678, 1996.

[97] T. Beyer and D. F. Swinehart, "Algorithm 448: number of multiply-restricted partitions," *Commun. ACM*, vol. 16, no. 6, p. 379, 1973.

[98] W. M. Haynes, ed., *CRC Handbook of Chemistry and Physics, 96th ed.* CRC Press, 2015.

[99] W. L. Fitch and A. D. Sauter, "Calculation of relative electron impact total ionization cross sections for organic molecules," *Anal.Chem.*, vol. 55, no. 6, pp. 832–835, 1983.

[100] M. Braun-Unkhoff, P. Frank, and T. Just, "High temperature reactions of benzyl radicals," *Ber. Bunsen-Ges. Phys. Chem.*, vol. 94, no. 11, pp. 1417–1425, 1990.

[101] V. S. Rao and G. B. Skinner, "Formation of hydrogen atoms in pyrolysis of ethylbenzene behind shock waves. rate constants for the thermal dissociation of the benzyl radical," *Symp. (Int.) Combust. [Proc.]*, vol. 21, no. 1, pp. 809–814, 1988.

[102] M. Zierhut, B. Noller, T. Schultz, and I. Fischer, "Excited-state decay of hydrocarbon radicals, investigated by femtosecond time-resolved photoionization: ethyl, propargyl, and benzyl," *J. Chem. Phys.*, vol. 122, no. 9, p. 094302, 2005.

[103] R. G. Butler and I. Glassman, "Cyclopentadiene combustion in a plug flow reactor near 1150K," *Proc. Combust. Inst.*, vol. 32, no. 1, pp. 395–402, 2009.

[104] C. Cavallotti, D. Polino, A. Frassoldati, and E. Ranzi, "Analysis of some reaction pathways active during cyclopentadiene pyrolysis," *J. Phys. Chem. A*, vol. 116, no. 13, pp. 3313–3324, 2012.

[105] D. Wang and A. Violi, "Radical–molecule reactions for aromatic growth: a case study for cyclopentadienyl and acenaphthylene," *J. Org. Chem.*, vol. 71, no. 22, pp. 8365–8371, 2006.

[106] D. Wang, A. Violi, D. H. Kim, and J. A. Mullholland, "Formation of naphthalene, indene, and benzene from cyclopentadiene pyrolysis: a DFT study," *J. Phys. Chem. A*, vol. 110, no. 14, pp. 4719–4725, 2006.

[107] F. Xu, X. Shi, Q. Zhang, and W. Wang, "Mechanism for the growth of polycyclic aromatic hydrocarbons from the reactions of naphthalene with cyclopentadienyl and indenyl," *Chemosphere*, vol. 162, pp. 345–354, 2016.

[108] A. Comandini and K. Brezinsky, "Radical/π bond addition between o-benzyne and cyclic C5 hydrocarbons," *J. Phys. Chem. A*, vol. 116, no. 4, pp. 1183–1190, 2012.

[109] S. Fascella, C. Cavallotti, R. Rota, and S. Carr, "The peculiar kinetics of the reaction between acetylene and the cyclopentadienyl radical," *J. Phys. Chem. A*, vol. 109, no. 33, pp. 7546–7557, 2005.

[110] C. Cavallotti, S. Mancarella, R. Rota, and S. Carr, "Conversion of C5 into C6 cyclic species through the formation of C7 intermediates," *J. Phys. Chem. A*, vol. 111, no. 19, pp. 3959–3969, 2007.

[111] V. D. Knyazev and K. V. Popov, "Kinetics of the self reaction of cyclopentadienyl radicals," *J. Phys. Chem. A*, vol. 119, no. 28, pp. 7418–7429, 2015.

[112] C. Cavallotti and D. Polino, "On the kinetics of the C_5H_5+C_5H_5 reaction," *Proc. Combust. Inst.*, vol. 34, no. 1, pp. 557–564, 2013.

[113] A. M. Mebel and V. V. Kislov, "Can the $C_5H_5 + C_5H_5 \rightarrow C_{10}H_{10} \rightarrow C_{10}H_9 + H$ / $C_{10}H_8 + H_2$ reaction produce naphthalene? an ab initio/RRKM study," *J. Phys. Chem. A*, vol. 113, no. 36, pp. 9825–9833, 2009.

[114] J. Filley and J. T. McKinnon, "Dimerization of cyclopentadienyl radical to produce naphthalene," *Combust. Flame*, vol. 124, no. 4, pp. 721–723, 2001.

[115] C. F. Melius, M. E. Colvin, N. M. Marinov, W. J. Pit, and S. M. Senkan, "Reaction mechanisms in aromatic hydrocarbon formation involving the C_5H_5 cyclopentadienyl moiety," *Symp. (Int.) Combust.*, vol. 26, no. 1, pp. 685–692, 1996.

[116] K. Roy, M. Braun-Unkhoff, P. Frank, and T. Just, "Kinetics of the cyclopentadiene decay and the recombination of cyclopentadienyl radicals with H-atoms: Enthalpy of formation of the cyclopentadienyl radical," *Int. J. Chem. Kinet.*, vol. 33, no. 12, pp. 821–833, 2001.

[117] L. B. Harding, S. J. Klippenstein, and Y. Georgievskii, "On the combination reactions of hydrogen atoms with resonance-stabilized hydrocarbon radicals," *J. Phys. Chem. A*, vol. 111, no. 19, pp. 3789–3801, 2007.

[118] X. Zhong and J. W. Bozzelli, "Thermochemical and kinetic analysis of the H, OH, HO_2, O, and O_2 association reactions with cyclopentadienyl radical," *J. Phys. Chem. A*, vol. 102, no. 20, pp. 3537–3555, 1998.

[119] J. H. Kiefer, R. S. Tranter, H. Wang, and A. F. Wagner, "Thermodynamic functions for the cyclopentadienyl radical: The effect of Jahn–Teller distortion," *Int. J. Chem. Kinet.*, vol. 33, no. 12, pp. 834–845, 2001.

[120] G. R. Liebling and H. M. McConnell, "Study of molecular orbital degeneracy in C_5H_5," *J. Chem. Phys.*, vol. 42, no. 11, pp. 3931–3934, 1965.

[121] M. Kira, M. Watanabe, and H. Sakurai, "Chemistry of organosilicon compounds. 100. substituent effects on the electron spin resonance spectra of cyclopentadienyl radicals. removal of degeneracy by organosilyl groups," *J. Am. Chem. Soc.*, vol. 99, no. 24, pp. 7780–7785, 1977.

[122] E. Hedaya, "Techniques of flash vacuum pyrolysis. cyclopentadienyl radical and its dimer," *Accts. Chem. Res.*, vol. 2, no. 12, pp. 367–373, 1969.

[123] M. Heaven, L. Dimauro, and T. A. Miller, "Laser-induced fluorescence spectra of free-jet cooled organic free radicals. vinoxy, cyclopentadienyl, and benzyl," *Chem. Phys. Lett.*, vol. 95, no. 4, pp. 347–351, 1983.

[124] L. Yu, S. C. Foster, J. M. Williamson, M. C. Heaven, and T. A. Miller, "Rotationally resolved electronic spectrum of jet-cooled cyclopentadienyl radical," *J. Phys. Chem.*, vol. 92, no. 15, pp. 4263–4266, 1988.

[125] L. Yu, J. M. Williamson, and T. A. Miller, "Rotationally resolved electronic spectrum of jet-cooled deuterated cyclopentadienyl radical," *Chem. Phys. Lett.*, vol. 162, no. 6, pp. 431–436, 1989.

[126] B. E. Applegate, T. A. Miller, and T. A. Barckholtz, "The Jahn–Teller and related effects in the cyclopentadienyl radical. I. The ab initio calculation of spectroscopically observable parameters," *J. Chem. Phys.*, vol. 114, no. 11, pp. 4855–4868, 2001.

[127] B. E. Applegate, A. J. Bezant, and T. A. Miller, "The Jahn–Teller and related effects in the cyclopentadienyl radical. II. Vibrational analysis of the $\tilde{A}^2A_2'' - \tilde{X}^2E_1''$ electronic transition," *J. Chem. Phys.*, vol. 114, no. 11, pp. 4869–4882, 2001.

[128] H. Ihee, J. S. Feenstra, J. Cao, and A. H. Zewail, "Ultrafast electron diffraction of transient cyclopentadienyl radical: A dynamic pseudorotary structure," *Chem. Phys. Lett.*, vol. 353, no. 5, pp. 325–334, 2002.

[129] T. Ichino, S. W. Wren, K. M. Vogelhuber, A. J. Gianola, W. C. Lineberger, and J. F. Stanton, "The vibronic level structure of the cyclopentadienyl radical," *J. Chem. Phys.*, vol. 129, no. 8, p. 084310, 2008.

[130] V. A. Korolev and O. M. Nefedov, "Direct IR spectroscopic study of the cyclopentadienyl radical," *Russ. Chem. Bull.*, vol. 42, no. 8, pp. 1436–1437, 1993.

[131] D. Leicht, M. Kaufmann, G. Schwaab, and M. Havenith, "Infrared spectroscopy of the helium solvated cyclopentadienyl radical in the CH stretch region," *J. Chem. Phys.*, vol. 145, no. 7, p. 074304, 2016.

[132] A. Burcat and M. Dvinyaninov, "Detailed kinetics of cyclopentadiene decomposition studied in a shock tube," *Int. J. Chem. Kinet.*, vol. 29, no. 7, pp. 505–514, 1997.

[133] R. D. Kern, Q. Zhang, J. Yao, B. S. Jursic, R. S. Tranter, M. A. Greybill, and J. H. Kiefer, "Pyrolysis of cyclopentadiene: Rates for initial C–H bond fission and the decomposition of c-C_5H_5," *Symp. (Int.) Combust.*, vol. 27, no. 1, pp. 143–150, 1998.

[134] K. Roy, C. Horn, P. Frank, V. G. Slutsky, and T. Just, "High-temperature investigations on the pyrolysis of cyclopentadiene," *Symp. (Int.) Combust.*, vol. 27, no. 1, pp. 329–336, 1998.

[135] V. D. Knyazev and I. R. Slagle, "Kinetics of the reaction between propargyl radical and acetylene," *J. Phys. Chem. A*, vol. 106, no. 23, pp. 5613–5617, 2002.

[136] F. Stahl, P. v. R. Schleyer, H. F. Schaefer Iii, and R. I. Kaiser, "Reactions of ethynyl radicals as a source of C4 and C5 hydrocarbons in Titan's atmosphere," *Planet. Space Sci.*, vol. 50, no. 7, pp. 685–692, 2002.

[137] J. D. Savee, T. M. Selby, O. Welz, C. A. Taatjes, and D. L. Osborn, "Time- and isomer-resolved measurements of sequential addition of acetylene to the propargyl radical," *J. Phys. Chem. Lett.*, vol. 6, no. 20, pp. 4153–4158, 2015.

[138] L. V. Moskaleva and M. C. Lin, "Unimolecular isomerization/decomposition of cyclopentadienyl and related bimolecular reverse process: ab initio MO/statistical theory study," *J. Comput. Chem.*, vol. 21, no. 6, pp. 415–425, 2000.

[139] A. Jamal and A. M. Mebel, "An ab initio/RRKM study of the reaction mechanism and product branching ratios of the reactions of ethynyl radical with allene and methylacetylene," *Phys. Chem. Chem. Phys.*, vol. 12, no. 11, pp. 2606–2618, 2010.

[140] A. V. Friderichsen, E.-J. Shin, R. J. Evans, M. R. Nimlos, D. C. Dayton, and G. B. Ellison, "The pyrolysis of anisole ($C_6H_5OCH_3$) using a hyperthermal nozzle," *Fuel*, vol. 80, no. 12, pp. 1747–1755, 2001.

[141] A. M. Scheer, C. Mukarakate, D. J. Robichaud, G. B. Ellison, and M. R. Nimlos, "Radical chemistry in the thermal decomposition of anisole and deuterated anisoles: an investigation of aromatic growth," *J. Phys. Chem. A*, vol. 114, no. 34, pp. 9043–9056, 2010.

[142] A. G. Harrison, L. R. Honnen, H. J. Dauben, and F. P. Lossing, "Free radicals by mass spectrometry. XX. Ionization potentials of cyclopentadienyl and cycloheptatrienyl radicals," *J. Am. Chem. Soc.*, vol. 82, no. 21, pp. 5593–5598, 1960.

[143] X. Zhong and J. W. Bozzelli, "Analysis of anisole and phenoxy radical decomposition kinetics," *Chem. Phys. Processes Combust.*, pp. 125–128, 1993.

[144] P. Schissel, D. J. McAdoo, E. Hedaya, and D. W. McNeil, "Flash vacuum pyrolysis. III. formation and ionization of cyclopentadienyl, cyclopentadienyl nickel, and dihydrofulvalene (dicyclopentadienyl) derived from nickelocene," *J. Chem. Phys.*, vol. 49, no. 11, pp. 5061–5066, 1968.

[145] D. C. Astholz, J. Troe, and W. Wieters, "Unimolecular processes in vibrationally highly excited cycloheptatrienes. I. Thermal isomerization in shock waves," *J. Chem. Phys.*, vol. 70, no. 11, pp. 5107–5116, 1979.

[146] N. Hansen, S. J. Klippenstein, J. A. Miller, J. Wang, T. A. Cool, M. E. Law, P. R. Westmoreland, T. Kasper, and K. Kohse-Hinghaus, "Identification of C_5H_x isomers in fuel-rich flames by photoionization mass spectrometry and electronic structure calculations," *J. Phys. Chem. A*, vol. 110, no. 13, pp. 4376–4388, 2006.

[147] N. M. S. D. Center, S. Stein, and director, "Mass spectra," in *NIST Chemistry WebBook, NIST Standard Reference Database Number 69, Eds. P.J. Linstrom and W.G. Mallard*, ch. Mass Spectra, Gaithersburg MD, 20899: National Institute of Standards and Technology.

[148] J. C. Robinson, N. E. Sveum, S. J. Goncher, and D. M. Neumark, "Photofragment translational spectroscopy of allene, propyne, and propyne-d3 at 193 nm," *Mol. Phys.*, vol. 103, no. 13, pp. 1765–1783, 2005.

[149] I. A. Ramphal, M. Shapero, C. Haibach-Morris, and D. M. Neumark, "Photodissociation dynamics of fulvenallene and the fulvenallenyl radical at 248 and 193 nm," *Phys. Chem. Chem. Phys.*, vol. 19, pp. 29305–29314, 2017.

[150] M. Lucas, Y. Song, J. Zhang, C. Brazier, P. L. Houston, and J. M. Bowman, "Ultraviolet photodissociation dynamics of the 1-propenyl radical," *J. Phys. Chem. A*, vol. 120, no. 27, pp. 5248–5256, 2016.

[151] K. Pachner, M. Steglich, P. Hemberger, and I. Fischer, "Photodissociation dynamics of the ortho- and para-xylyl radicals," *J. Chem. Phys.*, vol. 147, no. 8, p. 084303, 2017.

[152] R. Fröchtenicht, "The photodissociation of toluene studied by forward photofragment translational spectroscopy," *J. Chem. Phys.*, vol. 102, no. 12, pp. 4850–4859, 1995.

[153] M. Shapero, N. C. Cole-Filipiak, C. Haibach-Morris, and D. M. Neumark, "Benzyl radical photodissociation dynamics at 248 nm," *J. Phys. Chem. A*, vol. 119, no. 50, pp. 12349–12356, 2015.

[154] N. C. Cole-Filipiak, M. Shapero, C. Haibach-Morris, and D. M. Neumark, "Production and photodissociation of the methyl perthiyl radical," *J. Phys, Chem. A*, vol. 120, no. 27, pp. 4818–4826, 2016.

Appendix A

Laboratory Software

This appendix presents two programs written for daily operation of the laboratory in National Instruments' LabView 2014. There are two pieces to every LabView code, the front panel and the block diagram; both are presented here. The front panel is the user interface and has controls and indicators for the user. The block diagram is the back end of the program and has the code for the program function. Executable files were built from the LabView code so that these programs could be run by themselves without running the LabView coding environment. Only the front panel is available when running the executable files.

A.1 Data Acquisition Software

This software can be found on the computer in D10 Latimer as DataAcq.lvproj and the main code is in DataAcq.vi. The front panel is shown in Figure A.1.1, and the block diagram is shown in pieces throughout this appendix section. The code has many functions all relating to the data acquisition function. It communicates with the Ortec MCS PCI card to set the number of MCS bins, the dwell time for each bin, the number of passes to complete and when to start, stop and clear the data from the MCS. It displays the raw data as it is collected in real time with the option for background subtraction. It saves the collected data with the option for saving the background subtracted TOF spectrum. Additionally, this program can calculate the beam velocity of the molecular beam.

A.1.1 User Interface

The user interface for this program is made up of the front panel shown in Figure A.1.1. All of the buttons and boxes are connected to action items on the block diagram. Beginning with the top line of buttons, on the left is an indicator light that is bright when data acquisition is underway. Next is the "START" button to initiate acquisition and then the "Stop" button to pause acquisition. The "Save Unsub" button saves the unsubtracted TOF

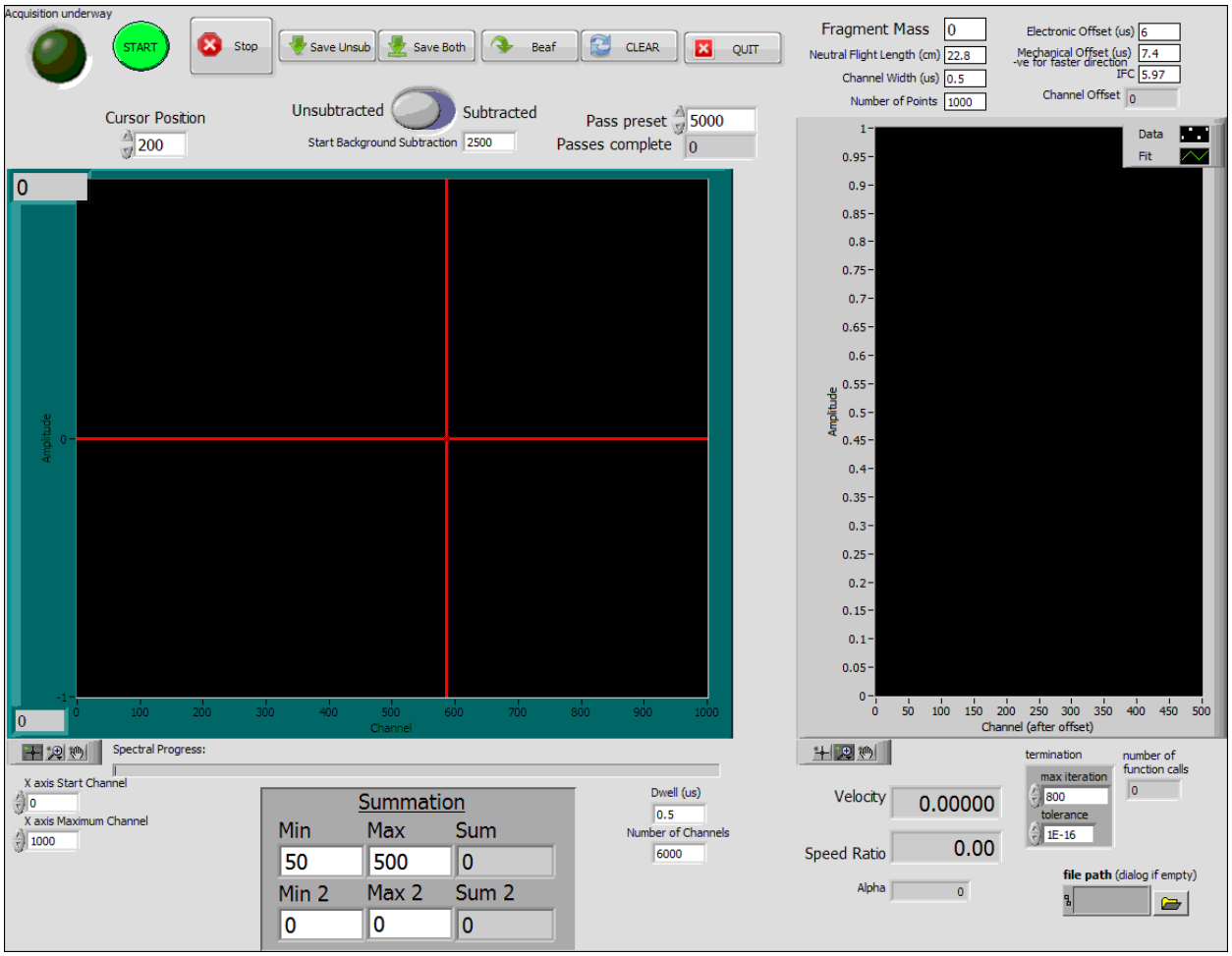

Figure A.1: Front panel for the data acquisition program

spectrum, whereas the "Save Both" button saves both the unsubtracted and the subtracted TOF spectra. The "Beaf" button will initiate the procedure for calculating the beam velocity. The "CLEAR" button erases the data stored on the MCS, clears the graph and sets the passes completed to 0. The "QUIT" button safely ends the entire program.

Below the first row of buttons are another set of controls. On the left is a numerical control for the position of the cursor along the x-axis. In the middle above the graph is the background subtraction controls. There is a switch that controls whether the unsubtracted or subtracted data is shown in the graph and underneath the switch is the channel number where background subtraction begins. At the right edge of the graph is the control box for the pass preset (i.e., the requested number of passes to complete) and below that is the indicator for how many passes have been completed.

On the graph itself, there are two boxes at the top and bottom of the y-axis that indicate the maximum and minimum values for the data shown in the graph. At the bottom left corner of the graph are 3 icons that allow you to manipulate the graph. When the first icon is selected, the red cursor can be moved with the mouse. The second icon allows the user to change the viewing field on the graph using the mouse. The third icon allows the mouse to grab and drag the data to change the visible range. The range on the x-axis can also be set with the 2 controls on the bottom left of the panel.

Directly below the graph is a progress bar that indicates the level of completion of the spectrum. Below that are the summation controls that integrate the signal between a given minimum and maximum channel number. On the right side are controls for the dwell time and the number of channels.

The right side of the front panel is for the beam fitting subroutine. The top has controls for inputing the fragment mass, the neutral flight length, the channel dwell time (width) of the spectrum to be fit, number of points to fit, electronic offset, mechanical offset, and ion flight constant. The graph displays the TOF for fitting as well as the fit function. Below the fitting graph are the indicators for the calculated velocity, speed ratio, alpha (another parameter for the spread in velocity) and the number of fitting function calls or iterations. There are also controls for setting the termination of the fitting routine with the number of max iterations and the fit tolerance. The file of the TOF spectrum to fit can also be specified in the box at the bottom right of the panel. Normally, this file path is left empty and in that case, a dialog box will pop up asking for the file.

A.1.2 Block Diagram Code

A state machine structure was used to construct this program. There are 5 states: “Initialize”, “Idle”, “Data Acquisition”, “Save Unsub Data”, “Sub Sub”, and “Beaf”. The program is initialized in the “Initialize” state, which then sets the state to “Idle”. Within the “Idle” state, the program waits for some user input and then proceeds according to the input.

There is a small amount of code that is outside of the state machine that is only run at the onset of the program. Figure A.2 shows the code outside of the state machine, which opens the connection to the MCS and passes that connection into the state machine structure. The graph on the front panel is also initialized outside of the state machine so that it can be changed through commands in the block diagram.

A.1.2.1 Initialize

Figure A.2 shows the “Initialize” state. Inside the “Initialize” state, the MCS parameters are set through property nodes. First the MCS connection is opened, then it is set to use a discriminator with a +1.4 V threshold. The impedance is set to 1 kΩ. Each pass is set

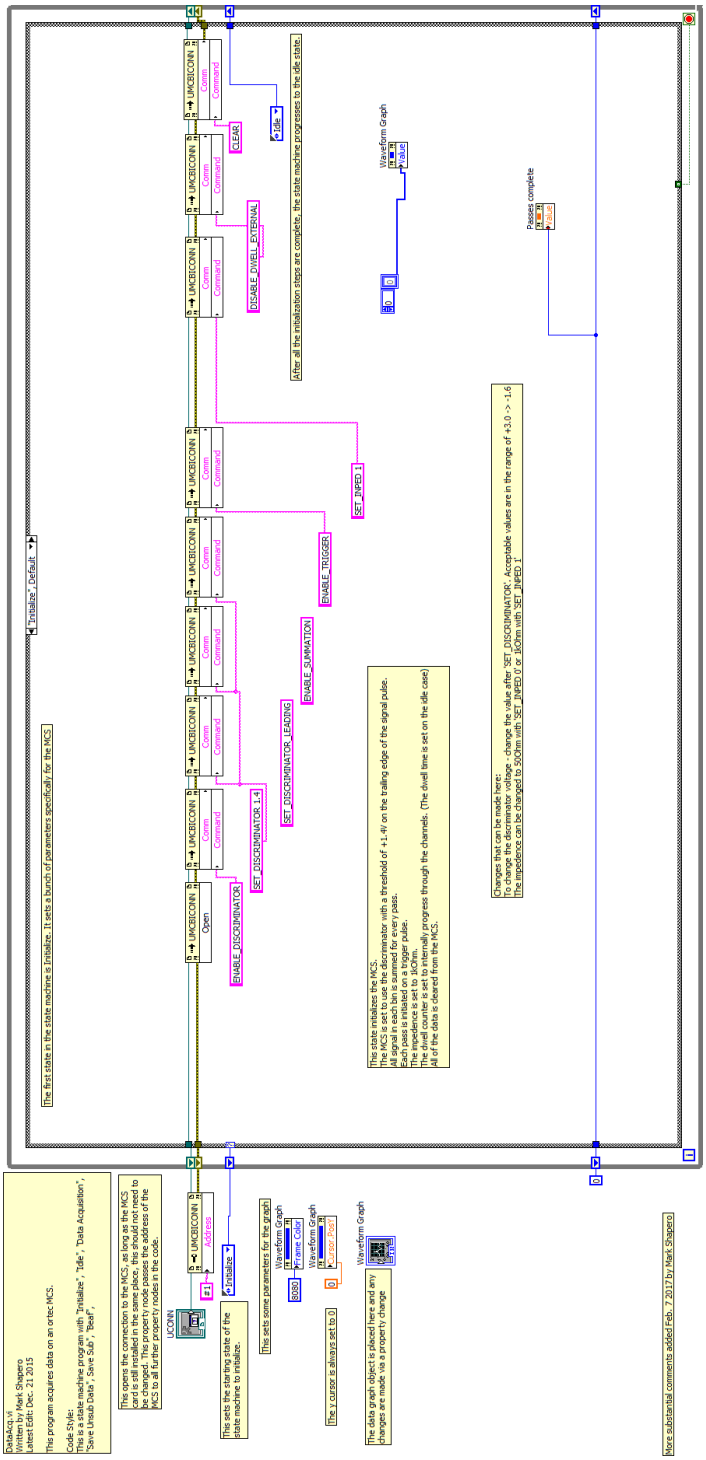

Figure A.2: This frame shows the code that is outside of the state machine as well as the "Initialize" state.

to start with an external trigger pulse that comes from a Stanford delay generator and to progress through the channels via the internal MCS clock. Finally, the MCS is cleared and the graph on the front panel is also cleared. The "Initialize" state ends by sending the state to the "Idle" state.

A.1.2.2 Idle

The "Idle" state structure is shown in Figure A.3. It begins with enabling the controls to set the channel dwell time, the pass preset value, the number of channels value, the "CLEAR" button and the "QUIT" button. Then the "Idle" state waits for an event to occur. The event structure has 12 different events that trigger actions. The events and their respective diagram figure numbers are show in Table A.1.

Table A.1: Events that trigger a response in the "Idle" state

Event	Figure
START button value change	A.3
Beaf button value change	A.5
Dwell time value change	A.8
Save Unsub button value change	A.6
Save Both button value change	A.7
Unsubtracted – Subtracted switch value change	A.10
Summation Min or Max value change	A.11
Cursor move via mouse on graph	A.12
Cursor Position value change	A.13
Number of Channels value change	A.9
Quit button value change	A.15
Clear button value change	A.14

The event structure of Figure A.3 is triggered when the "START" button is pressed. First, the pass preset is compared to the passes completed. If they are the same, then the True case is activated in Figure A.4, where there is a prompt saying "The pass preset and completed passes are equal". The True case returns the state to the "Idle" state.

If the pass preset is greater than the completed passes then the False case in Figure A.3 is activated. The False case sets up the program to start data acquisition. It reads the dwell time and number of channels and passes that to the MCS. It compares the pass preset and the completed passes and sends the difference as the pass preset to the MCS. Then the controls for the channel dwell time, the pass preset value, the number of channels value, the "CLEAR" button and the "QUIT" button are disabled and grayed out. Finally, the Acquisition underway light on the front panel is turned on and the state is changed to "Data Acquisition", shown in Figure A.16.

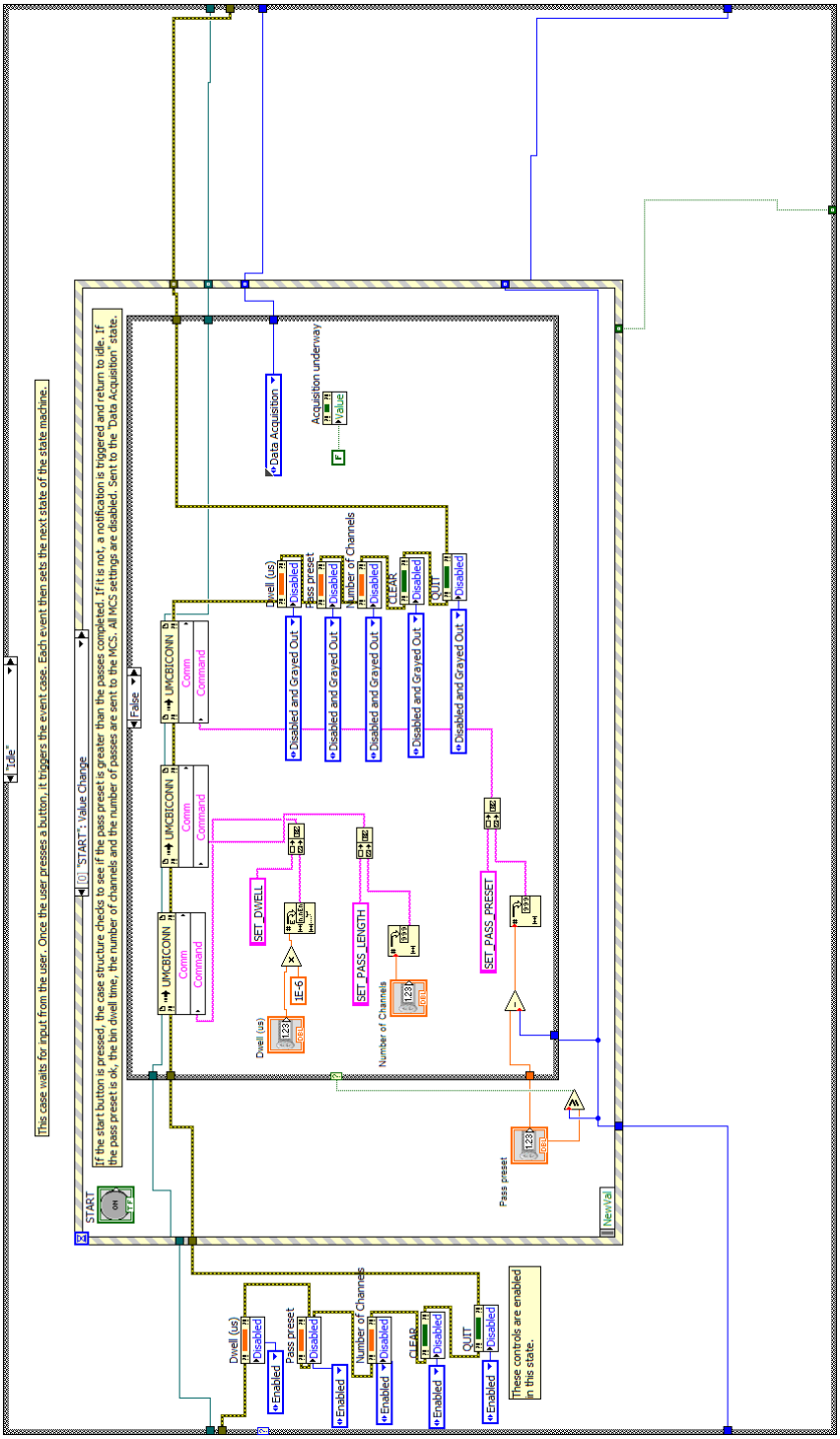

Figure A.3: This frame shows the "Idle" state with the event structure for when the "START" button on the front panel is pressed.

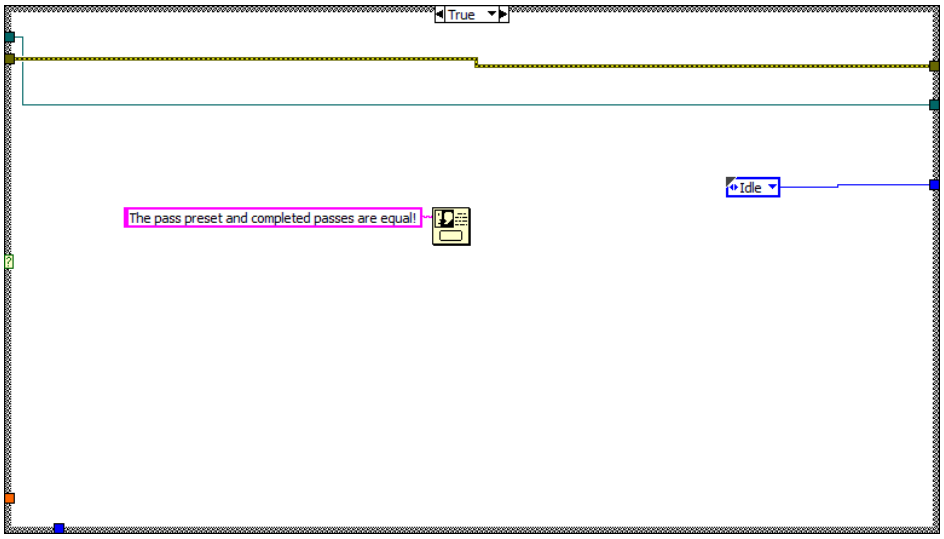

Figure A.4: This frame shows the case structure for when the pass preset value is equal to the passes complete value inside the event structure for when the "START" button is pressed.

Figures A.5, A.6 and A.7 show event structures that simply change the state of the program to the "Beaf" state, "Save Unsub Data" state and "Save Sub" state respectively.

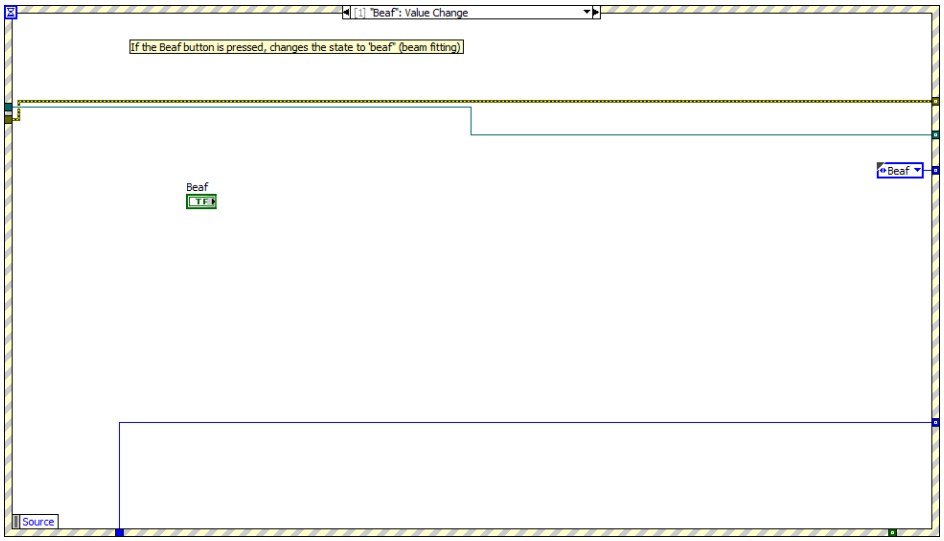

Figure A.5: This frame shows the event structure for when the "Beaf" button is pressed.

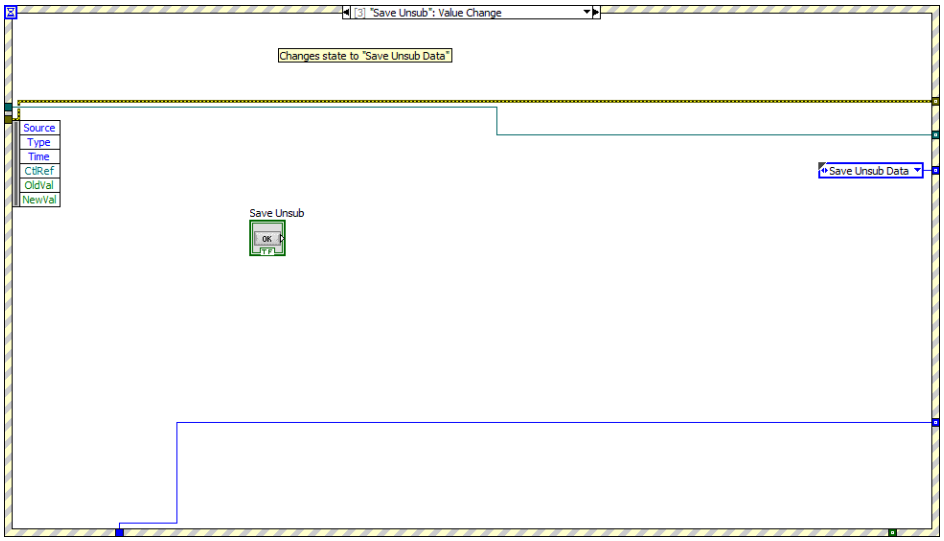

Figure A.6: This frame shows the event structure for when the "Save Unsub" button is pressed.

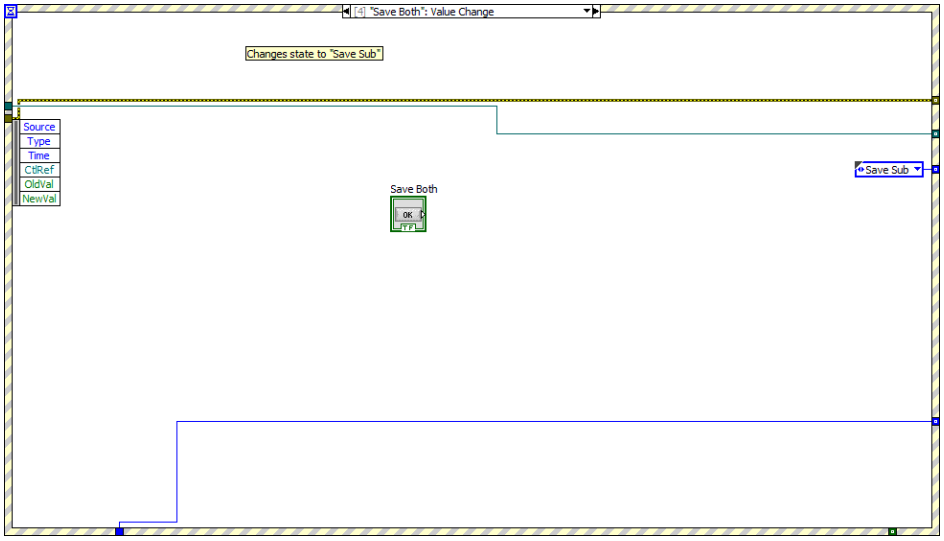

Figure A.7: This frame shows the event structure for when the "Save Both" button is pressed.

Figures A.8 and A.9 show event structures where the dwell time and number of channels values are changed, respectively. Once the change is made, a dialogue box pops up to say "MCS data will be cleared". If the user responds ok, the True case is activated and the MCS, the graph and the passes completed are cleared. If the user doesn't respond ok, then the False case is activated, which is just a blank case that allows the user to go back and save any wanted data. After these events occur, the state is returned to the "Idle" state.

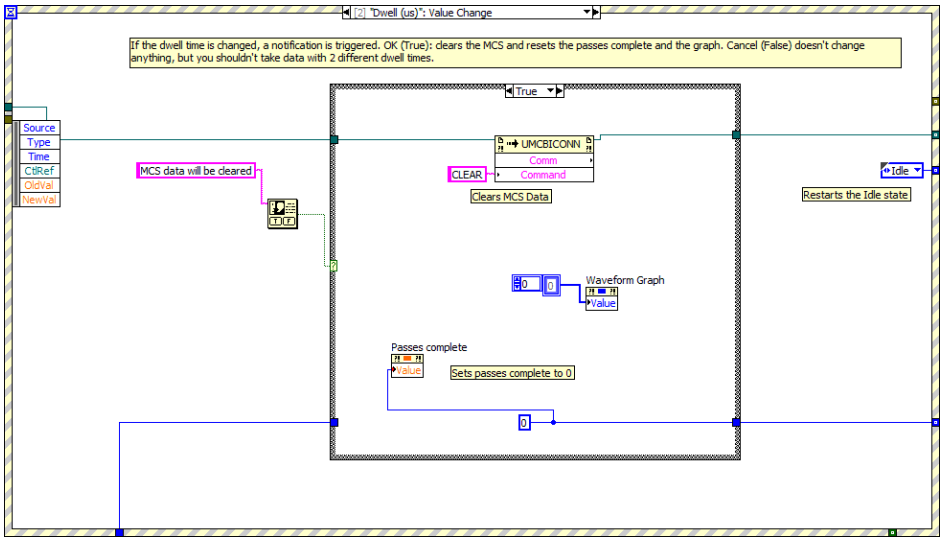

Figure A.8: This frame shows the event structure for when the dwell time for each channel is changed. The false case is blank.

The code in Figures A.10 and A.11 are the same but they are initiated by different events. The event that for Figure A.10 is when the Unsubtracted – Subtracted switch is pressed and the event for Figure A.11 is when any of the max or min values are changed in the summation section on the front panel. The goal of this structure is to change the summation data and the graph displayed on the front panel. First, data is collected from the MCS and converted into usable data arrays. Then the program checks to see if the user wants subtracted or unsubtracted data. Figures A.10 and A.11 show the case for subtracted data. Within the true case for subtracted data, the data array is processed so that it contains the subtracted data and then the integration of the signal is done and updated on the front panel. Finally the data is sent to the front panel graph and the state is returned to the "Idle" state.

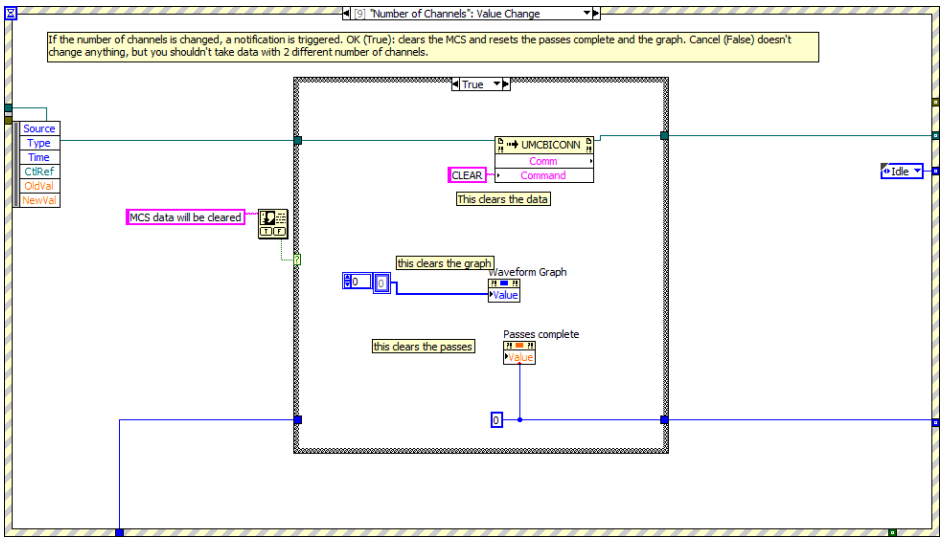

Figure A.9: This frame shows the event structure for when the number of channels is changed. The false case is blank.

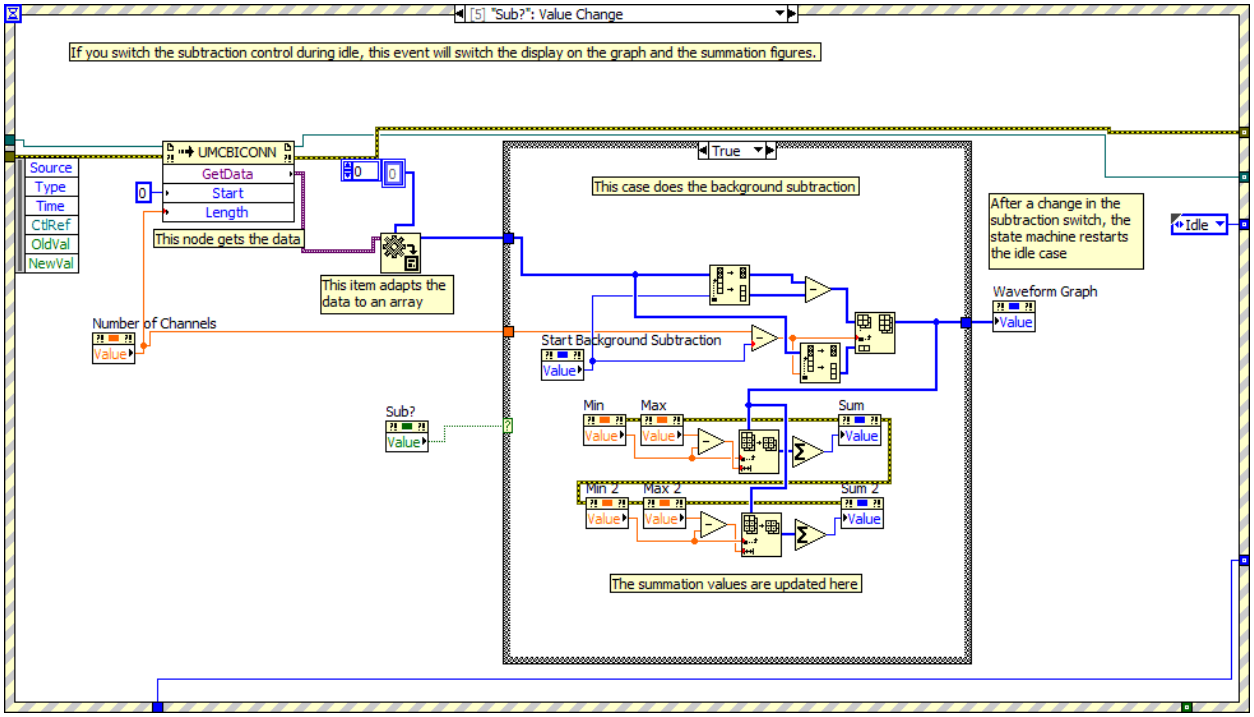

Figure A.10: This frame shows the event structure for when the Unsubtracted – Subtracted switch is pressed.

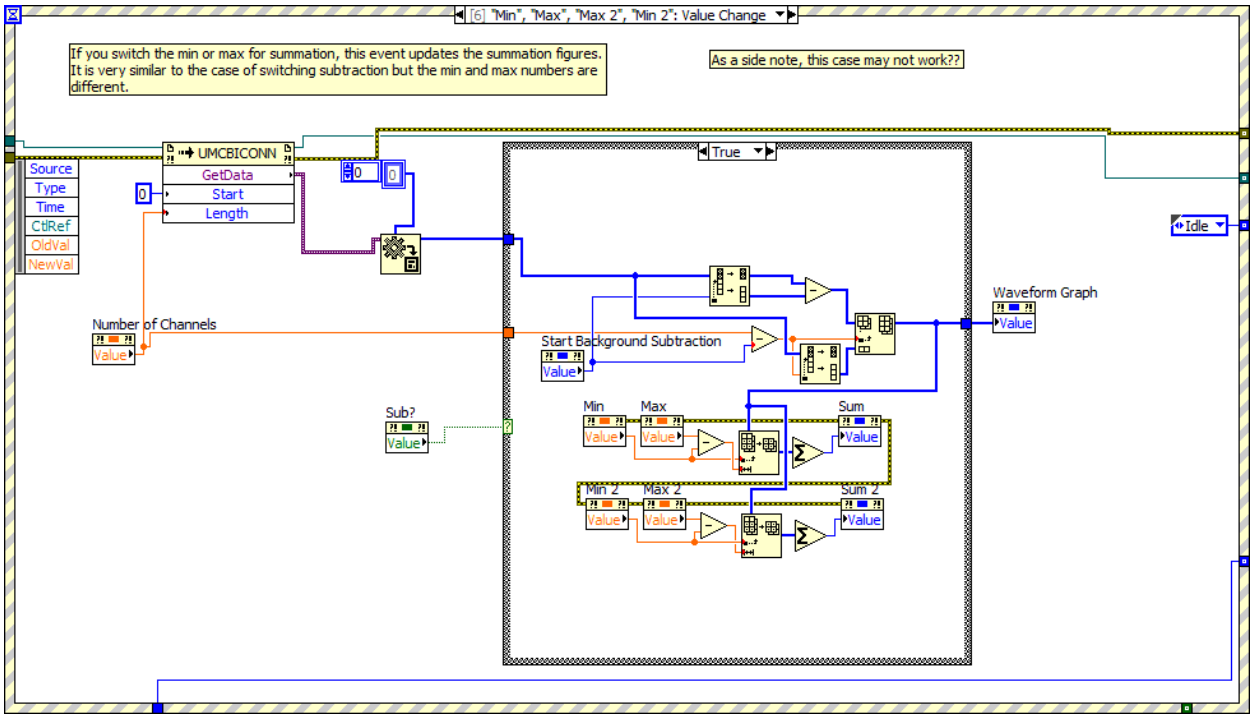

Figure A.11: This frame shows the event structure for when the Max or Min in the Summation controls are changed.

Figures A.12 and A.13 both deal with the cursor from the graph on the front panel. The bulk of the code in each diagram is to render the graph from the MCS data. The pertinent code for each event is at the bottom of the structure. Figure A.12 shows the event structure for when the cursor is moved with the mouse. In this case, the cursor position value on the front panel is updated to the where the cursor was moved with the mouse. In Figure A.13, the cursor on the graph is moved by changing the numerical value of the cursor position on the front panel. Both event cases return the state to the "Idle" state.

The last two events in the "Idle" state are clearing the MCS data in Figure A.14 and quitting the data acquisition program in Figure A.15. To clear the MCS data, a clear command is sent to the MCS. In addition, the graph is cleared and the passes completed is set to 0. After clearing, the state is returned to the "Idle" state. To quit the program, the connection to the MCS is closed and the program ends.

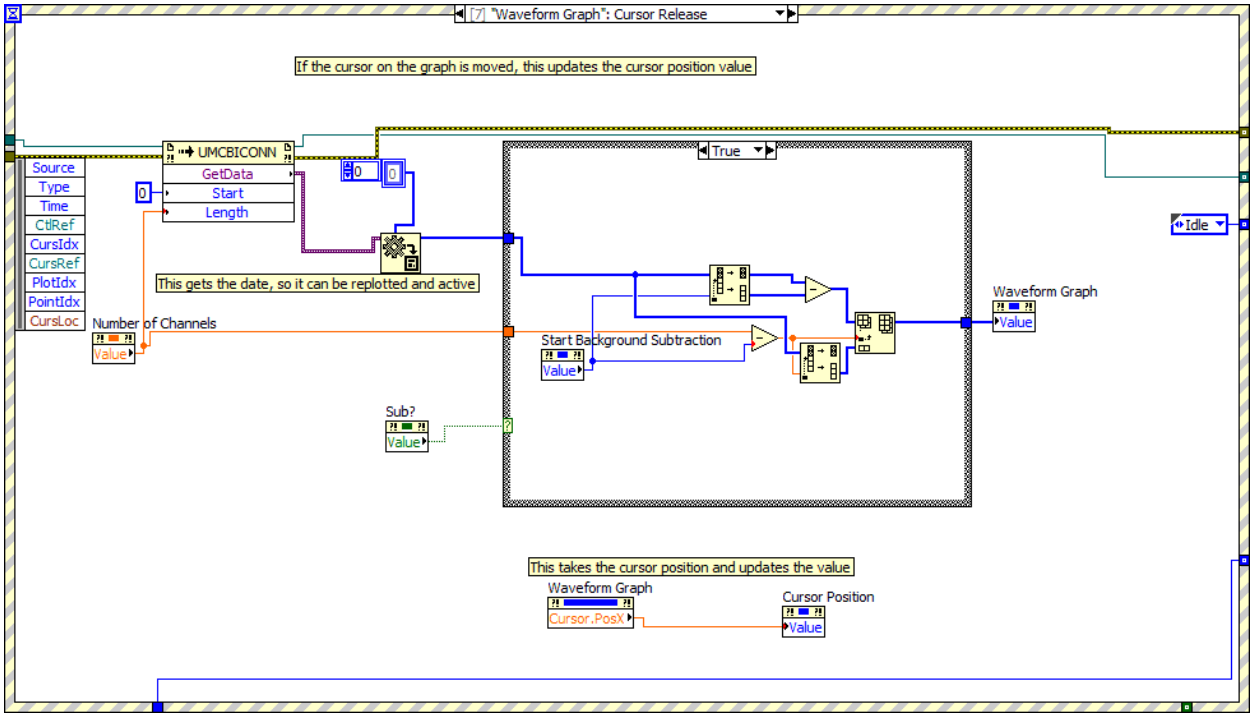

Figure A.12: This frame shows the event structure for when the cursor on the graph is moved with the mouse

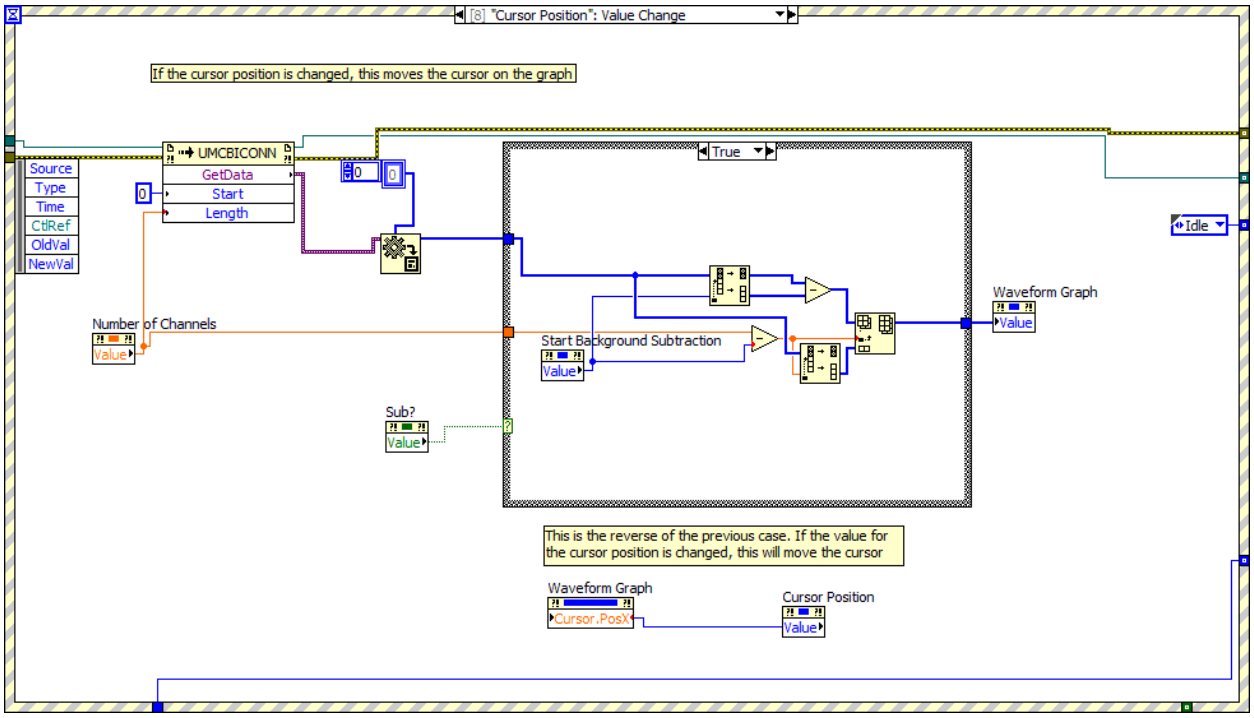

Figure A.13: This frame shows the event structure for when the numerical value of the cursor position is changed.

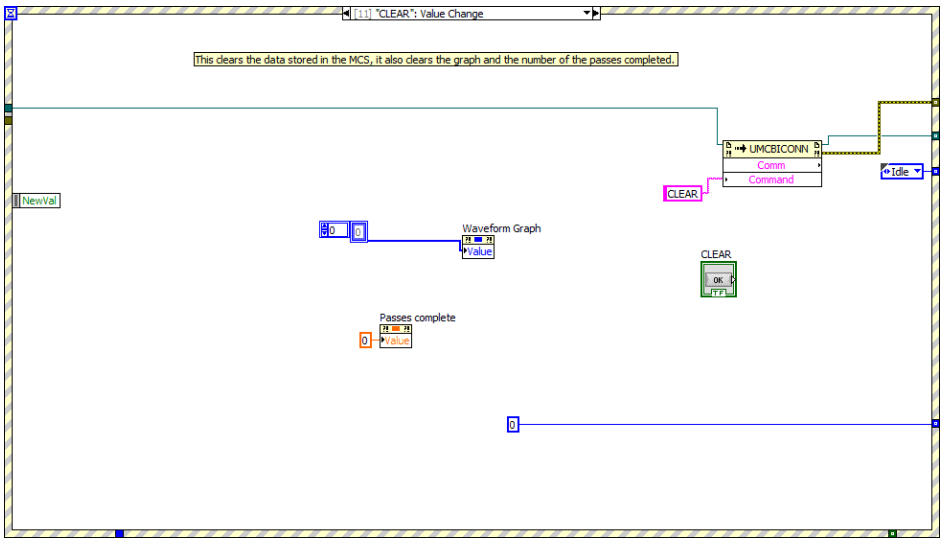

Figure A.14: This frame shows the event structure for when the "CLEAR" button is pressed.

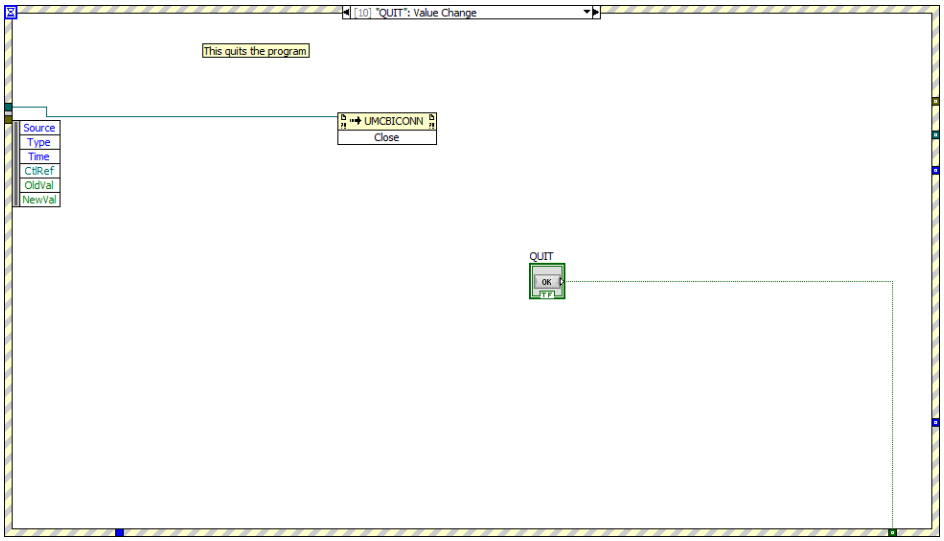

Figure A.15: This frame shows the event structure for when the "QUIT" button is pressed.

A.1.2.3 Data Acquisition

The heart of this program is in the "Data Acquisition" state shown in Figure A.16. First, the start command is sent to the MCS for it to start collecting data. Then a loop is entered, which is used to continuously update the front panel. The x-axis is monitored so that the maximum and minimum data amplitude shown on the front panel corresponds to the viewing window. The data on the graph is constantly being refreshed and Figure A.16 shows the case when the unsubtracted data is shown. Throughout the updates, the cursor position is monitored and adjusted according to user input either via the mouse or the numerical front panel control. The passes completed is monitored and compared to the pass preset. When the passes completed matches the pass preset, the loop is exited, a sound is played and the stop command is sent to the MCS. There is also the capability to press the "Stop" button, which also exits the loop and sends the stop command to the MCS. Once the data acquisition has been stopped, the state is sent back to "Idle".

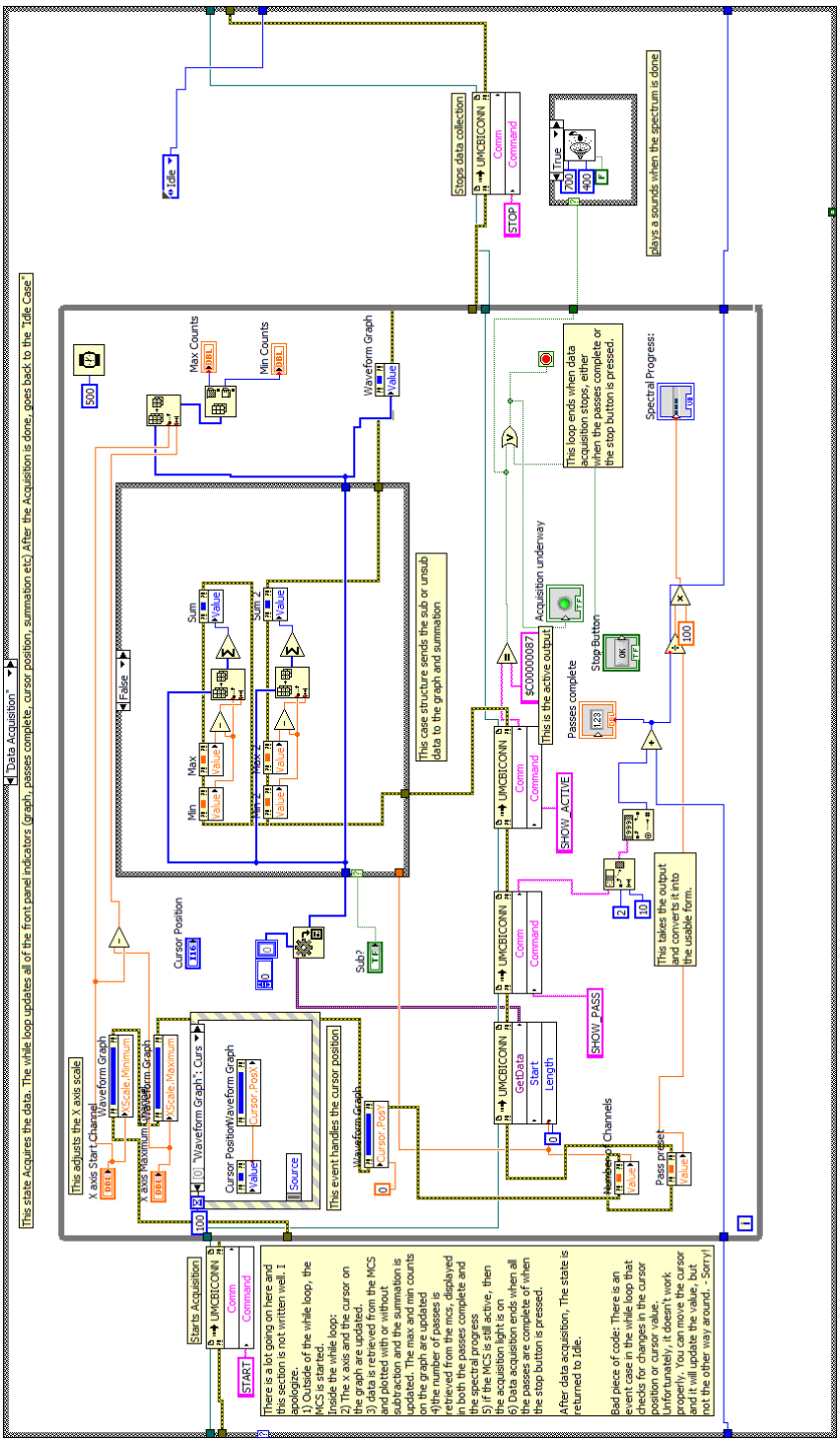

Figure A.16: This frame shows the data acquisition state.

A.1.2.4 Saving Data

Figures A.17 and A.18 show the routines for saving the data. They both begin with getting the data from the MCS, converting it into usable data and then saving it as a spreadsheet file. A dialog box pops up asking the user to input a file name. For saving both subtracted and unsubtracted data, first the unsubtracted data is saved and then the data is manipulated for background subtraction and saved again with an 's' added to the end of the unsubtracted file name. Both of these states return to the "Idle" state.

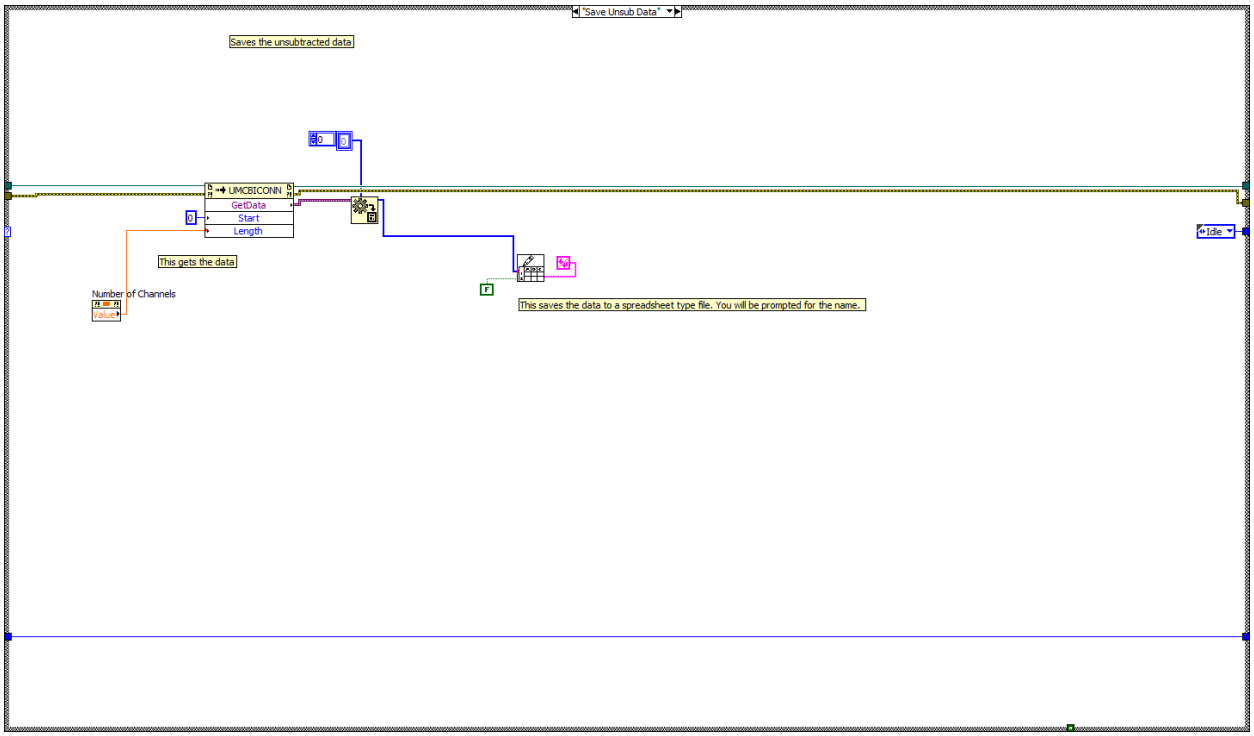

Figure A.17: This frame shows the "Save Unsub Data" state.

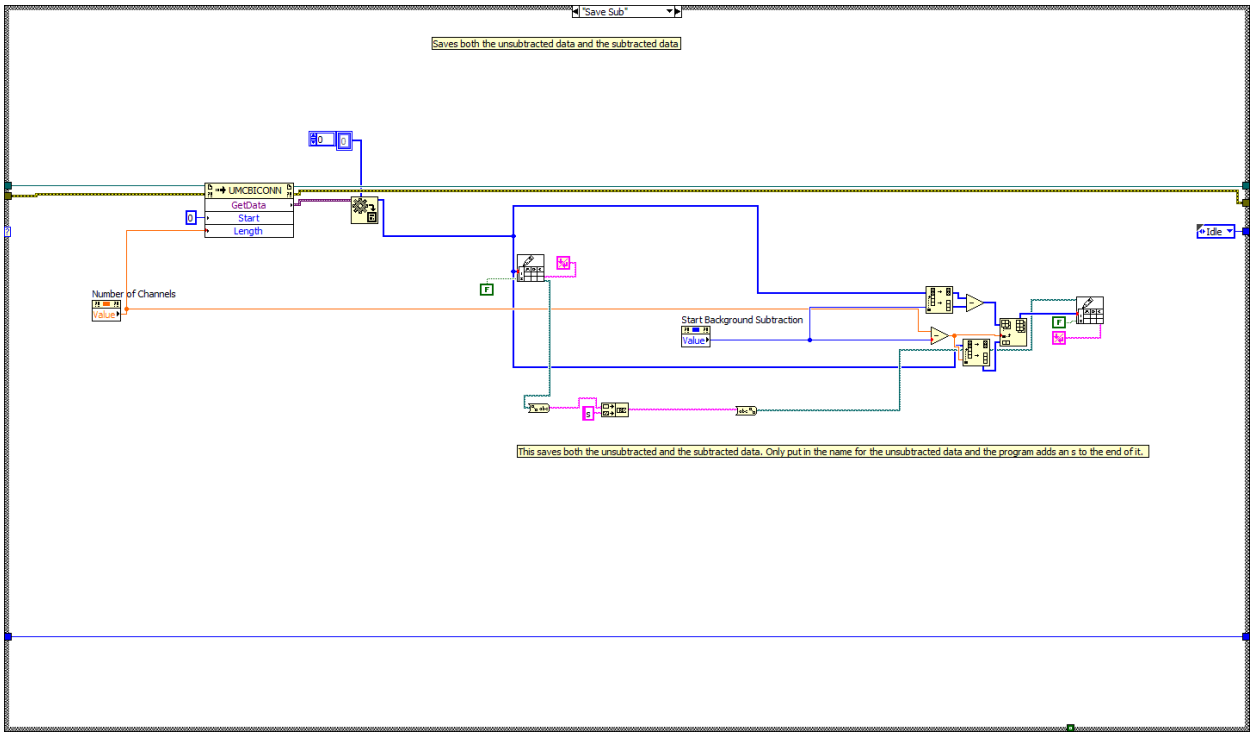

Figure A.18: This from shows the "Save Both" state.

A.1.2.5 Beam Fitting

The final state in the state machine is "Beaf" for the beam fitting routine to determine the beam velocity and the spread in beam velocities. It is shown in Figure A.19. Starting on the left side of the frame, the measured arrival time or channel is converted into the neutral flight time using Equation 2.3. If no fragment mass is input on the front panel then a dialogue box pops up warning the user. Next, the TOF spectrum to be fit is read into the program and the data is shifted so that the bins correspond to the corrected neutral flight time. Next the data is sent to a fitting routine built into LabView that uses the Levenberg-Marquardt algorithm. The initial guesses at the fitting parameters are determined by analyzing the input data. If a good fit is not reached, playing around with bolded numbers can help. The final input to the fitting routine is the beam fitting model, which is shown in Figure A.20 and is based on Equation 2.1. Out of the fitting routine, the parameters are manipulated to give the beam velocity and speed ratio and the fit function is shown on the front panel.

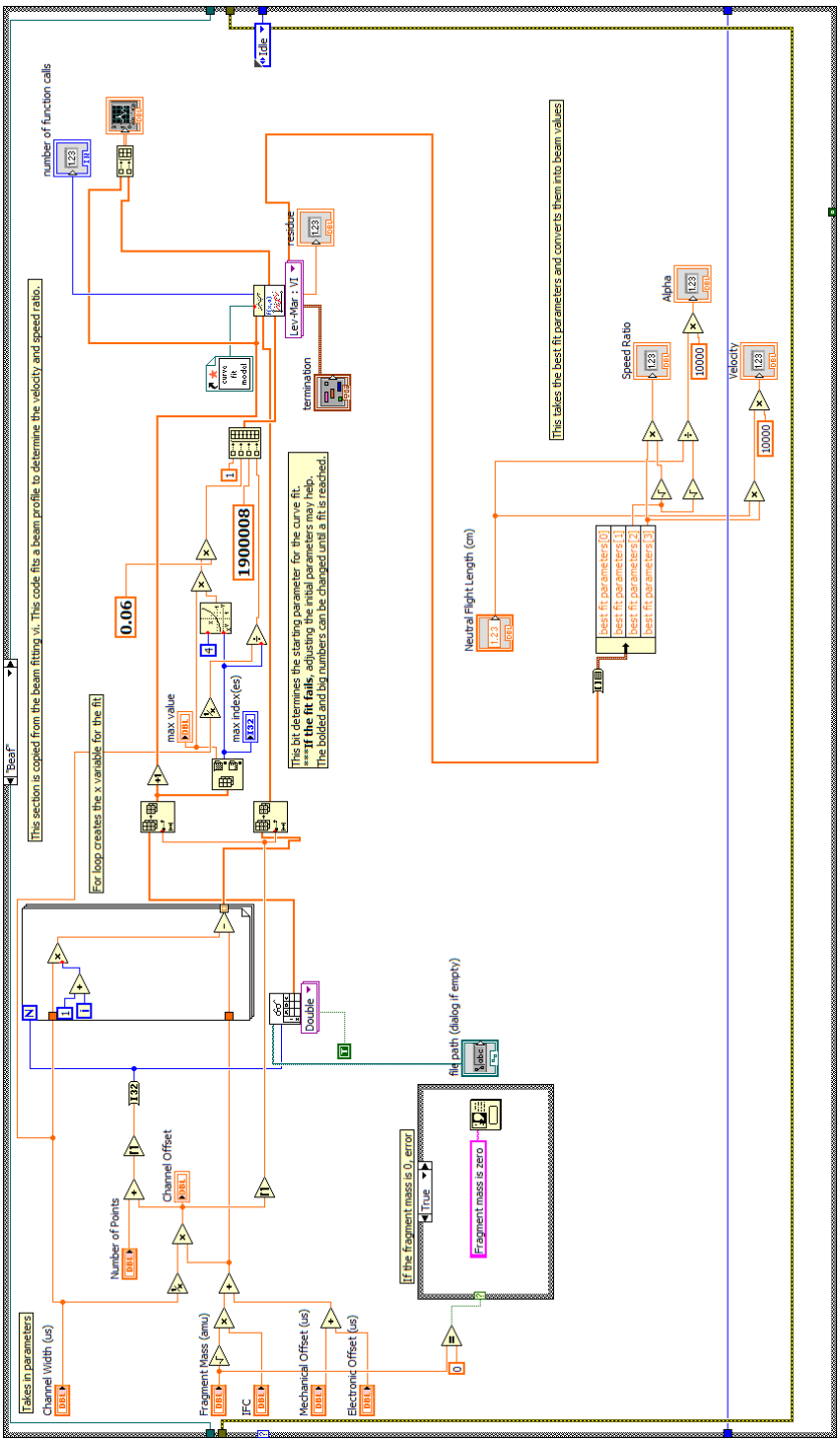

Figure A.19: This frame shows the "Beaf" state for beam fitting.

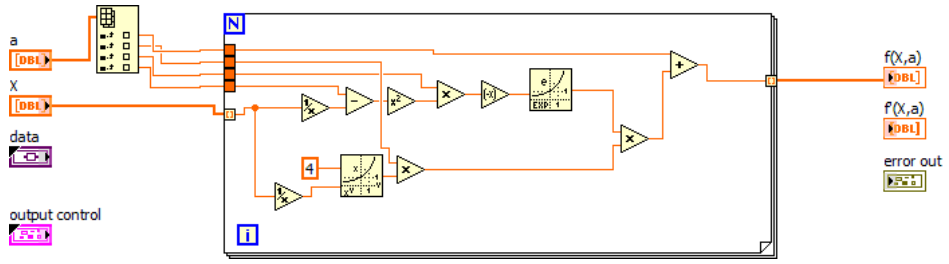

Figure A.20: This frame shows the model for the beam fitting routine.

A.2 Pressure Monitoring Software

The following code was developed to monitor the pressure in the apparatus and turn on the helium cyro-compressor at a certain time if the pressures were all low enough. It was later updated to include a routine that can print out the pressures to a file and a routine that adjusts the source chamber pressure by controlling a servo motor. The program can be found on the lab computer in D10 Latimer as "Pressure and Cold Head April 2014.lvproj" and the main code is pressure.vi.

A.2.1 Front Panel

The front panel contains indicators on the pressure in the apparatus as well as serval user controls. On the left in big red font are the pressures from the source chamber and the main chamber ion gauges. To their right are the controls to input the upper bound limits for those pressures in order for the cold head to turn on. At the top right are the pressure

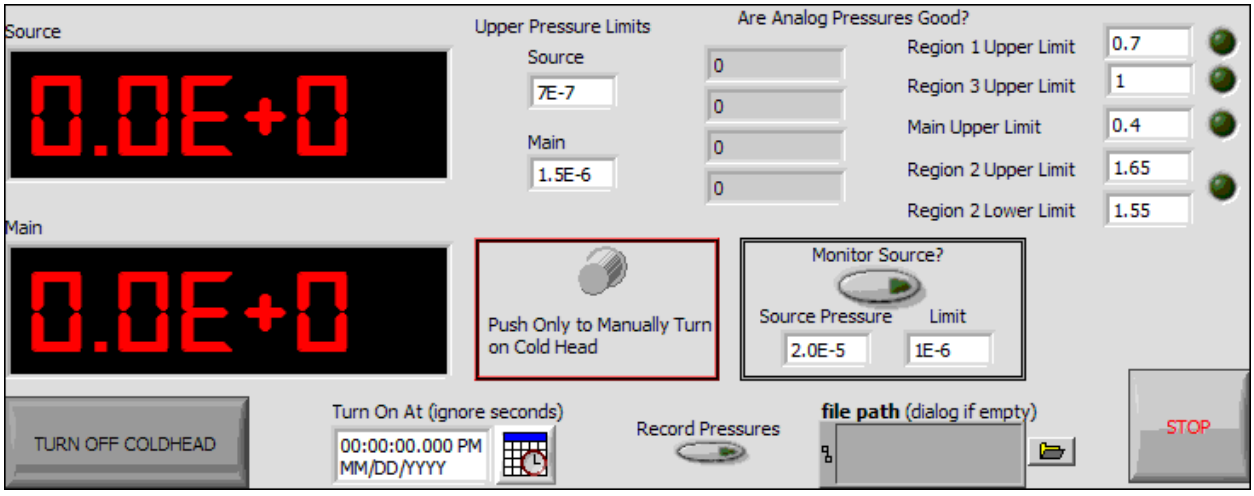

Figure A.21: The front panel of the pressure monitoring program

indicators and limits for the ion gauges of Regions 1, 2 and 3 in the detector as well as the convectron gauge on the main chamber. The readouts from these gauges are in volts and were not converted to pressure. If the voltage readouts from the pressure gauges are within the limits set, then the green lights on the far right turn on.

In the middle of the front panel is a button to manually turn on the cold head. Next to it is the pressure monitoring controls with a switch to turn source monitoring on and numerical controls to set the desired pressure and its the tolerance. Along the bottom is a button to turn off the cold head, a time control input to set when the cold head should turn on, a switch to record pressures and the file path for where to save the pressures. Finally there is a STOP button that quits the program.

A.2.2 Hardware

In order to be able to turn the cold head on with the computer and to adjust the pressure in the source chamber, new hardware solutions were installed in lab.

For the cold head to be turned on remotely, a voltage needs to be applied to one of the 25 pins on its remote connector. The correct voltage is supplied by a different pin. A relay was installed between the voltage supply and the pin to turn on the compressor. The relay takes 5 V from a National Instruments voltage I/O device and when that voltage is sent, the relay opens and turns on the cold head. The 5 V signal will be discussed below in the block diagram code. The same voltage I/O device reads in the voltage from the ion gauges of Regions 1, 2 and 3 in the detector as well as the convectron gauge on the main chamber

For the computer to adjust the pressure in the source chamber, gears were installed on the pulsed valve voltage controller and on a servo motor. The servo motor is controlled by an arduino uno that is connected to the LabView program. The arduino code is below.

A.2.3 Block Diagram Code

This code would be considered poor coding structure. It uses a while loop to inclose 5 parallel case structures. Outside the while loop, the connection to the source and main chamber ion gauge controllers is established through a visa serial connector. Inside the while loop the pressures are continuously read and the front panel is updated.

The five case structures, from top to bottom, in Figure A.22, monitor: 1) If the turn off cold head button has been pressed, 2) If the user wants the pressures recorded, 3) If the turn on cold head manually button is pressed, 4) If the set turn on time matches the actual time, and 5) If pressure monitoring is requested by the user.

The first case waits for the turn off cold head button to be pressed. When this button is pressed, the 5 V signal that is sent to the relay to turn on the cold head is removed and

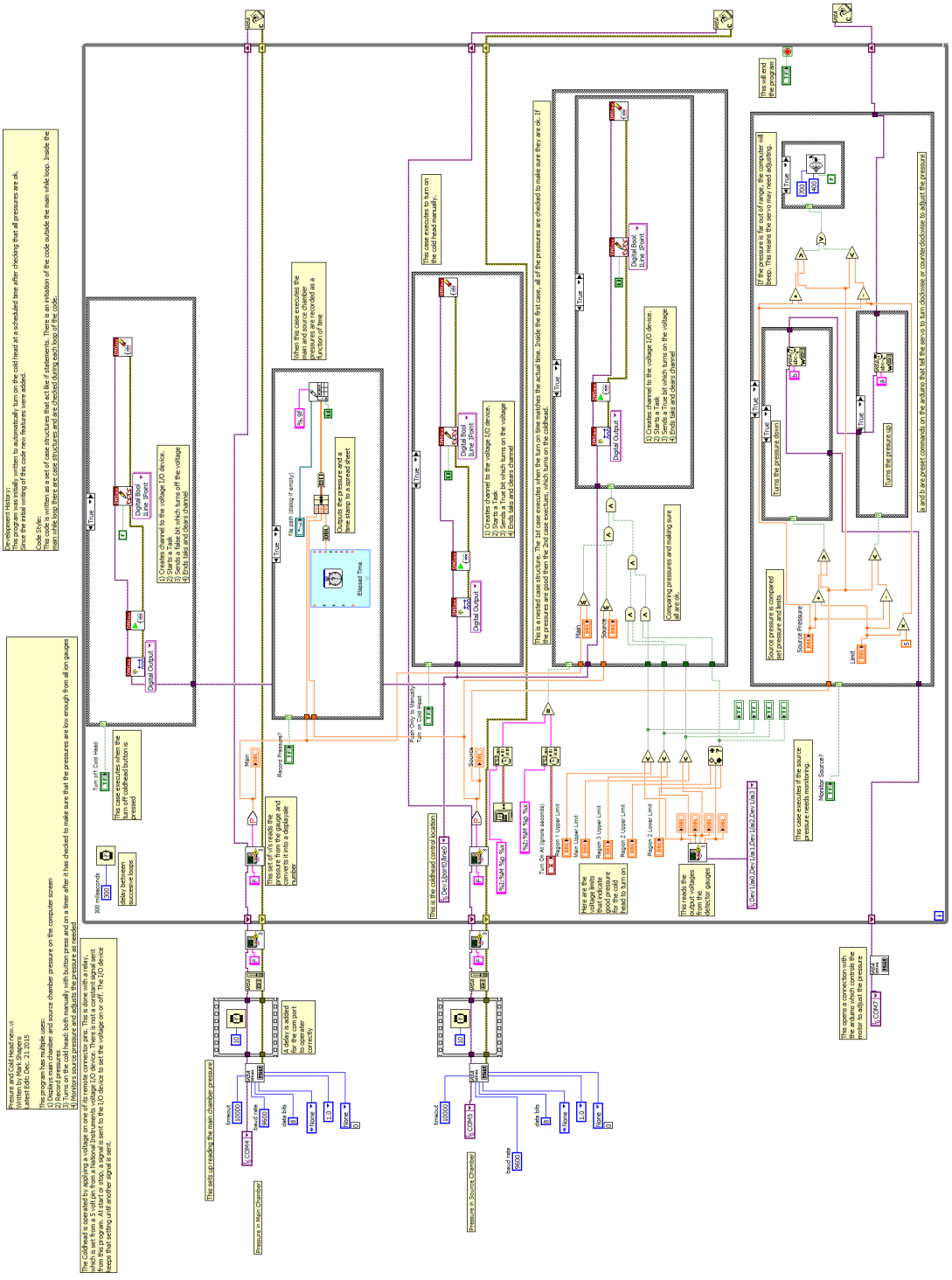

Figure A.22: The block diagram for the pressure monitoring code. All False cases are blank.

the cold head turns off.

The second case records the pressures from the main chamber and source chamber. The pressures are saved with the elapsed time to a spreadsheet with a desired file path.

The third case waits for the turn on cold head manually button to be pressed. In this case, the 5 V signal is sent to the relay to turn on the cold head.

The fourth case is the main part of this code. When the set turn on time matches the actual time, all of the pressures are compared with the limits set on the front panel. If all pressures are low enough, then the 5 V signal is sent to the turn on the cold head.

The fifth case is for pressure monitoring. It compares the desired pressure to the actual source pressure. If it is low by more than the limit, a command is sent to the arduino to turn the servo motor to increase the pressure and similarly if the pressure is too high by more than the limit, then the servo motor will decrease the pulsed valve voltage. In addition, if the pressure is 5 times the limit away from the desired pressure, the program beeps.

A.2.3.1 Internal LabView Code

The block diagram code includes three nodes that were designed for this program and their block diagrams are shown in Figures A.23, A.24, and A.25. These are small blocks of code that repeat in the main block diagram and therefore were converted into their own little sub-code.

A.2.4 Arduino Code

The following code, pressure.ino written in Arduino version 1.7.8, is programed into the Arduino to communicate with a continuous servo motor. The servo motor is idle when it is set to 90 and full speed in one direction at 0 and the other direction at 180. The program sets the servo motor to 88 for 100 ms when the arduino receives the decrease pressure command from LabView and to 92 for 100 ms to increase the pressure. The program is pressure.ino and

```
/*
Automated Pressure adjustment
Written by Mark Shapero 2015
*/

#include <Servo.h> // call the servo library

Servo servo; // create a servo object to control each servo
```

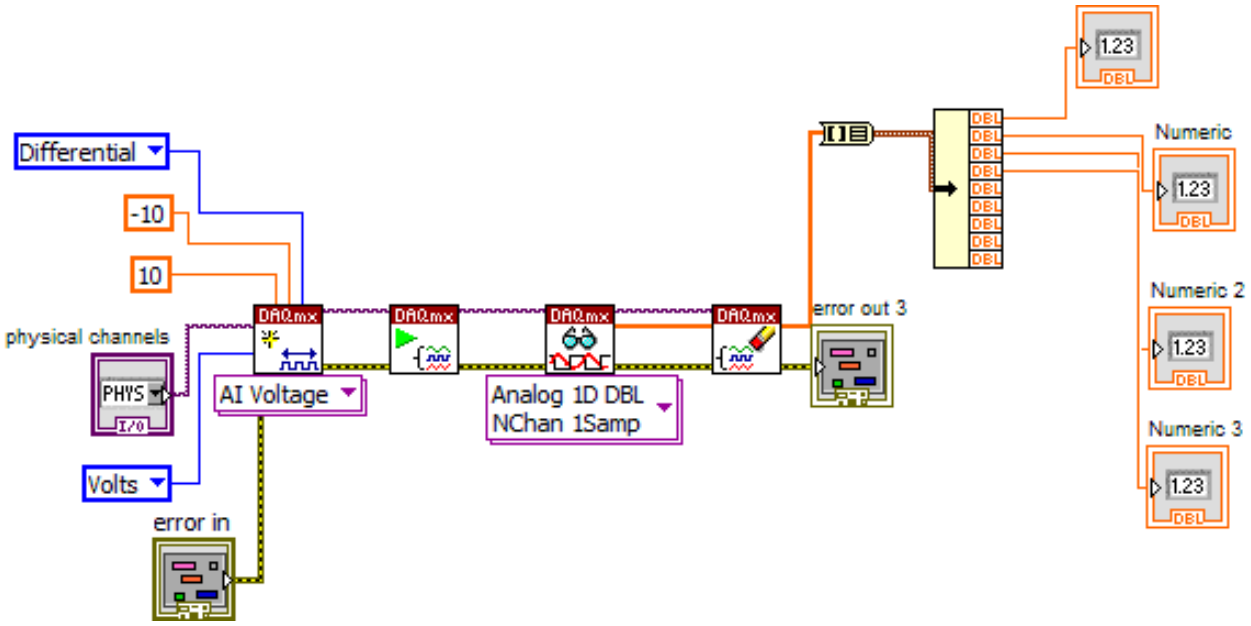

Figure A.23: Subroutine for reading analog voltages from detector ion gauges and main chamber convectron gauge.

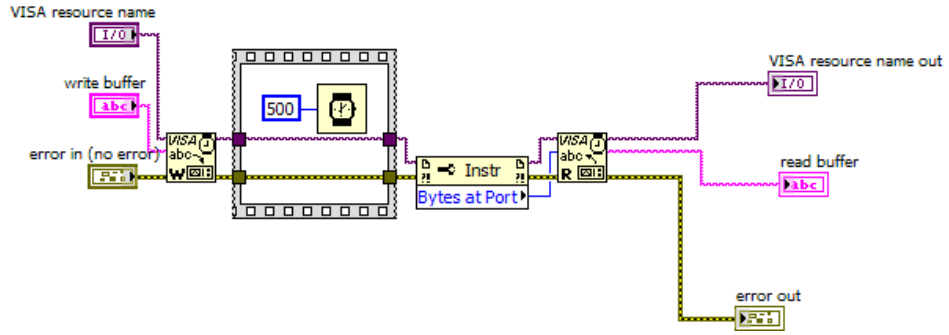

Figure A.24: Subroutine for requesting the TerraNova ion gauge controller send the pressure readout to the computer.

```
void setup()
{
  servo.attach(9); // attach servos on pins to servo object


  Serial.begin(9600); //connect to USB port
```

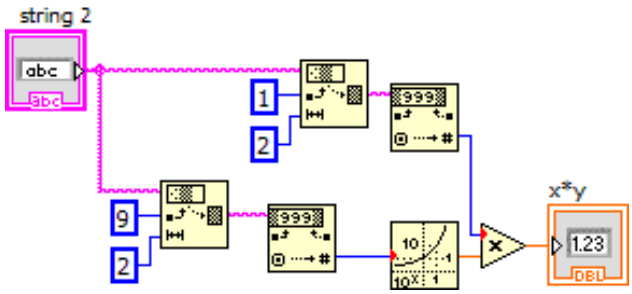

Figure A.25: Subroutine for converting output from TerraNova ion gauge controller into scientific notation for displaying on the front panel.

```
  // Initialize the servos to be stationary
  servo.write(90);
}

// Rotate the servo to adjust the pressure
void loop()
{
 if (Serial.available() > 0) // get the number of bytes available
    ↪ to read from the serial port
 {
   int inByte = Serial.read(); //reads the incoming byte

   switch (inByte) // depending on character received choose
      ↪ between several discrete options
   {
     case 'a' : // decrease pressure
      servo.write(88);
      delay(100);
      servo.write(90);


      break;
     case 'b' : // increase pressure
       servo.write(92);
       delay(100);
       servo.write(90);

       break;
```

```
      default: // if nothing else matches, do the default (ie
         ↪ stationary)
        servo.write(90);
    }

    delay(15);
    Serial.write(inByte);
  }
}
```

Appendix B

RRKM Code

This section includes the code used for the RRKM calculations completed as part of Chapter 4. A very similar version was used for Chapter 3. The code has 5 main components. First the vibrational frequencies of all the stationary points are read from individual files that contain a single frequency on each line. The next bunch of code is the implementation of the Beyer-Swinehart algorithm into functions for densities and sums of states with and without internal rotation. The next section uses the Beyer-Swinehart algorithm functions to calculate the densities and sums of state for the stationary points. Each function call reads in the frequencies, and energy of each state as well as the symmetry and B value if there is an internal rotation. The B value is calculated using the code in Section B.2.1. The next section of the code uses the densities and sums of state to calculate the individual rate constants using the micro-canonical RRKM equation. The final section of the code uses the rate constants to calculate the branching ratios. The branching ratio equations were determined from solving the kinetic scheme using the steady state approximation.

B.1 Python Code

```
import math
import numpy as np

MaxEnergy = 40323+1 # 248nm in cm^-1 = 40323, 193nm in cm^-1 =
    ↪ 51814

#This section imports the frequencies for the stationary points
ww2a=np.loadtxt('Frequencies/w2a.txt')

ww4=np.loadtxt('Frequencies/w4.txt')
ww5=np.loadtxt('Frequencies/w5.txt')
ww6=np.loadtxt('Frequencies/w6.txt')
```

```
ww7=np.loadtxt('Frequencies/w7.txt')
ww16=np.loadtxt('Frequencies/w16.txt')


wts2a=np.loadtxt('Frequencies/ts2a.txt')
wts6a=np.loadtxt('Frequencies/ts6a.txt')
wts7a=np.loadtxt('Frequencies/ts7a.txt')

wts8=np.loadtxt('Frequencies/ts8.txt')
wts10=np.loadtxt('Frequencies/ts10.txt')
wts22=np.loadtxt('Frequencies/ts22.txt')

wtsc=np.loadtxt('Frequencies/tsc.txt')
wtsi=np.loadtxt('Frequencies/tsi.txt')
wtsp=np.loadtxt('Frequencies/tsp.txt')
wtsq=np.loadtxt('Frequencies/tsq.txt')

#This section has the subroutine functions for the Beyer Swinehart
   ↪ Algorithm
def BSrhovib(w,Energy):
        Eavail=MaxEnergy-Energy
        rho=np.zeros((Eavail,1),dtype=(float))
        rho[0]=1
        j=0
        i=0
        w=np.around(w)
        w=w.astype(int)
        NOscillators = w.size
        print NOscillators
        while i<NOscillators:
                j = w[i]
                while j<Eavail:
                        rho[j]=rho[j]+rho[j-w[i]]
                        j+=1
                i+=1
        return rho[Eavail-1]

def BSsumvib(w,Energy):
        Eavail=MaxEnergy-Energy
        sum=np.ones((Eavail,1),dtype=(float))
        j=0
        i=0
```

```
        w=np.around(w)
        w=w.astype(int)
        NOscillators = w.size
        print NOscillators
        while i<NOscillators:
                j = w[i]
                while j<Eavail:
                        sum[j]=sum[j]+sum[j-w[i]]
                        j+=1
                i+=1
        return sum[Eavail-1]

def BSrhovibrot(w,Energy,sigma,B):
        Eavail=MaxEnergy-Energy
        rho=np.zeros((Eavail,1),dtype=(float))
        i=1
        while i<Eavail:
                rho[i] = math.sqrt(1/(B*i))/sigma
                i+=1
        rho[0]=1
        j=0
        i=0
        w=np.around(w)
        w=w.astype(int)
        NOscillators = w.size
        print NOscillators
        while i<NOscillators:
                j = w[i]
                while j<Eavail:
                        rho[j]=rho[j]+rho[j-w[i]]
                        j+=1
                i+=1
        return rho[Eavail-1]

def BSsumvibrot(w,Energy,sigma,B):
        Eavail=MaxEnergy-Energy
        #print Eavail
        sum=np.zeros((Eavail,1),dtype=(float))
        i=1
        while i<Eavail:
                sum[i] = 2*math.sqrt(i/B)/sigma
                i+=1
```

```
        sum[0]=1
        #print sum[0],sum[100],sum[2000]
        j=0
        i=0
        w=np.around(w)
        w=w.astype(int)
        #print w
        NOscillators = w.size
        print NOscillators
        while i<NOscillators:
                j = w[i]
                while j<Eavail:
                        sum[j]=sum[j]+sum[j-w[i]]
                        j+=1
                i+=1
        return sum[Eavail-1]

#This section calculates the densities and sums of states for each
   ↪ stationary point
rho4=int(BSrhovibrot(ww4,21650,1,1.0225))
rho5=int(BSrhovib(ww5,10423))
rho6=int(BSrhovibrot(ww6,19062,3,6.349))
rho7=int(BSrhovibrot(ww7,16474,3,5.46))
rho16=int(BSrhovibrot(ww16,20636,1,1.2933))


rho2a=int(BSrhovib(ww2a,11500))


sum8=int(BSsumvib(wts8,36795))

sum10=int(BSsumvibrot(wts10,34591,3,5.45))

sum22=int(BSsumvib(wts22,31618))


sumc=int(BSsumvib(wtsc,35291))
sumi=int(BSsumvib(wtsi,33996))

sump=int(BSsumvibrot(wtsp,29974,3,4.95))
sumq=int(BSsumvibrot(wtsq,31198,1,0.98095))
```

```
sum2a=int(BSsumvib(wts2a,26518))
sum6a=int(BSsumvib(wts6a,26718))
sum7a=int(BSsumvibrot(wts7a,31856,1,1.09697))



#This section calculates the rates of individual reactions with
    ↪ the microcanonical RRKM equation
h=3.3356392219199*10**(-11)


k420=3*sumc/(h*rho4)
k56=1*sum8/(h*rho5)
k65=2*sum8/(h*rho6)
k67=1*sum10/(h*rho6)
k76=1*sum10/(h*rho7)
k722=1*sump/(h*rho7)
k1618=1*sumi/(h*rho16)
k1623=1*sumq/(h*rho16)
k516=1*sum22/(h*rho5)
k165=2*sum22/(h*rho16)
k2a16=1*sum2a/(h*rho2a)
k2a4=1*sum6a/(h*rho2a)
k162a=1*sum2a/(h*rho16)
k42a=1*sum6a/(h*rho4)
k423=1*sum7a/(h*rho4)

#This section prints out the reaction rates
print "k420",k420
print "k1618",k1618
print "k1623",k1623
print "k516",k516
print "k165",k165
print "k423", k423
print "k2a4", k2a4
print "k2a16", k2a16

#This section calculates the branching ratios. The equations are
    ↪ determined by solving the kinetic schemes.
```

```
BRA=(k1623 *(k2a4 *k423 + k2a16* (k420 + k423))* (k56 *k67 *k722 +
   ↪     k516 *(k67 *k722 + k65* (k722 + k76))) +  k2a4 *k423 *(
   ↪ k165 *k56* k67* k722 + k1618 *(k56* k67 *k722 + k516 *(k67*
   ↪ k722 + k65 *(k722 + k76)))))/(k1618 *(k2a4 *k420 +    k2a16*
   ↪  (k420 + k423))* (k56* k67* k722 + k516 *(k67 *k722 + k65* (
   ↪ k722 + k76))) + k2a4 *k420 *(k165* k56 *k67 *k722 + k1623 *(
   ↪ k56* k67 *k722 + k516 *(k67* k722 + k65* (k722 + k76)))))
print "BR acetylene over total H loss", BRA

BRE=(k1618* k2a16* (k420 + k423) *(k56 *k67 *k722 + k516 *(k67 *
   ↪ k722 + k65 *(k722 + k76))))/(k2a4 *k420 *(k165 *k56* k67 *
   ↪ k722 + k1618* (k56 *k67 *k722 + k516* (k67 *k722 + k65 *(
   ↪ k722 + k76))) + k1623 *(k56 *k67 *k722 + k516 *(k67 *k722 +
   ↪ k65* (k722 + k76)))))
print "BR ethynylallene over pentadiyne", BRE

BRM = (k165 *k2a16* (k420 + k423)* k56* k67* k722)/(k1623 *(k2a4 *
   ↪ k423 + k2a16* (k420 + k423))* (k56 *k67 *k722 + k516* (k67 *
   ↪ k722 + k65 *(k722 + k76))) + k2a4 *k423 *(k165 *k56 *k67 *
   ↪ k722 + k1618 *(k56 *k67* k722 + k516 *(k67 *k722 + k65 *(
   ↪ k722 + k76))))
print "BR methyl over acetylene", BRM

BREA = (k1618* k2a16 *(k420 + k423)* (k56* k67 *k722 + k516* (k67
   ↪ *k722 + k65 *(k722 + k76))))/(k1623 *(k2a4* k423 + k2a16 *(
   ↪ k420 + k423))* (k56* k67* k722 + k516* (k67* k722 + k65 *(
   ↪ k722 + k76))) + k2a4 *k423 *(k165* k56 *k67* k722 + k1618* (
   ↪ k56 *k67 *k722 + k516* (k67 *k722 + k65* (k722 + k76)))))
print "BR ethynyallene over acetylene", BREA
```

B.2 Rotational Constant Code

For stationary points with internal rotors, the rotational constant was calculated with the Mathematic code below. The code requires the user to input all of the parameters and change the code slightly for each molecule. The code takes the x,y,z coordinates of the two atoms that constitute the rotational axis and computes the distance of every other atom from the rotational axis. Then the moment of inertia is calculated for both sections of the molecule that are rotating relative to each other. The reduced moment of inertia is calculated and used to determine the rotational constant, B.

B.2.1 Mathematica Code

```
Clear["Global`*"]

d = Norm[Cross[(X0 - X1), (X0 - X2)]] / Norm[(X2 - X1)]
```

$$\frac{\text{Norm}[(X0 - X1) \times (X0 - X2)]}{\text{Norm}[-X1 + X2]}$$

```
X1 = {1.46181400, 1.01727600, 0.00000000};
X2 = {-0.60793300, 0.56591500 , 0.00000000};

X0 = {1.78356800, 2.21708500, 0.00000000};
dc4 = d
1.1037

X0 = {1.73068100 , 3.28460800 , 0.00000000};
dh12 = d
2.15798

X0 = {1.79426100, -0.00448700, 0.00000000};
dh14 = d
1.06913

I1 = dh14^2 + dh12^2 + 12 * dc4^2
20.4179
```

```
X0 = {-0.65625300, -1.59669600, 0.73368300};
dc1 = d
X0 = {-0.65625300, -0.30189700, 1.17457300};
dc2 = d
X0 = {-0.65625300, -1.59669600, -0.73368300};
dc5 = d
X0 = {-0.65625300, -0.30189700, -1.17457300};
dc6 = d
X0 = {-0.66304100, -2.48646700, 1.35266600};
dh7 = d
X0 = {-0.66304100, -2.48646700, -1.35266600};
dh8 = d
X0 = {-0.65677100 , 0.04217100, -2.20056200};
dh9 = d
X0 = {-0.95993700 , 1.58993200, 0.00000000};
dh11 = d
X0 = {-0.65677100 , 0.04217100 , 2.20056200};
dh13 = d


2.22698

1.44263

2.22698

1.44263

3.26403

3.26403

2.25694

1.0755

2.25694

I2 = 12 * (dc2^2 + dc1^2 + dc5^2 + dc6^2) + dh7^2 + dh8^2 + dh9^2 + dh11^2  + dh13^2

201.627

Inet = I1 * I2 / (I1 + I2)

18.5404

16.8576 / Inet

0.909238

B12 = 16.8448 / Inet

0.908548
```

Appendix C

Publications Resulting From Graduate Work

1. Shapero, M.; Ramphal, I.A.; Neumark, D.M. Photodissociation of the Cyclopentadienyl Radical at 248 nm. *J. Phys. Chem. A*, Submitted.

2. Ramphal, I.A.; Shapero, M.; Haibach-Morris, C.; Neumark, D.M. Photodissociation Dynamics of Fulvenallene and the Fulvenallenyl Radical at 248 and 193 nm. *Phys. Chem. Chem. Phys.*, **2017**, 19, 29305.

3. Cole-Filipiak, N.C.; Shapero, M.; Haibach-Morris, C.; Neumark, D.M. Production and Photodissociation of the Methyl Perthiyl Radical. *J. Phys. Chem. A*, **2016**, 120, 4818.

4. Shapero, M; Cole-Filipiak, N.C.; Haibach-Morris, C.; Neumark, D.M. Benzyl Radical Photodissociation Dynamics at 248 nm. *J. Phys. Chem. A*, **2015**, 119, 12349.

5. Cole-Filipiak, N.C.; Shapero, M.; Negru, B.; Neumark, D.M. Revisiting the Photodissociation Dynamics of the Phenyl Radical. *J. Chem. Phys.*, **2014**, 141, 1004307.